| | | | |
|---|---|---|---|
| **1.0** | 4.5 | 2.8 | 2.5 |
| | 50 | 3.2 | 2.2 |
| | 56 | 3.6 | |
| **1.1** | 63 | 4.0 | 2.0 |
| | | | 1.8 |
| **1.25** | | **1.4** | **1.6** |

MICROCOPY RESOLUTION TEST CHART
NATIONAL BUREAU OF STANDARDS-1963-A
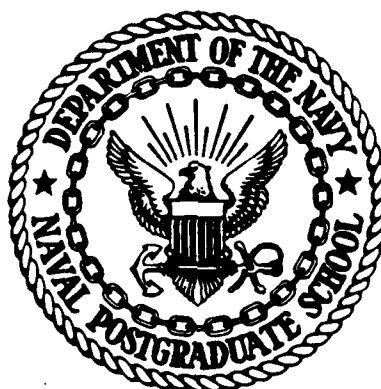
# NAVAL POSTGRADUATE SCHOOL
## Monterey, California

DTIC
ELECTE
JUL 1 1985
S
D
B

# THESIS

A NUMERICAL AND ANALYTICAL INVESTIGATION OF
LEE CYCLOGENESIS

by

John L. Hayes

March 1985

Thesis Advisor:                Dr. R. T. Williams

Approved for public release, distribution unlimited

| REPORT DOCUMENTATION PAGE | | READ INSTRUCTIONS<br>BEFORE COMPLETING FORM |
|---|---|---|
| **1. REPORT NUMBER** | **2. GOVT ACCESSION NO.** | **3. RECIPIENT'S CATALOG NUMBER** |
| **4. TITLE** *(and Subtitle)*<br><br>A Numerical and Analytical Investigation<br>of Lee Cyclogenesis | | **5. TYPE OF REPORT & PERIOD COVERED**<br>Doctor of Philosophy<br>March, 1985 |
| | | **6. PERFORMING ORG. REPORT NUMBER** |
| **7. AUTHOR(s)**<br><br>John L. Hayes | | **8. CONTRACT OR GRANT NUMBER(s)** |
| **9. PERFORMING ORGANIZATION NAME AND ADDRESS**<br><br>Naval Postgraduate School<br>Monterey, California 93943 | | **10. PROGRAM ELEMENT, PROJECT, TASK**<br>**AREA & WORK UNIT NUMBERS** |
| **11. CONTROLLING OFFICE NAME AND ADDRESS**<br><br>Naval Postgraduate School<br>Monterey, California 93943 | | **12. REPORT DATE**<br>March, 1985 |
| | | **13. NUMBER OF PAGES**<br>138 |
| **14. MONITORING AGENCY NAME & ADDRESS***(if different from Controlling Office)* | | **15. SECURITY CLASS.** *(of this report)*<br><br>UNCLASSIFIED |
| | | **15a. DECLASSIFICATION/DOWNGRADING**<br>**SCHEDULE** |
| **16. DISTRIBUTION STATEMENT** *(of this Report)*<br><br>Approved for public release, distribution unlimited. | | |
| **17. DISTRIBUTION STATEMENT** *(of the abstract entered in Block 20, if different from Report)* | | |
| **18. SUPPLEMENTARY NOTES** | | |
| **19. KEY WORDS** *(Continue on reverse side if necessary and identify by block number)*<br><br>Numerical Weather Prediction<br>Topographic Effects<br>Cyclogenesis<br>Baroclinic Instability | | |

**20. ABSTRACT** *(Continue on reverse side if necessary and identify by block number)*

The effect of topography on the evolution of a disturbance in a baroclinically unstable mean flow is studied using analytical and numerical simulations. In particular, dynamical mechanisms involved in cyclogenesis in the lee of long, meridional barriers similar to the Rocky Mountains are explored. The rapid growth observed in lee cyclogenesis is highly dependent on the superposition of a growing baroclinic wave with a steady, orographically forced wave of the same scale. As the baroclinic wave

1

20. Abstract (Continued)

moves over the mountain, development is masked by the orographically-forced, high-pressure ridge.  As it moves down the lee side of the mountain, the baroclinic wave appears to grow rapidly due to superposition with the forced, lee-side trough.  Indications of enhanced, lee-side baroclinic instability are present in the numerical simulations, but the effect on wave development is minor compared to the effect of super-position.  The rapid continuous-mode growth which has recently been demonstrated by Farrell (1982) is not observed in any of the simulations.

Accession For

| | |
|---|---|
| NTIS GRA&I | ✓ |
| DTIC TAB | ☐ |
| Unannounced | ☐ |
| Justification | |

By
Distribution/
Availability Codes

| Dist | Avail and/or Special |
|---|---|
| A-1 | |

DTIC
COPY
INSPECTED
1

A Numerical and Analytical Investigation of Lee Cyclogenesis

by

John L. Hayes
Major, United States Air Force
B.S., Bowling Green University, 1970
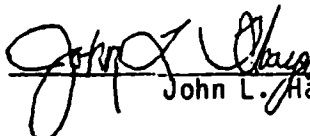M.S., Naval Postgraduate School, 1977

Submitted in partial fulfillment of the
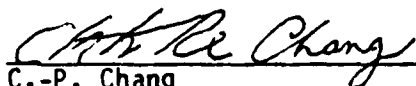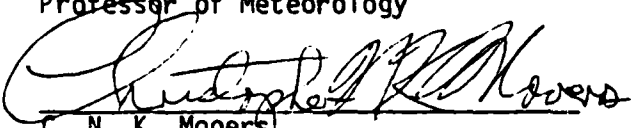requirements for the degree of

DOCTOR OF PHILOSOPHY

from the

NAVAL POSTGRADUATE SCHOOL
March 1985

Author: _____
John L. Hayes
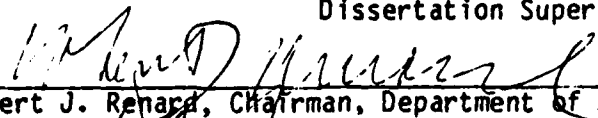
Approved by:

_____          _____
C.-P. Chang                               R. L. Elsberry
Professor of Meteorology                  Professor of Meteorology
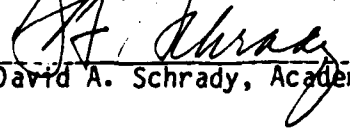
_____          _____
C. N. K. Mooers                           A. L. Schoenstadt
Professor & Chairman of Oceanography      Associate Professor of Mathematics

_____          _____
C. H. Wash                                R. T. Williams
Associate Professor of Meteorology        Professor of Meteorology
                                          Dissertation Supervisor
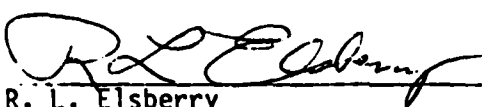
Approved by: _____
Robert J. Renard, Chairman, Department of Meteorology

Approved by: _____
David A. Schrady, Academic Dean

3

## ABSTRACT

The effect of topography on the evolution of a disturbance in a baro-
clinically unstable mean flow is studied using analytical and numerical
simulations. In particular, dynamical mechanisms involved in cyclogene-
sis in the lee of long, meridional barriers similar to the Rocky Moun-
tains are explored. The rapid growth observed in lee cyclogenesis is
highly dependent on the superposition of a growing baroclinic wave with a
steady, orographically forced wave of the same scale. As the baroclinic
wave moves over the mountain, development is masked by the orographical-
ly-forced, high-pressure ridge. As it moves down the lee side of the
mountain, the baroclinic wave appears to grow rapidly due to superposi-
tion with the forced, lee-side trough. Indications of enhanced, lee-side
baroclinic instability are present in the numerical simulations, but the
effect on wave development is minor compared to the effect of superposi-
tion. The rapid continuous-mode growth which has recently been demon-
strated by Farrell (1982) is not observed in any of the simulations.

4

## TABLE OF CONTENTS

# LIST OF FIGURES

7

8

10

## ACKNOWLEDGEMENTS

carried out at the W. R. Church Computer Center and the dissertation was carefully typed by Ms. Nita Raichart.

Finally, I want to say thank you to my wife, Sharon, for her patience, understanding and support throughout this period. She sacrificed and endured through the hard times - always encouraging me to continue on. She is the light of my life, and I dedicate this dissertation to her.

# I. INTRODUCTION

In recent years, there has been renewed interest in the effects of topography on atmospheric flows. Mountains of various shapes, sizes and orientations force motions on all scales - from small, turbulent eddies to planetary waves. The objective of this research is to determine the crucial mechanisms in lee cyclogenesis, wherein cyclones form on the downwind side of major mountain ranges.

It has been generally accepted for a number of years that a dynamical connection exists between the presence of mountains and the occurrence of lee cyclogenesis. This is based on evidence presented in both observational and numerical studies. Petterssen's (1956) climatological statistics of cyclogenesis frequency established that the lee sides of large mountain complexes such as the Rockies, the Alps and the Himalayas are preferred regions for cyclogenesis. More recently, the observational studies by Reitan (1974); Chung, Hage and Reinelt (1976); Zishka and Smith (1980); as well as others, have produced similar findings. In addition, various numerical studies, such as those by Egger (1974); Manabe and Terpstra (1974); Bleck (1977); and Tibaldi, Buzzi and Malguzzi (1980), have concluded that inclusion of topography in numerical models is necessary to predict cyclogenesis in the "preferred" regions. Consequently, it is generally accepted that mountains play a role in the cyclogenesis process. However, the dynamical nature of that role is still not well understood.

The basic components of lee cyclogenesis appear to include: large mountains, the presence of the jet stream normal to the mountain barrier, and a pre-existing disturbance. The required mountain size is somewhat arbitrarily defined, although the results of Petterssen (1956) and others indicate that cyclogenesis is not observed with enhanced frequency in the lee of mountains with smaller heights and widths, such as the Urals. The presence of the jet stream during lee cyclogenesis has been thoroughly documented in a number of studies, including Newton (1956), Klein (1957), Hovanec and Horn (1975), and Whittaker and Horn (1980) for the Rockies, and Trevisan (1976) and Buzzi and Tibaldi (1980) for the Alps. In the typical case (see, for example, Hess and Wagner, 1945; Palmen and Newton, 1969; and Buzzi and Tibaldi, 1980), lee cyclogenesis is initiated as a disturbance crosses a large mountain range. During the initial stages of development, rapid intensification is observed with e-folding times of 12 hours or less (Buzzi and Tibaldi, 1980). This e-folding time is much less than the rough estimate of 25-30 hours given for cyclogenesis occurring away from mountains (Palmen and Newton, 1969; Holton, 1971). After moving away from the mountain, the growth and phase speed of the lee cyclone approach those values normally associated with cyclone development. Consequently, it has been suggested that topography alters the baroclinic instability process in a way that results in more rapid intensification on the lee side of large mountain ranges.

The basic objective of this research is to gain a better understanding of how topography affects the cyclogenesis process. This investigation will provide insight into the dynamical basis for the rapid intensification which is observed on the lee side of large mountain

ranges, and, in so doing, provide a better understanding of why these areas are preferred regions for cyclogenesis. Since the nature of the orographic effect is dependent on the size, scale and orientation of the mountains (Palmen and Newton, 1969; Chung et al., 1976; and others) the types of mountain ranges to be considered must be limited. This research focuses on cyclogenesis in the lee of a long, meridional barrier which is intended to simulate the Rocky Mountains. Cyclogenesis is treated as a manifestation of baroclinic instability, and orographic effects are sought which can explain the increased growth which is observed on the lee side of large mountains.

Recent dynamical investigations of flow over topography provide a number of possible mechanisms which could play a role in the cyclogenesis process. Charney and DeVore (1978), and Charney and Strauss (1979) considered topographic forcing of atmospheric flow and identified the form-drag instability which results from the interaction of mean flows with large-scale mountains. This mechanism, which depends on the Rossby wave being nearly stationary, appears to play a role in the evolution of planetary waves and blocking patterns; these waves occur on scales larger than those observed in lee cyclogenesis. Pedlosky (1981) considered resonant topographic forcing as a growth mechanism and found that slowly moving long waves could experience large increases in amplitude due to resonance. This mechanism also appears to be applicable to the longer and more slowly moving planetary waves rather than the cyclone waves, and it is not investigated here.

Merkine (1975, 1977) and Merkine and Israeli (1978) have considered the interaction of baroclinic flows with topography using the

15

quasi-geostrophic and semi-geostrophic equations. Merkine's (1975) solution for a vertically sheared, steady, quasi-geostrophic flow past an infinitely long ridge showed that the flow acquires a vertically sheared northerly component of velocity along the lee side of the mountain. This vertically sheared northerly component is in addition to the shear of the basic state and indicates enhanced baroclinicity. According to Merkine, the increased baroclinicity could explain the higher growth rates observed in lee cyclogenesis. However, it has not been demonstrated how such enhancement could increase the instability of lee cyclones.

Farrell (1982) used the linearized quasi-geostrophic equations to demonstrate that continuous-mode solutions can, with the proper initial conditions, exhibit large growth rates for periods of up to 12 hours after excitation; this initial growth is followed by damping. The addition of these modes to the exponentially growing discrete modes could explain the enhanced growth which is observed in lee cyclogenesis. The selection of initial conditions is crucial for this effect, since one could always pick a special initial state with will give rapid initial growth.

Smith (1984) has proposed a baroclinic lee wave mechanism for lee cyclogenesis in the Alps. This mechanism depends on a mean flow in which the vertical wind shear is opposite to the surface component across the mountain range. However, it does not appear to apply to the Rocky Mountain cases where the vertical shear is usually in the same general direction as the surface wind.

Still another possibility is that the mountains have only an apparent effect on the cyclogenesis process. A steady flow over a synoptic-scale

mountain forces a stationary high-pressure ridge over the mountain and a pressure trough on the leeward side (see, for example, Smith, 1979). A growing cyclonic disturbance of approximately the same scale as the mountain would be cancelled by superposition with the high pressure ridge as it moves over the topography. On the lee side, large growth rates would be observed as the cyclonic disturbance continues to grow and become superposed with the lee-side trough. With a high enough mountain, such lee-side growth could appear as rapid deepening. In addition, the lee-side superposition would induce a closed circulation at an earlier stage of the amplification process than would occur over the mountain or flat terrain. As a result, the initial appearance of the closed surface-pressure contour (which is defined as cyclogenesis in most of the studies quoted above) would be accelerated by the presence of the mountain. This could explain the higher frequencies of lee cyclogenesis, since growing waves placed randomly are more likely to have the first closed contour over the lee than over the mountain top.

Of the dynamical mechanisms described above for lee cyclogenesis, the three most likely are examined in this study: 1) enhanced, lee-side baroclinic instability; 2) continuous-mode growth; and 3) superposition. Chapter II treats analytically the interaction between an infinitely long mountain range and baroclinic waves in the basic state which was used by Eady (1949). The quasi-geostrophic equations for this problem are linear so that the mountain-forced solution and the unstable Eady solution are mathematically independent. An example is given which shows that the superposition of the two simple solutions can give a reasonable representation of lee cyclogenesis. Semi-geostrophic solutions are also

17

derived which show some interaction between the mountain and the moving disturbances. This interaction changes the phase speed of the moving wave, but it does not change the intensity of the disturbance.

In Chapter III, the finite-difference and spectral numerical models which will be used in later chapters are described. The topography and initial conditions for the following numerical experiments are found in Chapter IV. In Chapter V, the continuous-mode growth mechanism which was proposed by Farrell (1982) is investigated. The initial conditions are crucial to this mechanism. In this study, simple orographic forcing is used to perturb a basic state that initially contains no perturbations. Such a situation might be expected if the mean flow was rapidly increased from zero to the limiting value. The linear study in this chapter uses the spectral model and the nonlinear study uses the finite-difference model. None of these experiments show any significant continuous-spectrum growth.

Chapter VI contains the numerical experiments with more realistic conditions which include a pre-existing disturbance and a baroclinic jet with vertical and horizontal shear. A procedure is developed which allows a comparison between a transient mountain solution and a solution in which a no-mountain transient solution is superposed on a forced mountain solution. The experiments are carried out for a range of initial disturbance amplitudes so that the small-amplitude experiments show the linear behavior of a wave in a mean flow forced by the mountain. The larger amplitude experiments include nonlinear interaction between the disturbance and the mountain-forced flow. The experiments show no significant difference in intensity between the mountain interaction

18

cases and the superposition cases. Phase changes are found in the inter-action cases which are consistent with those predicted by the semi-geostrophic theory in Chapter II. The various studies included in this research lead to the conclusion that superposition is the main mechanism for lee cyclogenesis with mountain systems similar to the Rocky Mountains.

# II. <u>ANALYTICAL MODELS</u>

Baroclinic instability has been accepted as a major source of propagating synoptic-scale disturbances in the mid-latitudes. The success of this theory in predicting the general scale, growth, and structure of cyclone waves is undisputed. In this chapter, some simple analytical models are introduced to provide a theoretical basis for investigating the dynamical mechanisms involved in lee cyclogenesis.

In the first section, the model developed by Eady (1949) is briefly reviewed. Although this model does not include topography, it provides a good description of wave development in the early stages of cyclogenesis and is useful for examining the linear dynamics of baroclinic instability. In the second section, Eady's model is modified to include small-amplitude topography through the lower boundary condition; the forced, steady solution is derived for investigating orographic effects on wave development. In the third section, a non-geostrophic model is used to describe wave development in the presence of a finite-amplitude mountain. The potential vorticity equation for this model is transformed following Hoskins and Bretherton (1972) and solved analytically. Analysis of the solution reveals that finite-amplitude topography distorts the structure of a developing baroclinic wave while in the vicinity of the mountain, but has no net effect on growth away from the mountain. As will be demonstrated, these simple models appear to explain very well some of the dynamical features observed in lee cyclogenesis.

20

## A. REVIEW OF THE EADY MODEL

Eady (1949) considered a simple, yet realistic baroclinic instability problem. His model uses the linearized form of the quasi-geostrophic equations with the Boussinesq approximation to describe an inviscid atmosphere confined between two rigid horizontal plates. The basic problem is stated in terms of a single partial differential equation which expresses conservation of potential vorticity. The vertical velocity is assumed to vanish at the boundaries, $z = 0, 1$ (where $z = - \ln p/p_0$ is the non-dimensional vertical coordinate). The following assumptions are made: The basic wind flow varies linearly with height - that is, $U = Sz$, where $S$ is a constant. The supporting horizontal temperature gradient is constant. The basic state density, $\bar{\rho}$, and the static stability, $\Gamma$, are taken as constants, and the effect of the earth's sphericity is ignored by assuming that the Coriolis parameter is constant. With these assumptions and the normal mode solution form

$$\psi = \text{Re}\left[\psi_F(z)e^{i\mu(x - ct)}\right] \qquad , \qquad (2.1)$$

the quasi-geostrophic potential vorticity equation reduces to the ordinary differential equation for $\Psi_F(z)$ given by Haltiner and Williams (1980):

$$(U - c)\left[(f_0^2/\Gamma)\frac{d^2\Psi}{dZ^2}F - \mu^2 \varepsilon \Psi_F\right] = 0 \qquad . \qquad (2.2)$$

21

The subscript, F, is used here to denote the free, or unforced, solution. The boundary conditions are obtained from the first law of thermodynamics

$$\left(\frac{\partial}{\partial t} + U \frac{\partial}{\partial x}\right) \frac{\partial \psi}{\partial z} - \frac{\partial \psi}{\partial x} \frac{\partial U}{\partial z} + \frac{1}{f_0} \Gamma \dot{z} = 0 \qquad \qquad (2.3a)$$

If (2.1) is substituted into (2.3a) and the non-dimensional vertical velocity

$$\dot{z} = \text{Re} \left[ W(z) e^{i\mu(x-ct)} \right] \qquad , \text{ then (2.3a) becomes}$$

$$(U - c) \frac{\partial \Psi_F}{\partial z} - \frac{\partial U}{\partial z} \Psi_F + \frac{\Gamma W}{i\mu f_0} = 0 \qquad \qquad (2.3b)$$

At the upper and lower boundaries where $\dot{z} = 0$, the boundary conditions become

$$(U - c) \frac{\partial \Psi_F}{\partial z} - S\Psi_F = 0, \quad z = 0,1 \qquad \qquad (2.4)$$

The free solution takes the form

$$\Psi_F = A \sinh \left(\frac{Z}{\epsilon^{\frac{1}{2}}}\right) + B \cosh \left(\frac{Z}{\epsilon^{\frac{1}{2}}}\right) \qquad , \qquad (2.5)$$

where $\qquad \epsilon = \dfrac{f_0^2}{\Gamma \mu^2}$

22

Application of the boundary conditions yields the characteristic equation for the phase speed, c. The condition for baroclinic instability is that c must be complex, which occurs if

$$L > \frac{\Gamma^{\frac{1}{2}}}{2.4 f_0} \qquad \text{and} \qquad S \neq 0 \qquad , \qquad (2.6)$$

where $L = 2\pi/\mu$. When these conditions are satisfied, $\psi$ in (2.1) becomes an exponential function of time, with growth rate proportional to vertical shear. Maximum growth rate is predicted for

$$L = \frac{\Gamma^{\frac{1}{2}}}{1.92 f_0} \qquad ;$$

this indicates that wavelengths of the order of 4,000 km will dominate the spectrum of atmospheric waves, and is in approximate agreement with the observed scale of mid-latitude cyclones.

## B. EADY'S MODEL WITH SIMPLE TOPOGRAPHY

The effect of topography can easily be included in Eady's model if the topography has a small amplitude compared to the scale height of the atmosphere. In this case, the basic flow remains zonal and the effect of the topography is felt through the lower boundary only. This simplification is frequently made for mathematical convenience and provides a rough approximation of the effect of the topography on the flow. As will be shown, even with this weakness, the model is able to describe at least qualitatively the increased growth observed on the lee side of the mountain.

23

## 1.  Model Formulation

Consider the case of steady flow over a small-amplitude mountain
with a profile given by

$$h(x) = \left( \text{Re } h_s e^{i\mu x} \right) \quad , \quad (2.7)$$

where $h_s$ is a constant.  Notice that $h$ is independent of $y$, which indi-
cates a mountain of infinite north-south extent.  Let the basic flow be
given by

$$U = U_s + Sz \quad , \quad (2.8)$$

where $U_s$, the surface wind, is constant.  It will be shown below that the
inclusion of the surface current is necessary to obtain an orographic
effect through the lower boundary.  The surface current has no effect on
the preferred scale and growth rate of the basic Eady solution reviewed
above.  If the solution form

$$\psi = \text{Re } \left( \Psi_M e^{i\mu(x - ct)} \right) \quad , \quad (2.9)$$

is substituted into the steady form of the quasi-geostrophic potential
vorticity equation, the equation becomes

$$\left( \frac{f^2{}_0}{\Gamma} \frac{d^2 \Psi_M}{dz^2} - \mu^2 \Psi_M \right) = 0 \quad , \quad (2.10)$$

24

where the subscript, M, indicates the steady, mountain-forced solution.
The boundary conditions are obtained from (2.3b). At the upper boundary,
where $\dot{z} = 0$,

$$(U_S + S) \frac{d\psi_M}{dz} - S\psi_M = 0 \qquad , \qquad (2.11a)$$

while at the lower boundary,

$$U_S \frac{d\Psi_M}{dz} - S\Psi_M + \frac{\Gamma}{f_0} U_S \frac{h_S}{H} = 0 \qquad , \qquad (2.11b)$$

where H is the scale height of the atmosphere. The term in (2.11b) which
includes $h_S$ follows from the topographically-forced vertical velocity at
the lower boundary

$$\dot{z}(x,0) = \frac{U_S}{H} \frac{\partial h}{\partial x} \qquad . \qquad (2.12)$$

The solution of (2.10) with boundary conditions (2.11a, b) is

$$\Psi_M = - \frac{\Gamma U_S h_S \epsilon^{\frac{1}{2}}}{f_0 H(U_S \alpha - S_\epsilon^{\frac{1}{2}} \gamma)} \quad \alpha \sinh \left(\frac{z}{\epsilon^{\frac{1}{2}}}\right) + \gamma \cosh \left(\frac{z}{\epsilon^{\frac{1}{2}}}\right) \qquad , \qquad (2.13)$$

where

$$\epsilon = \frac{f_0^2}{\Gamma \mu^2} \qquad\qquad \alpha = (1 - r \tanh \epsilon^{-\frac{1}{2}})$$

$$r = \epsilon^{-\frac{1}{2}}(\frac{U_S}{S} + 1) \qquad\qquad \gamma = r - \tanh \epsilon^{-\frac{1}{2}} \qquad .$$

25

This result shows that the amplitude of the forced wave is proportional to the magnitude of the surface wind and the height of the mountain. As indicated previously, a non-zero surface wind is required for an orographic effect on the flow. The solution $\psi = \Psi_M e^{i\mu x}$ is shown for various levels in Figure 2.1. A high-pressure ridge is centered over the mountain with troughs on both the upstream and downstream sides. The phase is constant with height, but the amplitude damps exponentially. The amplitude of the meridional wind component, $v = \partial\psi/\partial x$ is shown versus height for various wave numbers in Figure 2.2. The amplitude of $v$ damps in the vertical in each case, and the magnitude of the damping increases with wave number. This latter result indicates that, as the horizontal scale of the mountain is decreased, the vertical extent of the orographic effect is reduced. These solutions are generally similar to those given by Smith (1979) for an atmosphere with no vertical wind shear.

## 2. Model Application

The steady, forced solution given by (2.9) may be combined with the free Eady solution to form a linear model of a wave passing over topography. As a result of the linearity assumption, the free and forced solutions do not interact. Therefore, this model does not predict any new or enhanced instability mechanism associated with the mountain. However, due to superposition, a developing, small-amplitude, baroclinic wave of the proper scale can be cancelled by the forced ridge as it moves over the crest of the mountain and appear to grow rapidly as it moves down the lee slope and into phase with the stationary trough.

26
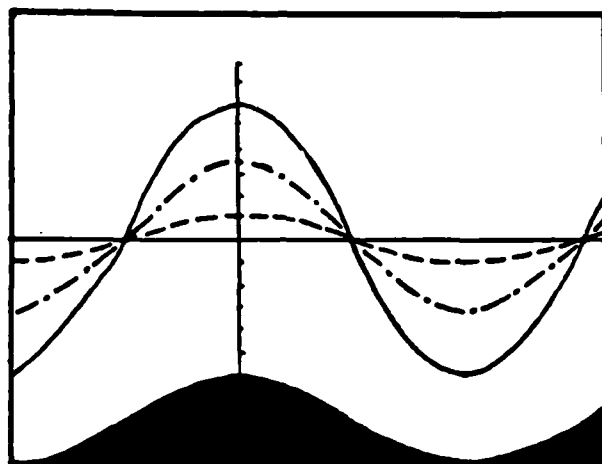
Figure 2.1. Steady, forced solution $\psi = \Psi_M(z) \cos \mu x$ given by (2.13). Solution is given at: $z = 0.0$ (solid curve), $z = 0.5$ (dotted-dashed curve), and $z = 0.1$ (dashed curve); $z = -\ln p/p_s$ is the non-dimensional vertical coordinate. The shaded region at the bottom represents the terrain, $h = h_s \cos \mu x$.
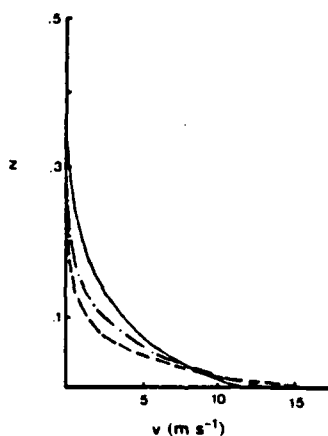


Figure 2.2. Amplitude of the steady forced solution $v = \partial \psi / \partial x$ as a function of non-dimensional height, z, for global wave numbers: $\mu_* = 8$ (solid), $\mu_* = 12$ (dotted-dashed), and $\mu_* = 16$ (dashed).

27

Let the constants in equations (2.1 - 2.13) be given the follow-ing mid-latitude values: $f_0 = 10^{-4}$ $s^{-1}$, $\Gamma = 10^4 m^2 s^{-2}$, $U_s = 5$ m $s^{-1}$, and $S = 40$ m $s^{-1}$. The constant B in (2.5) represents the initial amplitude of the free wave and is arbitrarily assigned the value of 300 $m^2 s^{-1}$. Let the mountain profile be given by the truncated Fourier series:

$$h(x) = z_*(A_0 + \sum_{n=1}^{50} A \cos nx) \qquad , \qquad (2.14a)$$

where

$$A_0 = 1/4 \qquad , \qquad (2.14b)$$

$$A_n = \frac{\sin n\pi/2}{n\pi(4-n^2/4)} \qquad , \qquad (2.14c)$$

and $z_* = 1.5$ km. $A_2$ is evaluated by taking the limit of $A_n$ as $n$ approaches 2 and applying L'Hopital's Rule. The steady, forced solution computed along 45°N is given in Figure 2.3 for a 45° sector of the globe. A high pressure ridge is centered over the mountain, which is located at the center of the sector, and weak troughs are observed both upstream and downstream of the mountain.

When superposed upon a transient, growing wave, the forced solu-tion will cause a cyclonic disturbance to appear more intense both on the upstream and downstream side of the mountain, and to appear weaker over the mountain. To demonstrate this effect, a developing free Eady-wave of approximately the same scale as the forced wave (here, the global wave number $\mu_* = 8$) is taken at various stages of its evolution (Figure 2.4) and superposed on the steady solution. The resulting superposition (or combined solution) is shown in Figure 2.5. At t = 0, when the free

28
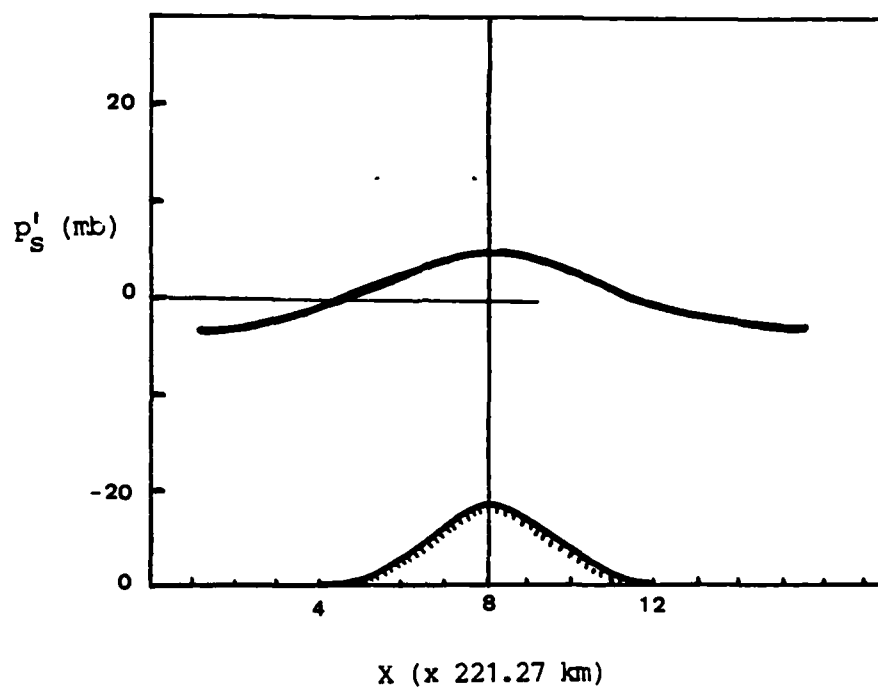
Figure 2.3. Steady, forced solution for the linear model presented as $p'_s$, the deviation from mean-state surface pressure, for a $45^0$ sector if the globe. Cyclic continuity is assumed at the east and west boundaries of the sector. Profile of the mountain given by (2.14) is included at bottom.

29
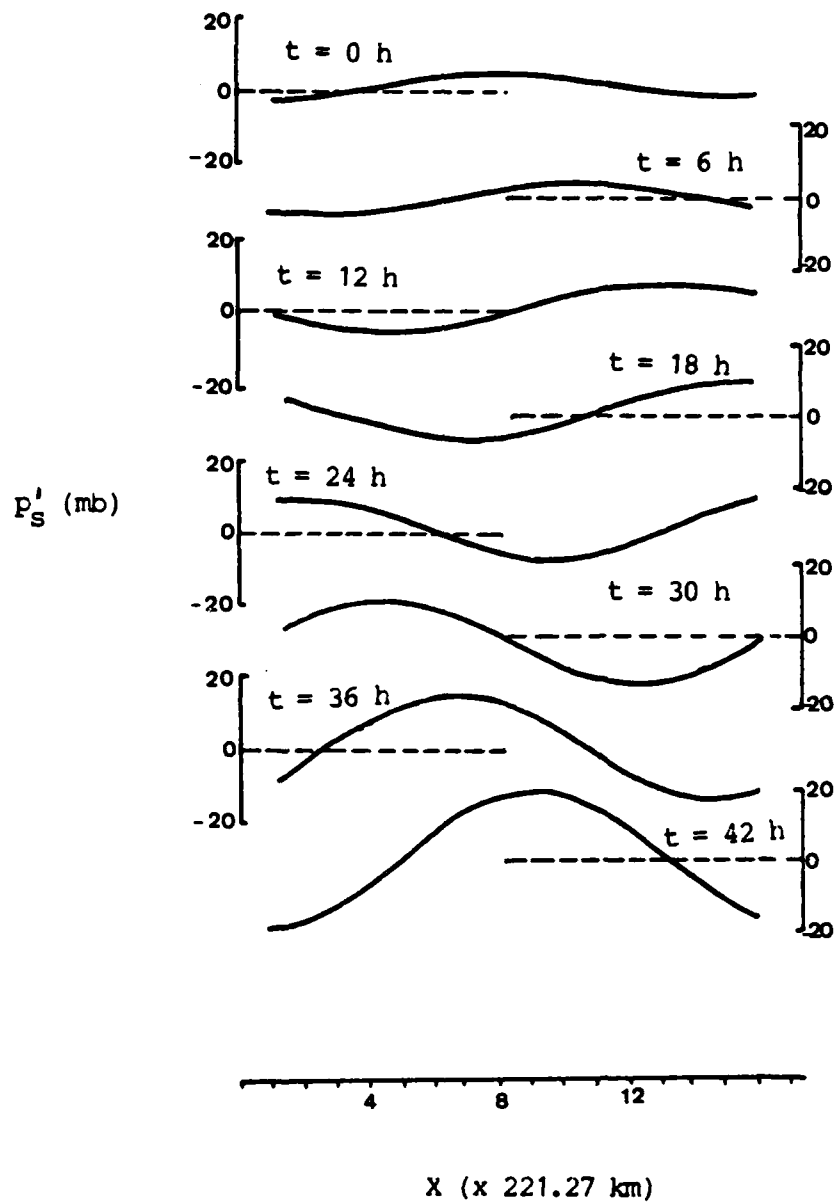
Figure 2.4.    Transient, free solution for the linear model given by
               (2.1, 2.5) presented as $p_s'$ for a 45° sector of the globe.
               Curves are given at six-hourly time intervals at 45°N.
               Cyclic continuity is assumed at the east and west boundaries
               of the sector.
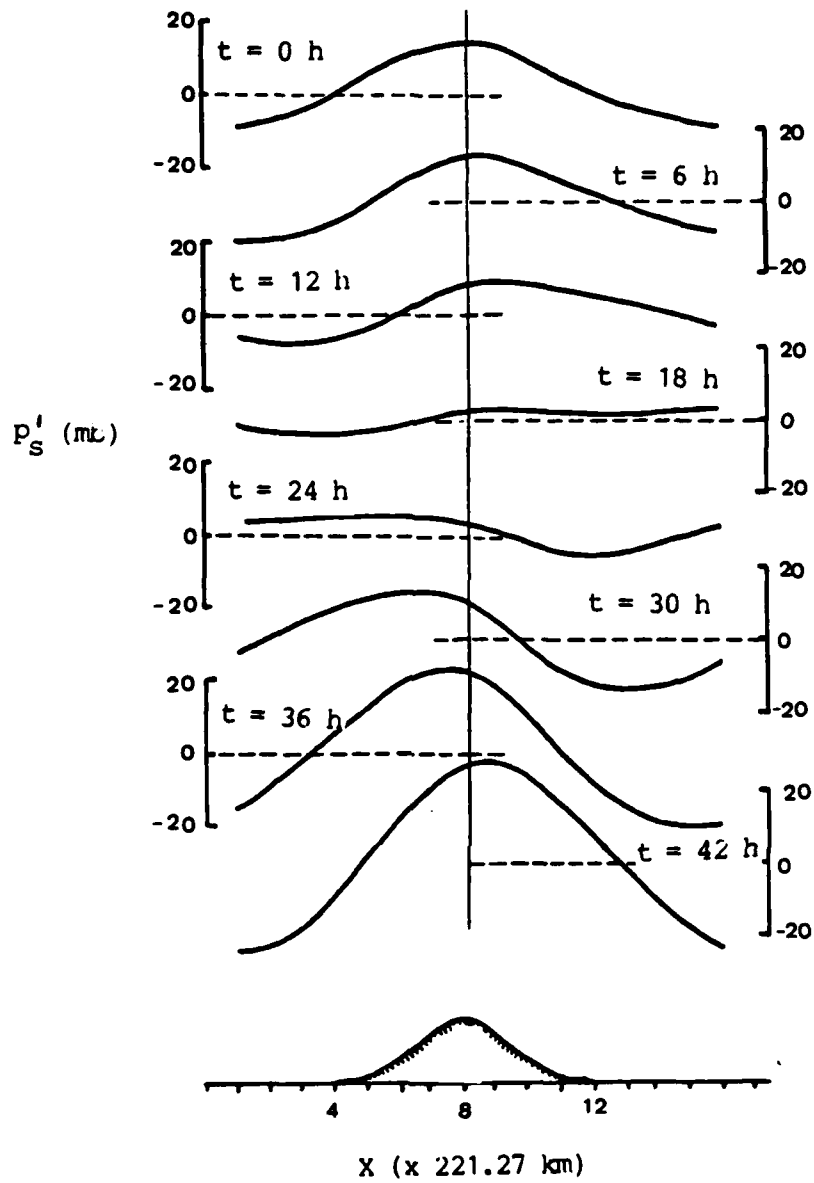
Figure 2.5.  As in Figure 2.4, except for combined (free + forced) linear model solution.  Profile of the mountain given by (2.14) is included at the bottom.

and forced solutions are in phase, the combined solution exhibits a larger amplitude ridge-trough pattern than the free solution alone. As the developing wave moves toward the mountain (at t = 6 and 12 h), the amplitude of the combined solution decreases indicating an apparent weakening, while the amplitude of the free solution continues to grow. As the wave reaches the top of the mountain (at t = 18 h), it is almost completely cancelled in the combined solution by the forced ridge and only weak troughs are observed on the upstream and downstream sides of the mountain. The cancellation would be exact if the wavelength and amplitude of the mountain were the same as, and out of phase with, the wave. Between t = 18 and t = 30 h, rapid deepening of the lee-side trough is apparent in the combined solution as the free wave moves east of the mountain and into phase again with the forced solution. When the combined solution is viewed in isolation, it appears as if a well-developed cyclonic disturbance dissipates as it approaches the mountain. Later, a lee-side disturbance appears to form and amplify rapidly as it moves down the mountain slope.

This behavior is very similar to observations preceding and during Rocky Mountain lee cyclogenesis. In a typical case (Palmen and Newton, 1969), a well-developed Pacific cyclone slows and weakens as it approaches the west coast of North America. As in the example above, an initially strong high pressure ridge centered over the Rockies appears to weaken considerably during the next 12-18 hours. However, cyclogenesis follows along the lee slopes as rapid deepening and slow eastward movement are observed during the first 6-12 hours after formation. As the cyclone moves away from the lee slopes, the intensification is less rapid

32

and the eastward phase speed increases. In the words of Palmen and Newton, the disturbance "behaves in a manner similar to a cyclone over flat terrain."

A plot (Figure 2.6) of minimum $p_s'$ versus time for the combined and free solutions, shows the major stages of this sequence quite well. From $t = 0$ to $t = 18$ h, the wave in the combined solution appears to weaken rapidly (as indicated by rising $p_s'$) and suggests a weakening surface cyclonic disturbance. Notice that during this period, the free solution continues to grow. From $t = 18$ to $t = 36$ h, pressure in the combined solution falls at a much faster rate than that of the free solution, which suggests a more rapid intensification. After $t = 36$ h, when the free wave is away from the mountain, the two solutions appear to deepen at the same rate.
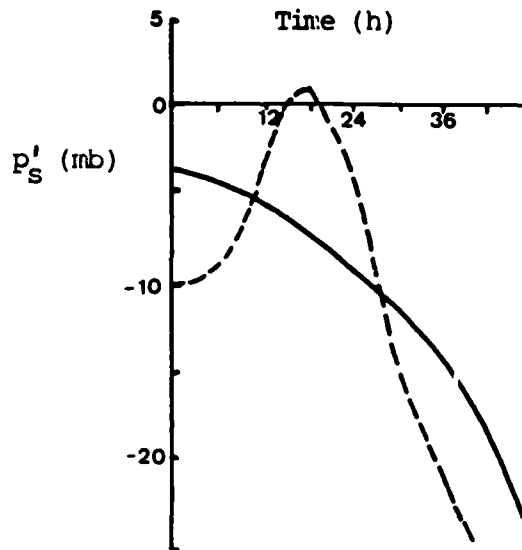


Figure 2.6. Minimum $p_s'$ versus time at 45°N for free (solid) and combined (dashed) linear model solutions.

The effect of the mountain on the phase of the combined solution is shown in Figure 2.7. As the disturbance approaches the mountain from t = 6 to 18 h, the phase speed of the combined solution is less than that of the free solution. That is, the trough appears to move more slowly as observed in Pacific cyclones approaching the windward slopes of the Rockies. From t = 24 h, when the lee trough is first observed in the combined solution, to t = 36 h, the phase speed of the combined solution is less than that of the free solution. This agrees with the observation that the lee cyclone moves more slowly during the 6-12 hour period after formation over the mountain slope. After t = 36 h, the phase-versus-time curves become coincident, which indicate that the disturbance moving away from the mountain has a phase speed characteristic of a cyclone over flat terrain.
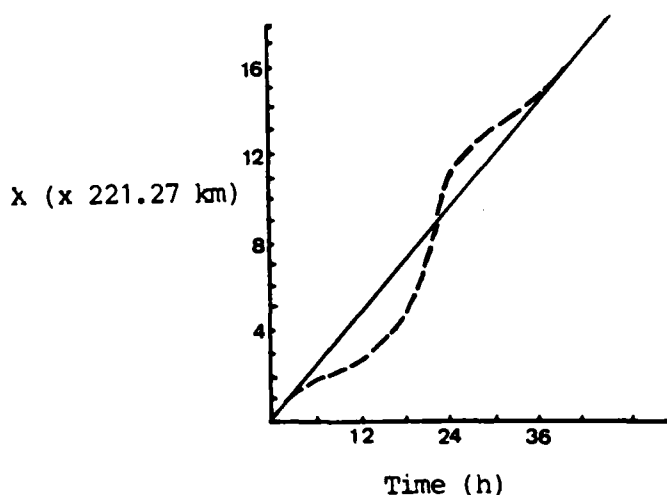


Figure 2.7. Phase versus time for free (solid) and combined (dashed) linear model solutions. Phase is inferred from the location of the minimum value of $p_s'$ at 45°N.

It is emphasized that this model is a linear one and does not include potentially important nonlinear effects. For example, this model requires that the mountain be of a small amplitude so that its effect on the mean flow and the developing wave may be ignored. In reality, the Rocky Mountain massif does affect the basic airflow. However, the success of this conceptual model in describing at least qualitatively the major features of lee cyclogenesis indicates the importance of linear dynamics in the lee cyclogenesis process.

## C.  NON-GEOSTROPHIC MODEL WITH FINITE-AMPLITUDE FORCING

In the preceding section, the analysis was accomplished with the quasi-geostrophic equations and did not consider ageostrophic advections. The semi-geostrophic equations described by Hoskins (1975) provide a set of equations which is capable of describing nongeostrophic processes such as frontogenesis (Hoskins and Bretherton, 1972). This equation set is formed by approximating the momentum geostrophically in the equations of motion while retaining the complete advecting wind. With a transformation of horizontal coordinates, the quasi-geostrophic equations are obtained in the new coordinate system. If the quasi-geostrophic equations are linear for the problem, these transformed equations are linear and may be solved analytically. The solution must then be transformed back to physical space for interpretation. The general development which follows in section 1 is similar to Bannon (1984) who used the semi-geostrophic equations to study the interaction of a front with an infinitely long mountain range. In his study, there was no vertical shear in the basic current and the frontogenesis was driven by horizontal

35

deformation. Bannon also used an unbounded atmosphere, while in this study, a lid is placed at the non-dimensional height $z = 1$.

1. Model Formulation

As before, consider a Boussinesq fluid. The potential vorticity equation may be written in Cartesian coordinates (with $z = -\ln p/p_S$) as follows:

$$\frac{dQ}{dt} = 0 \quad , \quad (2.15)$$

where

$$Q = \frac{\partial u}{\partial z}\frac{\partial \theta}{\partial y} - \frac{\partial v}{\partial z}\frac{\partial \theta}{\partial x} + (f_0 + \frac{\partial v}{\partial x} - \frac{\partial u}{\partial y})\frac{\partial \theta}{\partial z} \quad . \quad (2.16)$$

The semi-geostrophic approximation is made by replacing $(u,v)$ by $(u_g,v_g)$ in (2.16).

Using the mean wind of the preceding section, let $u_g = U = U_S + Sz$, where $U_S$ and $S$ are constants. Equation (2.15) may then be re-written as

$$\frac{dq}{dt} = 0 \quad , \quad (2.17)$$

where

$$q = -\frac{\partial v_g}{\partial z}\frac{\partial \theta}{\partial x} + (f_0 + \frac{\partial v_g}{\partial x})\frac{\partial \theta}{\partial z} \quad . \quad (2.18)$$

Here, the first term on the right-hand side of (2.16) does not appear because it is independent of time. If the geostrophic angular momentum, $M = v_g + fx$, is introduced, the potential vorticity equation becomes

36

$$q = - \frac{\partial M}{\partial z} \frac{\partial \theta}{\partial x} + \frac{\partial M}{\partial x} \frac{\partial \theta}{\partial z} \equiv \frac{\partial(M,\theta)}{\partial(x,z)} \qquad (2.19)$$

The Hoskins geostrophic coordinate system is introduced with

$$X = x + \frac{v_g}{f_o}, \quad Z = z, \quad T = t \qquad (2.20)$$

The associated transformation formulas are:

$$\frac{\partial}{\partial x} = \frac{\eta}{f_o} \frac{\partial}{\partial X} \qquad (2.21)$$

$$\frac{\partial}{\partial z} = \frac{g}{f_o^2 \theta_o} \left(\frac{\eta}{f_o}\right) \frac{\partial \theta}{\partial x} \frac{\partial}{\partial X} + \frac{\partial}{\partial Z} \qquad (2.22)$$

where $\qquad n = f_o + \frac{\partial v_g}{\partial x} = \dfrac{f_o}{1 = \dfrac{1}{f_o} \dfrac{\partial v_g}{\partial X}} \qquad (2.23)$

If $\Phi$, the geopotential in transform space, is defined as

$$\Phi = \phi + \frac{v_g^2}{2}$$

where $\phi$ is the geopotential in physical space, it follows that

$$f_o v_g = \frac{\partial \Phi}{\partial X}, \text{ and } \frac{g\theta}{\theta_o} = \frac{\partial \Phi}{\partial Z} \qquad (2.24)$$

37

If the initial v is very small, then the potential vorticity will be constant, and according to (2.17), it will remain constant. Consequently, by (2.18),

$$q = q_c = f_0 \frac{\partial \bar{\theta}}{\partial z} \qquad . \qquad (2.25)$$

The potential vorticity equation may be transformed into the geostrophic coordinate system as follows:

$$q = \frac{\partial(M,\theta)}{\partial(x,z)} = \frac{\partial(M,\theta)}{\partial(X,Z)} \frac{\partial(X,Z)}{\partial(x,z)} = \frac{\eta}{f_0} \frac{(M,\theta)}{\partial(X,Z)} \qquad , \qquad (2.26)$$

and since $M = f_0 X$,

$$q = \eta \frac{\partial \theta}{\partial Z} \qquad . \qquad (2.27)$$

Combining (2.23), (2.25), and (2.27), it follows that

$$f_0 \frac{\partial \bar{\theta}}{\partial z} = \frac{f_0 \frac{\partial \theta}{\partial z}}{1 - \frac{1}{f_0} \frac{\partial v_g}{\partial X}} \qquad . \qquad (2.28)$$

and, using (2.24), this may be written

$$f_0 \frac{\partial \bar{\theta}}{\partial z} = \frac{1}{f_0} \frac{\partial \bar{\theta}}{\partial z} \frac{\partial^2 \Phi}{\partial X^2} + \frac{f_0 \theta_0}{g} \frac{\partial^2 \Phi}{\partial Z^2} \qquad . \qquad (2.29)$$

38

Now, it is convenient to remove the basic stratification by writing

$$\Phi = \bar{\Phi}(z) + \Psi \qquad , \qquad (2.30)$$

where
$$\frac{\partial \bar{\Phi}}{\partial Z} = \frac{g\bar{\theta}}{\theta_o} \quad .$$

Substituting this into (2.29) results in the following

$$\frac{\partial^2 \Psi}{\partial X^2} + \frac{f_o^2 \theta_o}{g \, \partial\bar{\theta}/\partial z} \frac{\partial^2 \Psi}{\partial Z^2} = 0 \qquad , \qquad (2.31)$$

which states that the disturbance potential vorticity is zero. The time evolution, then, must come from the first law of thermodynamics,

$$\frac{d\theta}{dt} = 0, \text{ applied at boundaries } z = z_S \text{ and } z - 1.$$

The total derivative in the transform space may be written

$$\frac{d\theta}{dt} = \frac{\partial \theta}{\partial T} + \dot{X} \frac{\partial \theta}{\partial X} + \dot{Y} \frac{\partial \theta}{\partial y} + \dot{Z} \frac{\partial \theta}{\partial Z} \qquad . \qquad (2.32)$$

Using (2.20), $\dot{X}$ can be written

$$\dot{X} = \dot{x} + \frac{1}{f_o} \dot{v}_g = u - (u - u_g) = u_g \qquad , \qquad (2.33)$$

39

where the semi-geostrophic momentum equation has been used to evaluate $v_g$. The first law of thermodynamics now becomes

$$\frac{\partial \theta}{\partial T} + (U_s + Sz) \frac{\partial \theta}{\partial X} - \frac{f\theta_0}{g} Sv + \dot{Z} \frac{\partial \theta}{\partial Z} = 0 \qquad . \qquad (2.34)$$

At the upper boundary,

$$\dot{Z} = 0 \quad \text{at} \quad Z = 1 \qquad . \qquad (2.35)$$

Following Bannon (1984), the lower boundary condition is linearized by applying it at $Z = 0$ rather than $z_s$, and by replacing

$$\frac{\partial \theta}{\partial Z} \quad \text{by the constant} \quad \frac{\partial \bar{\theta}}{\partial Z}$$

*The forced vertical motion is given by*

$$\dot{Z} = \frac{dh_s}{dt} = \dot{X} \frac{\partial h_s}{\partial X} = \dot{U} \frac{\partial h_s}{\partial X} \qquad . \qquad (2.36)$$

Notice that the boundary condition, itself, is not linearized; it becomes linear as a result of the assumption that $z_s = 0$.

Since the interior equation is linear and the boundary conditions are linear, the solution may be separated into a steady-state forced solution and a free solution:

$$\Psi = \Psi_M(X,Z) + \Psi_F(X,Z,T) \qquad . \qquad (2.37)$$

40

The mountain solution, $\Psi_M$, satisfies

$$\frac{\partial^2 \Psi_M}{\partial X^2} + \frac{f_0^2 \, \theta_0}{g \, \partial\bar{\theta}/\partial z} \frac{\partial^2 \Psi_M}{\partial Z^2} = 0 \qquad , \qquad (2.38a)$$

and the boundary conditions:

$$(U_s + S) \frac{\partial}{\partial X} \frac{\partial \Psi_M}{\partial Z} - S \frac{\partial \Psi_M}{\partial X} = 0 \qquad , \ Z = 1 \qquad (2.38b)$$

$$U_s \frac{\partial}{\partial X} \frac{\partial \Psi_M}{\partial Z} - S \frac{\partial \Psi_M}{\partial X} = - \left(\frac{g}{\theta_0} \frac{\partial\bar{\theta}}{\partial z}\right) U_s \frac{\partial h_s}{\partial X} , \ \ Z = 0 \qquad (2.38c)$$

The free solution must satisfy

$$\frac{\partial^2 \Psi_F}{\partial X^2} + \frac{f_0^2 \, \theta_0}{g \, \partial\bar{\theta}/\partial z} \frac{\partial^2 \Psi_F}{\partial Z^2} = 0 \qquad , \qquad (2.39a)$$

and the boundary conditions:

$$\left[\frac{\partial}{\partial T} + (U_s + S) \frac{\partial}{\partial X}\right] \frac{\partial \Psi_F}{\partial Z} - S \frac{\partial \Psi_F}{\partial X} = 0 \quad , \ Z = 1 \qquad (2.39b)$$

$$\left[\frac{\partial}{\partial T} + U_s \frac{\partial}{\partial X}\right] \frac{\partial \Psi_F}{\partial Z} - S \frac{\partial \Psi_F}{\partial X} = 0 \qquad , \ Z = 0 \qquad (2.39c)$$

Notice that the lower boundary condition for the free solution follows from setting $\dot{Z} = 0$ at $Z = 0$. Both sets of equations are quasi-geostrophic in _transform_ space. Consequently, the mountain solution is given in transform space by (2.13), which gives a high-pressure ridge over the crest of the mountain which decays with height. The free solution in transform space leads to the Eady (1949) baroclinic instability solutions (2.1, 2.5), although the continuous modes (Pedlosky, 1964; Farrell, 1982) are required for complete solutions. In transform space, the mountain solution and the free solution do not interact. The interaction occurs in physical space as expressed through the coordinate transformation (2.20).

## 2. Model Application

Consider the interaction between a small-amplitude, baroclinic wave and the flow forced by a finite-amplitude mountain. This requires that

$$v_M \gg v_F \qquad (2.40)$$

and, consequently

$$V(X,Z,T) \doteq V(X,Z) = v_M \qquad (2.41)$$

The coordinate transformation (2.20) now becomes

$$X = x + \frac{V(X,Z)}{f} \quad , \quad Z = z \quad , \quad T = t \qquad (2.42)$$

42

The solutions to (2.38) and (2.39) are transformed to physical space with (2.42). In this case, the transformation is independent of time because it is controlled by the steady mountain solution.

The effect of the mountain on the amplitude of the disturbance may be seen by considering the effect of the transformation on the geopotential. In physical space, the pressure function, $\phi$, will change according to

$$\phi = \Phi = \frac{v^2}{2} \qquad . \qquad (2.42)$$

In this application, $v \doteq V_M(X,Z)$, so that (2.43) may be rewritten as:

$$\phi(X,Z,T) \doteq \Phi(Z) + \Phi_M^!(X,Z) - \frac{V_M^2(X,Z)}{2} + \Phi_F^!(X,Z,T) - V_M(X,Z)V_F(X,Z,T) \qquad (2.44)$$

This indicates that the primary effect of the onographically forced solution is "felt" by the time-dependent, mountain term, $\Phi_M^!$, because of the squared term. The time-dependent $V_M V_F$ term indicates that an orographic effect is present. However, there is no orographic effect on amplitude at the base of the free trough where $V_F = 0$. Consequently, changes in amplitude (other than those due to the free wave) as the wave moves across the mountain are due to the superposition of the forced and free solutions. After the wave moves away from the mountain, its amplitude will be the same as if there had been no mountain. In other words, for the assumptions made above, a finite-amplitude mountain has no effect on the growth of a small-amplitude baroclinic wave. Even over the

43

mountain, the minimum $\Phi_F^!$ (where $\Phi_F^!$ is the time-dependent part of $\Phi$) is the same whether or not it is over the mountain. Only its location will be affected by the mountain.

The effect of the mountain on the phase of the disturbance may be seen by diffentiating (2.42) with respect to X:

$$\frac{\partial x}{\partial X} = 1 - \frac{1}{f_0} \frac{\partial v}{\partial X} \qquad \qquad (2.45)$$

This result indicates that the horizontal dimension of the solution will be stretched in physical space when

$$\frac{\partial v}{\partial X} < 0 \text{ and compressed when } \frac{\partial v}{\partial X} > 0 \qquad .$$

In physical terms, the stretching of the horizontal dimension corresponds to a phase acceleration of the solution, and the compression represents a deceleration. These effects are caused by $U_M$, the divergent component of the wind, which is forced by the mountain. The divergent component $U_M$, is a maximum at the mountain top because there is divergence on the up-wind side and convergence on the downwind side. Consider Figure 2.8 in which the solution $V_M(X,0)$ is plotted in transform space for a mountain profile $H_S(X)$. The mountain forces a northward deflection of the wind ($V_M > 0$) on the windward side and a southward deflection on the leeward side. If $-X_1$ and $+X_1$ represent the points at which

$\frac{\partial V_M}{\partial X} = 0$, a wave will be decelerated when it is west of $-X1$,
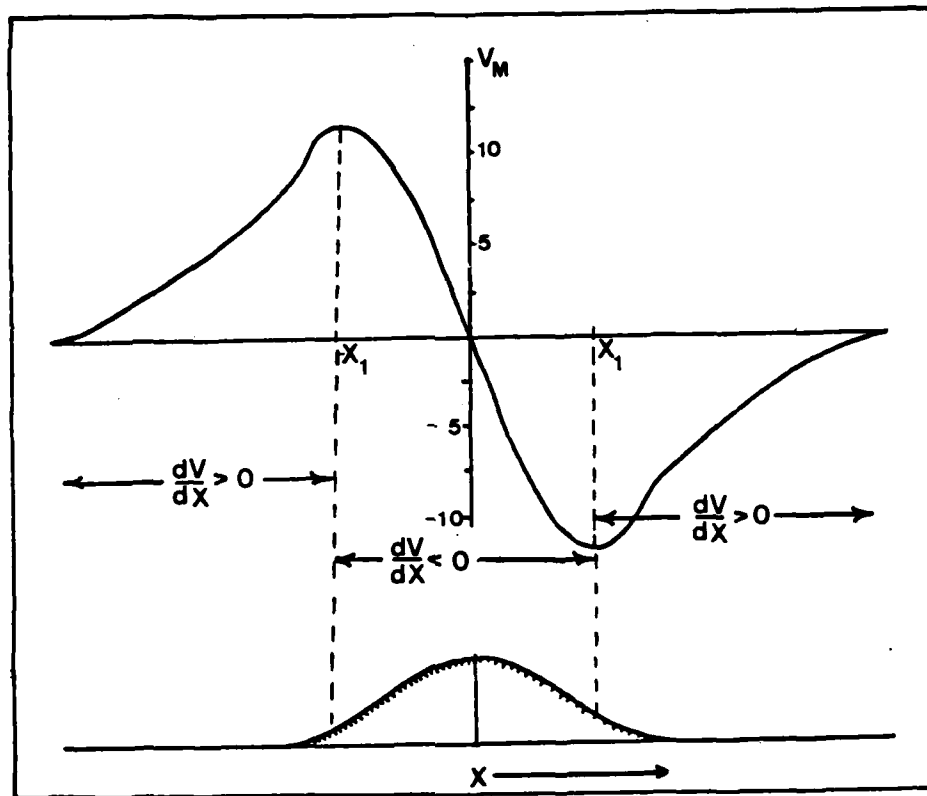
Figure 2.8.  Steady, forced solution of the semi-geostrophic model, $V_M$, in transform space. At the points $-X_1$ and $+X_1$, $\partial V_M/\partial X = 0$; these points separate the region of phase acceleration from the regions of deceleration.

accelerated when it is between $-X_1$ and $+X_1$ (over the mountain), and decelerated again when it is east of $+X_1$.

The phase acceleration may be seen by comparing the free solution (of (2.38)) in transform space and physical space. As indicated previously, the free solution is given by (2.1, 2.5). It is transformed to physical space by reversing the Hoskins transformation to obtain

$$x = X - \frac{V_M(X,Z)}{f_0} \quad , \quad z = Z \quad , \quad t = T \quad , \quad (2.46)$$

45

where $V_M$ is computed by taking the derivative of (2.9, 2.13) with respect to X. The solutions in transform space and physical space may then be computed using the same constants as in section II.B.2, except $z_\star$ = 3.0 km. The result is shown in Figure 2.9. The horizontal scale of the developing Eady wave is approximately the same as the scale of the mountain (global wave number $\mu_\star$ = 8). To focus on the acceleration caused by the mountain, the trough in transform space is initially positioned in phase with the trough in physical space at the point $X = -X_1$. This point where the acceleration effect begins is determined analytically using (2.42). In this way, the phase difference between the two troughs on the lee side of the mountain will be a maximum.

As the wave begins to move up the mountain slope (t = 6 h), evidence of acceleration is already present in the physical solution. At t = 12 h, when the trough in transform space reaches the top of the mountain, the trough in physical space is located half-way down the lee side of the mountain. At t = 18 h, the trough in transform space has moved over the le          trails the trough in physical space by nearly 500 km.          di   ence has decreased by t = 24 h, which indicates that     .r        sical spac  as slowed. This effect on phase speed is caus        ivergent component of the wind which is forced by the mou.       annon (1984) obtained similar results with a front moving over  mountain range. After the disturbance moves away from the mountain and $V_M(X,Z) \rightarrow 0$, the phase speed of the physical solution is approximately the same as that of the transform solution, and the lee disturbance now behaves similar to a cyclone over flat terrain.
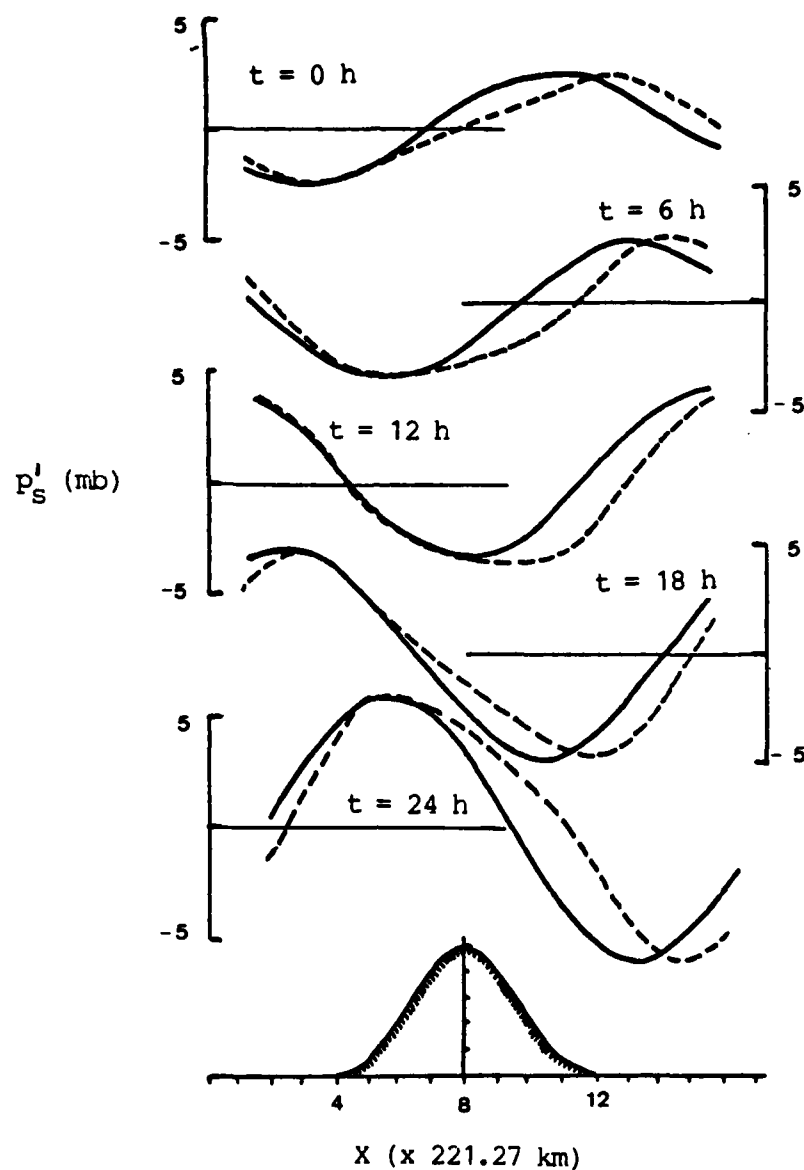
Figure 2.9. Semi-geostrophic model solutions presented as $p_s'$ along 45°N in transform space (solid) and in physical space (dashed). The 3.0km mountain is included at the bottom.

This latter result is similar to that discussed in the preceding section, but, in this case, the acceleration and deceleration of the disturbance is actually caused by the interaction with the mountain. As the disturbance moves down the lee slope and away from the mountain it is

decelerated and moves more slowly than a similar disturbance over flat terrain. After the disturbance has left the mountain's influence, its phase speed increases to that of the disturbance over flat terrain. As in the preceding section, a relatively simple model has been used to describe key aspects which are observed in Rocky Mountain lee cyclogenesis.

The results of this chapter suggest that the cyclogenesis which is observed in the lee of the Rocky Mountains is largely unaffected dynamically by the presence of the mountain. In both models, the rapid intensification which is characteristic of lee cyclogenesis is observed as the disturbance moves down the lee slope of the mountain. However, in neither model is there a net orographic effect on the amplitude of the disturbance. The characteristic phase behavior of cyclonic disturbances on both the windward and leeward sides of the mountain is also observed in these models. In the linear model, the effect was due to superposition of two solutions; in the semi-geostrophic model, the larger mountain affects the phase speed of the wave. However, after the disturbance has moved away from the mountain, it shows no net orographic effect. The success of these models in explaining the major features of Rocky Mountain lee cyclogenesis suggest that it is a manifestation of simple baraclinic instability distorted by the mountain - and not any new or enhanced instability mechanism. This idea will be tested in Chapters V and VI where the primitive equations are integrated with more realistic initial conditions.

48

## III. ATMOSPHERIC MODELS

Two atmospheric prediction models are used in this study: the UCLA general circulation model described by Arakawa and Lamb (1981) and the Naval Environmental Prediction Research Facility (NEPRF) global spectral model developed by Dr. T. Rosmond. These two models represent state-of-the-art atmospheric research models and have many desirable features.

The UCLA model is designed specifically to provide an accurate representation of air flow over and near topography. The basic numerical scheme was developed for the shallow water equations which conserve absolute potential vorticity. The UCLA finite-difference scheme is designed to conserve the domain-averaged potential vorticity while it approximately conserves the potential vorticity of individual parcels. Arakawa and Lamb (1981) have shown that, for a given coarse grid, simulations of the airflow over steep topography improved significantly when this scheme is used. In this study, airflow over a long, narrow mountain is considered, and it is believed that the UCLA model provides the best available representation.

The NEPRF model is a spectral version of the 1977 UCLA model. Although it is not explicitly designed to conserve the domain-averaged potential vorticity, it is quite accurate because of the spectral representation. It is used in this study to investigate the continuous-mode growth mechanism. Because this mechanism is a linear one, a linearized model is sufficient for the investigation. The NEPRF model was selected primarily because it can be linearized more easily and run more

49

rapidly than a comparable finite-difference model. Since the physics are very similar to those of the UCLA model, the results should be about the same. Additionally, the fully nonlinear version of the NEPRF model can be used as a check on the effect of truncation errors in the finite-difference runs. The following sections describe these two models and the integration schemes used.

## A.  THE UCLA MODEL

The UCLA general circulation model is described in detail by Arakawa and Lamb (1977, 1981). A short summary of the version used in this study is provided here. The model consists of the primitive equations for an inviscid, adiabatic, and hydrostatic atmosphere; moisture and its effects are not included. The prognostic variables are the horizontal components (u, v) of the wind velocity, potential temperature ($\theta$), and pressure ($\pi = p_s - p_t$). The model's vertical coordinate is $\sigma$, which is defined as

$$\sigma = \frac{p - p_t}{p_s - p_t} \quad . \qquad , \qquad (3.1)$$

where $p_s$ is surface pressure and $p_t$ is the top of the model atmosphere. In this study, $p_t = 200$ mb. Channey and Drazin (1961) have shown that wavelengths shorter than planetary scale are trapped in the vertical. In addition, the results of Section II.B (Figure 2.2) indicate that the onographic wave is strongly damped in the vertical. Consequently, model solutions should not be significantly affected by the boundary at 200 mb.

50

The domain is a 45º sector of the Northern Hemisphere with a wall at the equator and cyclic continuity at the east and west boundaries. The model atmosphere extends from the earth's surface to 200 mb, and $\dot\sigma$ is assumed to vanish at both of these boundaries. The variables are staggered horizontally according to Arakawa's Scheme C (Figure 3.1) with a grid spacing of approximately 2.8º longitude by 2.75º latitude. Variables are staggered vertically as shown in Figure 3.2 in six layers spaced equally in $\sigma$. Rennick and Williams (1985) have shown that with an upper boundary at 200 mb, the equal spacing in $\sigma$ gives well-behaved results for the forced mountain solution at the horizontal scales considered in this study. Spatial derivatives are approximated using a fourth-order finite difference scheme. The vertical differencing scheme, which was developed by Arakawa and Suarez (1983), has excellent integral properties and it eliminates the systematic error in the hydrostatic equation which was present in previous models. A nonlinear horizontal diffusion of momentum is included to parameterize the effects of subgrid-scale motions.
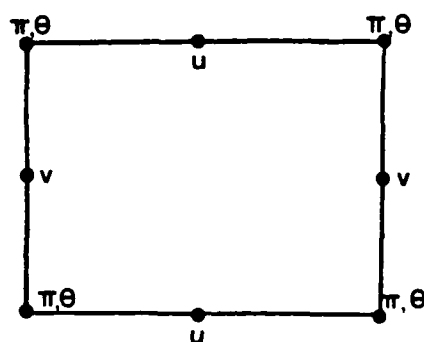


Figure 3.1. Horizontal distribution of variables in the UCLA model grid.

51

```
p=200mb ——— σ = 0 ——————————— φ ; σ̇=0
          — — — — — — — u,v,θ— — —
          ———————————————————— φ,σ̇
          — — — — — — — u,v,θ— — —
          ———————————————————— φ,σ̇
          — — — — — — — u,v,θ— — —
          ———————————————————— φ,σ̇
          — — — — — — — u,v,θ— — —
          ———————————————————— φ,σ̇
          — — — — — — —·— u,v,θ— — —
          ———————————————————— φ,σ̇
          — — — — — — — u,v,θ — — —
p=pₛ ——— σ = 1 ——————————— φ,σ̇=0
```
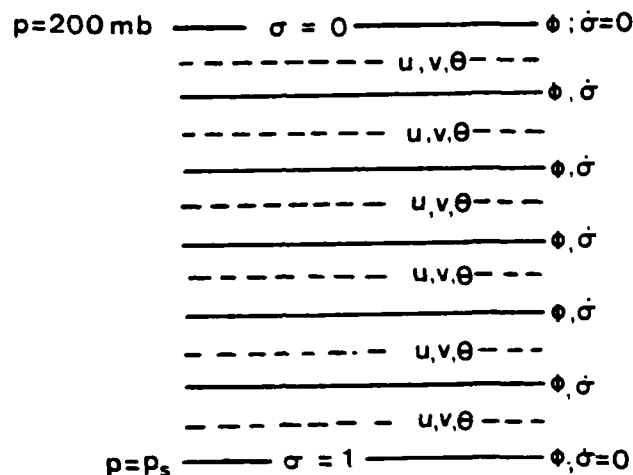
Figure 3.2.  Vertical distribution of variables in the six-layer version
             of the sigma-coordinate system.


The model integration proceeds in a series of Euler-backward time
steps followed by five centered time steps.  Convergence of the meridians
toward the poles would normally require the use of an extremely short
time step to maintain computational stability.  To avoid this require-
ment, the zonal smoothing technique described by Arakawa and Lamb (1977)
is used.  In this technique a local stability criterion, S, is used; it
is defined as follows:

$$S = (\Delta\lambda/\Delta\phi)\cos\phi / \sin(n\Delta\lambda/2) \quad (\Delta t_*/\Delta t) \tag{3.2}$$

where $\Delta\lambda$ = longitudinal grid size, $\Delta\phi$ = latitudinal grid size,
$\Delta t_*$ = 360 s, $\Delta t$ = time step, and n = wave number.

Smoothing is performed only when $S < 1$; this occurs generally at high latitudes and for higher wave numbers. The smoothing is accomplished by reducing the amplitudes of the Fourier components of the zonal pressure gradient and the zonal mass flux by the factor S. As indicated by (3.2), the amount of smoothing may be reduced by decreasing the time step. To measure the effect of the zonal smoothing on the features of interest in this study, runs were made in which a westerly mean flow was forced over a 1.5 km mountain using three-, six-, and ten-minute time steps. Comparison of the 36-h forecasts of surface pressure and 500 mb vorticity revealed virtually no differences between the solutions with three- and six-minute time steps. Therefore, it was concluded that a six-minute time step was adequate.

B. THE NEPRF SPECTRAL MODEL

A linearized form of the NEPRF spectral model is used in this study to investigate the continuous-mode growth mechanism. A short summary of the basic model and the version used in this study is presented in this section.

The spectral formulation was accomplished by Dr. T. Rosmond of NEPRF and is described by Lubeck, Rosmond and Williams (1977). The model's basic equations are obtained from the nonlinear primitive equations for an inviscid, adiabatic, and hydrostatic atmosphere. the prognostic variables are the horizontal components of the wind velocity (u, v); temperature (T); and the natural log of terrain pressure ($q = \ln p_s$). The variables are represented spectrally in the horizontal with wave number 40 triangular truncation. The model's vertical coordinate is $\sigma$, which is given by (3.1), with $p_t = 0$. The vertical derivatives are approximated

53

using finite differences. Vertical velocity, $\dot{\sigma}$, is assumed to vanish at the upper and lower boundaries. The model employs a semi-implicit time-differencing scheme which allows a 15-minute time step.

The version of the model used in this study is linearized according to Rennick and Williams (1985). This is accomplished by forcing the time tendencies to be zero at all wave numbers except the one of interest. The domain is restricted to one wavelength in the east-west direction, and cyclic continuity is assumed. To simulate the wall placed at the equator in the UCLA model, the Northern Hemisphere conditions are mirrored in the Southern Hemisphere. Six- and 20-layer versions of the model are used. A comparison of the results of these two versions will give an indication of the effect of the vertical resolution. The layers are spaced equally in $\sigma$. Rennick and Williams (1985) found that this spacing yields well-behaved solutions. Because the experiments are limited to the linear domain, the use of semi-implicit time-differencing allows a 30-minute time step.

## IV. INITIAL CONDITIONS AND TOPOGRAPHY

Many factors must be considered in the development of the initial conditions for experiments which treat the lee cyclogenesis problem. The wind shear (both vertical and horizontal) of the mean flow determines its stability and, consequently, plays a controlling role in the development of the cyclone. In addition, the vertical structure of the disturbance is critical to the rate at which mean kinetic energy is converted into eddy kinetic energy in a developing wave. Finally, as indicated by the climatology of cyclogenesis frequency, the size, scale and orientation of topography appear to play a role in the occurrence of cyclogenesis. Consequently, the initial conditions must be selected with care.

In this study, an attempt is made to reproduce the observed characteristics of lee cyclogenesis as closely as possible using analytical expressions. The structure of the mean flow is similar to that presented in Palmen and Newton (1969) in their description of cyclogenesis. The disturbance is specified using the results of Chapter II. The topography is patterned roughly after the Rocky Mountains. In the following sections, the specific analytical expressions and techniques used to initialize the model are described.

### A. MEAN FLOW

In this study, lee cyclogenesis is viewed as a mid-latitude manifestation of baroclinic instability. Consequently, the initial mean state for all experiments consists of a baroclinically unstable westerly current. The specific form of the upper-level wind is

55

$$\bar{u}_u[\phi, p(\sigma, \phi)] = \bar{u}_0 \text{sech}^2[\gamma(\phi - \phi_0)](\ln(p_s/p)/\ln(p_s/p_{max}) \qquad , \qquad (4.1a)$$

$$\bar{v}_u \phi, p(\sigma, \phi) = 0 \qquad , \qquad (4.1b)$$

where $\bar{u}_0 = 40 \text{ m s}^{-1}$, $\phi_0 = 45^{\circ}\text{N}$, $p_s = 1013.25$ mb, $p_{max} = 200$ mb, and $\gamma$ is the halfwidth of the jet. The maximum wind at each level occurs at $45^{\circ}\text{N}$. Wind speed varies linearly with the log of pressure and approximates profiles given by Palmen and Newton (1969) in case studies of cyclogenesis. The latitudinal variation is taken from Haltiner and Williams (1980). By setting the halfwidth of the jet, $\gamma$, equal to $8^{\circ}$ latitude, a horizontal profile which agrees quite well with that observed prior to cyclogenesis results. However, this profile meets the necessary condition for barotropic instability in regions to the north and south of the jet stream. Consequently, a profile in which $\gamma = 16^{\circ}$, that does not meet this criterion is included in this study to isolate the baroclinic effects. Meridional cross-sections of the two initial mean state velocity fields are shown in Figure 4.1.

A mean surface current is included with the same latitudinal structure as the upper-level flow,

$$\bar{u}_s(\phi) = \bar{u}_{00}\text{sech}^2[\gamma(\phi - \phi_0)] \qquad , \qquad (4.2a)$$

$$v_s(\phi) = 0 \qquad , \qquad (4.2b)$$

56
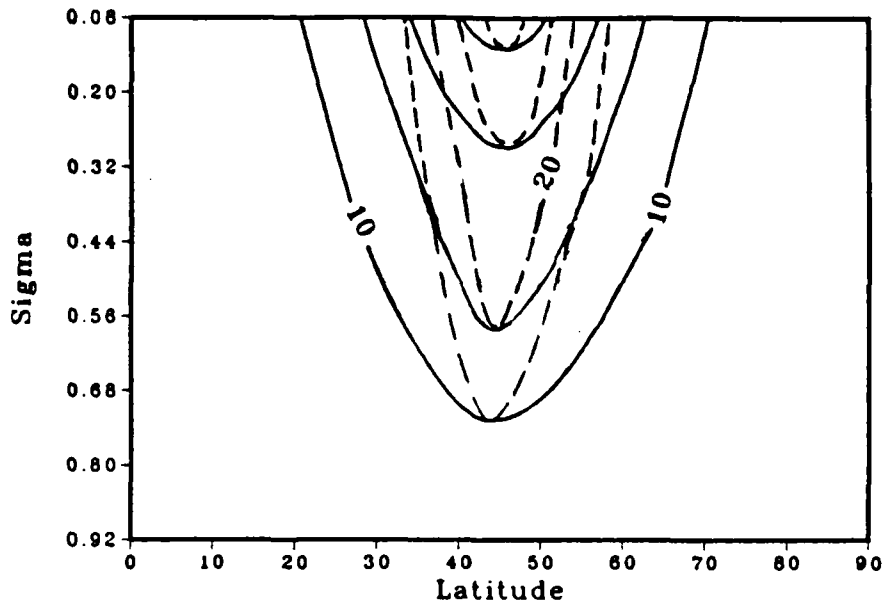
Figure 4.1. Meridional cross-sections of the initial mean wind, $\bar{u}$, for: a) $16^o$ jet, and b) $8^o$ jet. Contour interval is 10 m s$^{-1}$.

where $\gamma$ and $\phi$ are as defined above and $\bar{u}_{oo} = 5$ m s$^{-1}$. The upper-level wind given by (4.1) is modified by adding the surface current and applying the gradient correction to account for the earth's sphericity:

$$\bar{u}[\phi, p(\sigma,\phi)] = -\Omega a \cos \phi +$$
$$\Omega a \cos \phi[1+(2(\bar{u}_u + \bar{u}_s)/\Omega a \cos \theta)]^{0.5} \quad , \quad (4.3)$$

where $a$ is the radius of the earth, $\Omega$ is the earth's rotation rate, and $\bar{u}_u$ and $\bar{u}_s$ are given by (4.1a) and (4.2a), respectively.

57

Mean surface pressure and surface temperature are initialized from the mean surface wind using the geostrophic wind equation:

$$\bar{p}_S(\phi) = \exp[\ln \bar{p}_S(\phi_0) - (a/R) \int_{\phi_0}^{\phi} f u_S(\phi)/\bar{T}_S(\phi) \, d\phi] \, , \qquad (4.4)$$

where $\bar{p}_S(\phi_0 = 45^0 N) = 1013.25$ mb, $\bar{u}_S(\phi)$ is given by (4.2a), and $\bar{T}_S(\phi)$ represents the mean surface temperature. The integral in (4.4) is evaluated using a Simpson's rule approximation. Because the latitudinal structure of $\bar{T}_S(\phi)$ is unknown, $\bar{p}_S(\phi)$ is computed interatively as follows: an initial guess is made for $\bar{T}_S$; $\bar{p}_S(\phi)$ is computed using (4.4); $\bar{T}_S$ is then adjusted to the NACA standard temperature for the computed $\bar{p}_S$ and a new $\bar{p}_S(\phi)$ is derived; this latter step is repeated until the adjustment of $\bar{T}_S$ is less than $0.01^0 K$. The solution converges in approximately 10 iterations.

Upper-level temperature is specified by integrating the geostrophic thermal wind equation which gives:

$$\bar{T}(\phi,p) = \bar{T}(\phi_0,p) + (a/R) \int_{\phi_0}^{\phi} f(\partial u_u/\ln p) \, d\phi \qquad , \qquad (4.5)$$

where $\bar{T}_S(\phi_0,p)$ is the temperature at $45^0 N$ and $\bar{u}_u$ is given by (4.1). The integral in (4.5) is also evaluated using Simpson's rule.

58

These initial conditions were integrated over a flat lower boundary to test the balance of the mean state. Harmonic analysis of the v-component of the wind at all levels and at a variety of latitudes showed wave number zero amplitude fluctuations of less than 1 m s$^{-1}$.

B.  DISTURBANCE

Two types of disturbances are used in this study: a barotropic disturbance (amplitude and phase independent of height), and an orographically-forced disturbance which decays exponentially with height.  The barotropic disturbance is used in the majority of the experiments to study the effect of topography on the evolution of a baroclinic wave. The orographically-forced disturbance is used only in Chapter V to study the continuous-mode growth mechanism.

The barotropic disturbance consists of a weak wave which varies sinusoidally with longitude.  The maximum amplitude of the disturbance occurs at 45°N.  Fields are balanced geostrophically with a constaft f and are given by

$$\Phi' = f_0 \, A^* \sin(n\lambda)\sin^2(2\phi) \qquad , \qquad (4.6a)$$

$$p' = p\Phi'/RT \qquad , \qquad (4.6b)$$

$$u' = -(1/f_0 a) \; \partial\Phi'/\partial\phi \qquad , \qquad (4.6c)$$

$$v' = 1/f_0 a \cos \phi) \; \partial\Phi'/\partial\lambda \qquad , \qquad (4.6d)$$

$$T' = 0 \qquad , \qquad (4.6e)$$

where $\bar{T}$ = 273°K and $\bar{p}$ = 1013.25 mb.  Test integrations were conducted in which the initial wave number of the disturbance was varied to determine

59

the most unstable wavelength.  The wave number 8 perturbation exhibited the most rapid growth and is the one used in this study.

The orographically-forced disturbance is specified using the steady forced solution to Eady's model given by (2.9) and 2.13).  The fields are balanced geostrophically:

$$p_S' = -p/RT[(\gamma U_s h_s \epsilon^{\frac{1}{2}} \cos \mu x \sin^2(2\phi))/(H(U_s \alpha_E - S\epsilon^{\frac{1}{2}}\gamma_E))] \qquad , \qquad (4.7a)$$

$$u' = -\frac{\partial \psi'}{a\partial \phi} = \frac{U_s h_s \epsilon^{\frac{1}{2}}}{af_0 H(U_s \alpha_E - S\epsilon^{\frac{1}{2}}\gamma_E)} \left[ \alpha_E \sinh \frac{z}{\epsilon^{\frac{1}{2}}} + \right.$$
$$\left. \gamma_E \cosh \frac{z}{\epsilon^{\frac{1}{2}}} \right] \cos \mu x \ (2 \sin 4\phi) \qquad , \qquad (4.7b)$$

$$v' = \frac{\partial \psi'}{\partial x} = \frac{U_s h_s \epsilon^{\frac{1}{2}}\mu}{f_0 H(U_s \alpha_E - S\epsilon^{\frac{1}{2}}\gamma_E)} \left[ \alpha_E \sinh \frac{z}{\epsilon^{\frac{1}{2}}} + \right.$$
$$\left. \gamma_E \cosh \frac{z}{\epsilon^{\frac{1}{2}}} \right] \cos \mu x \ (2 \sin^2 2\phi) \qquad , \qquad (4.7c)$$

$$T' = \frac{1}{R} \frac{\partial \Phi'}{\partial Z} = -\frac{\Gamma U_s h_s}{RH(U_s \alpha_E - S\epsilon^{\frac{1}{2}}\gamma_E)} \left[ \alpha_E \cosh \frac{z}{\epsilon^{\frac{1}{2}}} + \right.$$
$$\left. \gamma_E \sinh \frac{z}{\epsilon^{\frac{1}{2}}} \right] \cos \mu x \ (\sin^2 2\phi) \qquad , \qquad (4.7d)$$

where $\Gamma = 1.167 \times 10^4 m^2 s^{-2}$, $U_s$ is the mean surface wind, $h_s$ is the terrain elevation, H = 8 km is the scale height of the atmosphere, and z is non-dimensional; height (here $Z = 1 - \sigma$).

## C. TERRAIN

The topography used in this study is designed to resemble the Rocky Mountains as a long, meridional barrier to westerly flow. It is given by

$$z_m(\phi,\lambda) = \begin{cases} z_*(\phi) \cos^2\left[\left(\dfrac{\lambda-\lambda_0}{4\Delta\lambda}\right)\dfrac{\pi}{2}\right] & , \quad |\lambda - \lambda_0| < 4\Delta\lambda \\[2em] 0 & , \quad |\lambda - \lambda_0| > 4\Delta\lambda \end{cases} \tag{4.8a}$$

where $\Delta\lambda$ is the longitudinal grid spacing and $\lambda_0$ is the longitude at which the mountain is centered; $z_*(\phi)$ is given by

$$z_*(\phi) = \begin{cases} z_s & , \quad \phi_N > \phi > \phi_S \\[1.5em] z_s \cos^2\left[\left(\dfrac{\phi-\phi_N}{3\Delta\phi}\right)\dfrac{\pi}{2}\right] & , \quad \phi_N + 3\Delta\phi > \phi > \phi_N \\[1.5em] z^s \cos^2\left[\left(\dfrac{\phi-\phi_s}{3\Delta\phi}\right)\dfrac{\pi}{2}\right] & , \quad \phi_S > \phi > \phi_S - 3\Delta\phi \\[1.5em] 0 & , \quad \text{elsewhere} \end{cases} \tag{4.8b}$$

where $z_s$ is the mountain height, $\Delta\phi$ is the latitudinal grid spacing, $\phi_N$ is approximately 61.75°N and $\phi_S$ is approximately 31.25°N. The resulting mountain (Figure 4.2) is 22.5° wide and extends from approximately 23°N to 70°N.

61
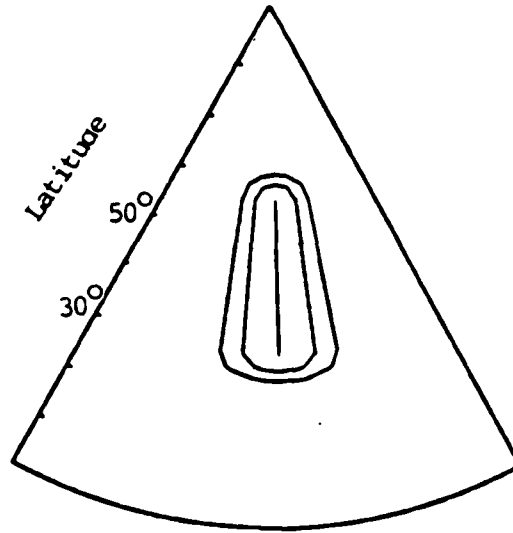
Figure 4.2.  Plan-view of the topography on a 45° sector of the globe. Vertical line at the center of the figure represents the mountain ridge line.

Terrain was initialized in the model by raising the mountain from zero to the values in (4.8) during the first 12 hours of the integration. This technique is designed to minimize the generation of inertia-gravity waves during the initial part of the integration while the mean flow, which is analytically balanced without topography, adjusts to the presence of the mountain.  Topography is incremented at each time step according to:

$$z_m(\lambda, \phi, t) = \begin{cases} z_{m*}(\lambda,\phi) \sin^2 \left(\dfrac{\pi t}{24}\right) & , \ t < 12 \text{ hours} \\ z_{m*}(\lambda,\phi) & , \ t > 12 \text{ hours} \end{cases} \qquad (4.9)$$

This technique has been used successfully by Tibaldi et al. (1980), Williams et al. (1981), and Walker (1982) and has been found to produce a smooth and rapid adjustment (within approximately 6-12 hours).

62

# V. CONTINUOUS-MODE GROWTH EXPERIMENTS

The results of Chapter II suggest that lee cyclogenesis may be inter-
preted as a manifestation of ordinary baroclinic instability distorted by
the mountain. In this chapter, the suggestion by Farrell (1982) that
continuous-mode growth plays a significant role in lee cyclogenesis is
considered. As indicated in Chapter I, the initial conditions are
crucial to this mechanism and must be based on a realistic flow. In this
study, the mean flow is assumed to contain no perturbations initially,
and, at the same time, t, a disturbance composed of a spectrum of dis-
crete and continuous modes is excited in response to orographic forcing.
This might be expected if the cross-topography flow increased rapidly
from zero. Two sets of numerical experiments are conducted in which an
orographically-forced disturbance is allowed to evolve for at least 24
hours in a baroclinically unstable mean flow. In the first set, a linear
model is used to examine the evolution of an orographically-forced dis-
turbance which is specified initially using the forced Eady solution
described in section II.B. Use of the linear model is justified because
the continuous-mode growth described by Farrell is a linear mechanism.
In the second set of experiments, the possibility is considered that the
structure of the orographically-forced disturbance is more complex than
the forced Eady solution. In these experiments, the forced disturbance
is not included in the initial conditions but develops during the inte-
gration in response to the mean flow being forced over the topography.

63

In addition, a nonlinear numerical model is used to include all possible orographic effects on the evolution of the continuous modes.

Results of these numerical experiments are examined for evidence of enhanced growth which could indicate a significant contribution to the amplification of the disturbance. According to Farrell's analysis, continuous-mode growth could occur for approximately 6-8 hours after excitation for the magnitude of vertical shear used in these experiments. Pedlosky (1964) has shown that, in the long term, these modes damp as $1/t^2$. Consequently, if the rapid algebraic growth predicted by Farrell is present, it should be evident within the first 24 hours of the integration.

A. EVOLUTION OF VERTICALLY TRAPPED DISTURBANCES IN A LINEAR MODEL

In this section, the excitation of an orographically-forced, vertically-trapped disturbance is considered as a possible trigger mechanism for rapid continuous mode growth. Numerical experiments are carried out in which the forced Eady solution described in section II.B is allowed to evolve in a baroclinically-unstable, zonal mean flow. Topography is not included because the continuous-mode-growth mechanism is linear, and, once excited, these modes grow independently of the mountain. In any case, the mountain solution is independent of time and it cannot interact with the disturbance since the model equations have been linearized.

The six-layer, linearized version of the NEPRF spectral model is used to carry out the experiments. The mean state is given by (4.3-4.5) with $\gamma = 8^0$, and the initial disturbance is given by (4.7a-d). The disturbance is allowed to evolve for at least 24 hours. Model runs are

64

carried out with global wave number $\mu_* = 8$, 12, and 16 because these wave numbers represent disturbance wavelengths of interest in studies of lee cyclogenesis.

The results of the wave number 8 experiment are shown in Figure 5.1. After an intial period in which the disturbance amplitude damps, amplification is observed at $\sigma = 0.9167$ (p $\doteq$ 930 mb) between t = 6 and 12 h. However, this growth is confined to the lowest level of the model and is not sustained beyong t = 12 hours. Little if any growth is observed at upper levels. The model run is extended to t = 60 h to see if the discrete mode growth predicted by baroclinic instability theory is observed. In Figure 5.2, the amplitude of v at $\mu_* = 8$ for level 6 is plotted versus time. Except for the growth spurt between t = 6 and 12 h noted above, virtually no growth is observed during the first 42 hours of the run. However, beginning at approximately t = 45 h, growth of the most unstable discrete mode is indicated by the rapid amplification.

The results of the wave number 12 and 16 experiments are shown in Figures 5.3 and 5.4, respectively. Behavior in both cases is roughly similar to that observed in the wave number 8 experiment. A small spurt of growth at the lowest level is observed in Figure 5.3 between t = 12 and 18 h between t = 6 and 12 h in Figure 5.4. Again, little if any growth occurs at higher levels.

Walker (1982) suggested that higher vertical resolution may be necessary to model the dynamics of lee cyclogenesis properly. Farrell (1982) has also shown that continuous-mode growth is favored in disturbances with higher wave numbers, which indicates that a higher vertical resolution may be necessary for the model. The three experiments
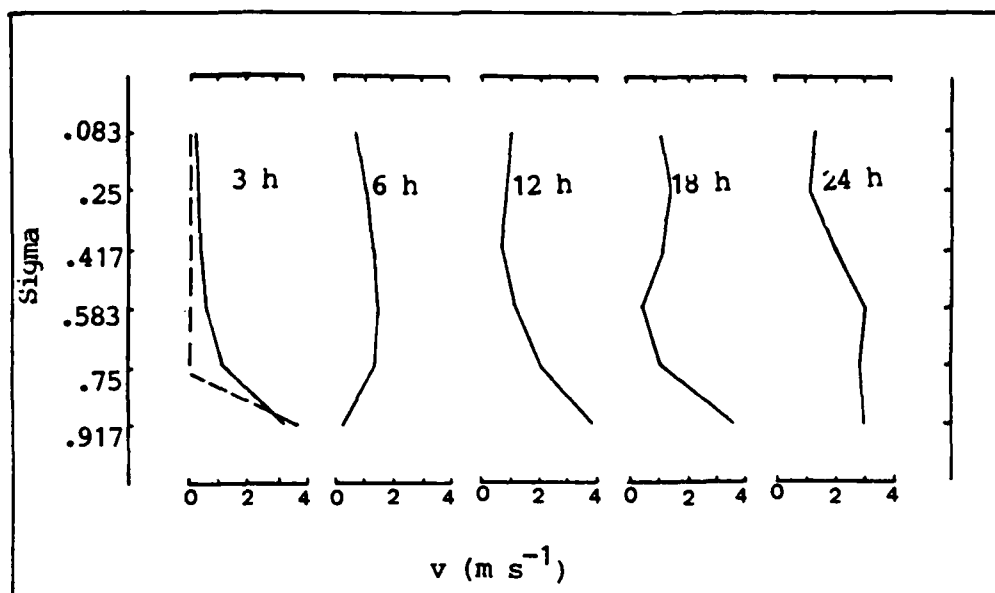
Figure 5.1. Amplitude of wave number 8 of v at 45°N as a function of σ for linear Experiment 1. Initial amplitude (dashed) versus σ is included.
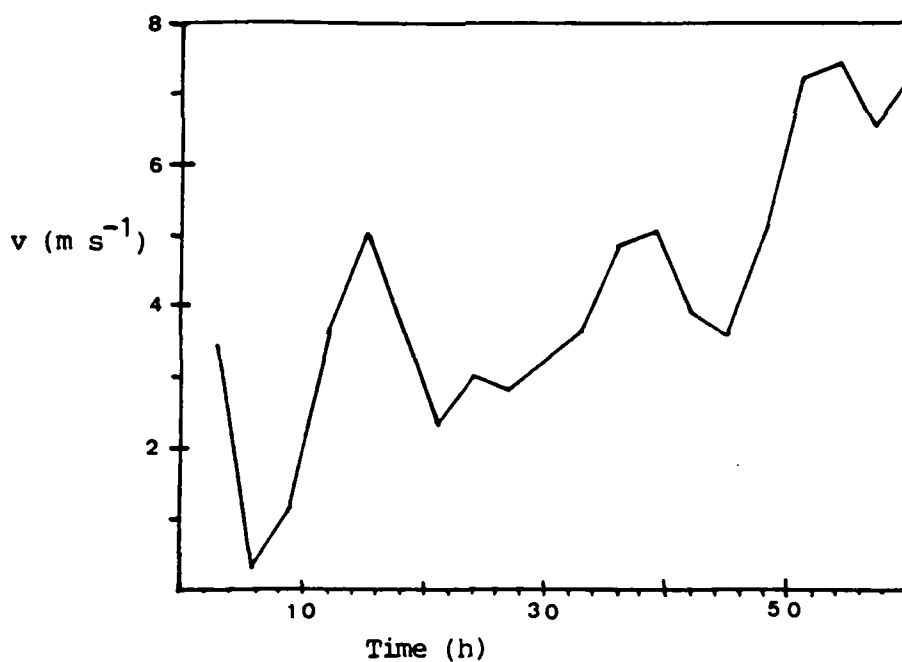


Figure 5.2. Amplitude of wave number 8 of v at σ = 0.9167 at 45°N plotted as a function of time for linear Experiment 1.

66
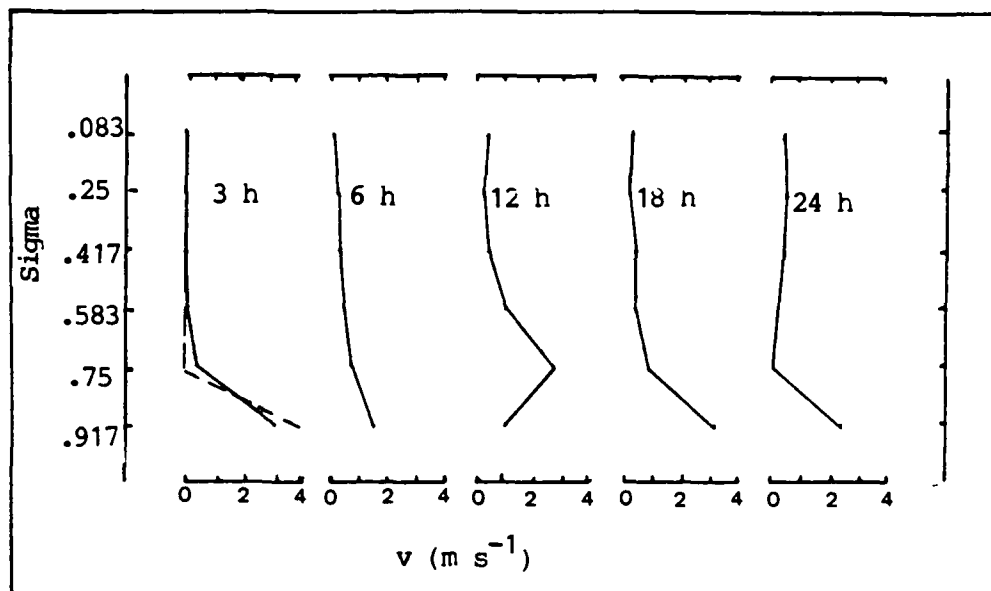
Figure 5.3.  Amplitude of wave number 8 of v at 45°N as a function of σ for linear Experiment 2.  Initial amplitude (dashed) versus σ is included.
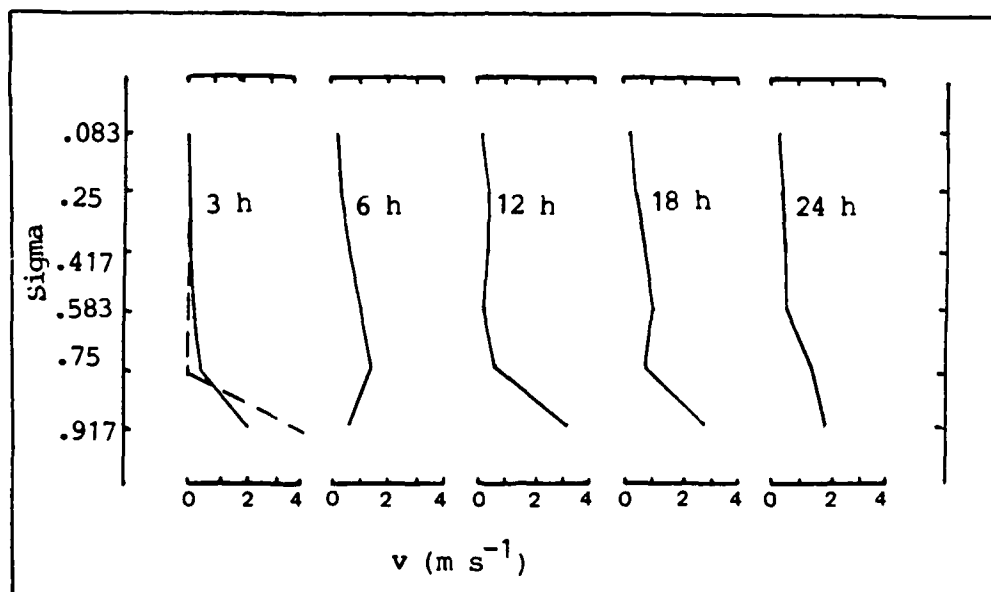


Figure 5.4.  Amplitude of wave number 8 of v at 45°N as a function of σ for linear Experiment 3.  Initial amplitude (dashed) versus σ is included.

described above were re-run using a 20-layer version of the NEPRF model to determine if more than six layers is required to resolve continuous-mode processes. In Figures 5.5a, b, and c, cross-sections at 45°N are shown for the 20-layer solutions superposed on the six-layer solutions at $t = 12$ h. In Figure 5.5a, the solutions are nearly coincident at all levels, which indicates that there are essentially no differences between the six-layer and 20-layer model runs. In Figures 5.5b and c, amplitude differences between the two solutions are only slightly greater (less than $1 \text{ m s}^{-1}$), and the phases are very close. No evidence of rapid growth was observed in any of the high resolution runs. Therefore, it is concluded that the six-layer resolution is sufficient for this research.

## B. DISTURBANCED FORCED BY THE TOPOGRAPHY IN A NONLINEAR MODEL

In the preceding section, the structure of the forced wave was explicitly specified in the initial conditions and a linearized model was used. The possibility exists that a more complicated structure is involved than given in the analytically-specified initial condition. In this section, cases are examined in which no attempt was made to control the initial structure of the forced orographic wave. Numerical experiments are conducted using the six-layer UCLA model, described in Chapter III, which includes nonlinear processes. The initial conditions consisted solely of the baroclinically unstable mean flow given by (4.3-4.5). In each experiment, the mean flow is forced over a long, narrow mountain (given by (4.8)) and was allowed to evolve for 90 hours.

Four experiments were conducted. In the first, the half-width of the jet stream, $\Upsilon$, was $8°$ and the mountain height, $z_{m_*}$, was 1.5 km. In the second experiment, $\Upsilon = 8°$ and $z_{m_*} = 3.0$ km were used. In the third
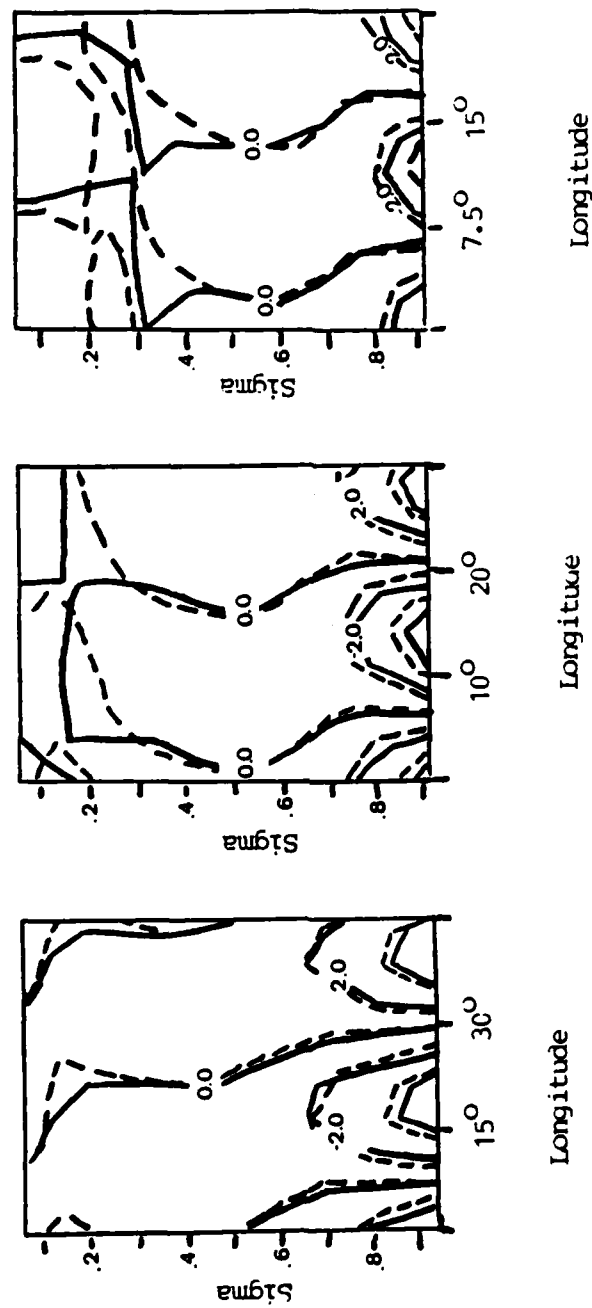
Figure 5.5. Vertical cross-sections of v along 45°N at 12 h from the six-layer (solid) and 20-layer (dashed) models for linear Experiments 1, 2, and 3 (a, b, and c, respectively). Contour interval is 2 m s⁻¹.

69

experiment, $\Upsilon = 16^0$ and $z_{m_\star} = 1.5$ km, and in the fourth, $\Upsilon = 16^0$ and $z_{m_\star} = 3.0$ km. Topography was raised from zero to its final height in 12 hours according to (4.9). Forcing of the mean flow by the mountain theoretically will excite a spectrum of discrete and continuous modes. As in the preceding section, for continuous modes to be significant, growth must occur earlier and be more rapid than that predicted for the discrete modes.

Results of the first experiment ($\Upsilon = 8^0$, $z_{m_\star} = 1.5$ km) are shown in Figure 5.6. When the mountain reaches its final height at $t = 12$ h, the forces ridge-trough pattern predicted by the Eady solution is observed. However, the high-pressure center is located over the lee slope of the mountain rather than over the ridge line as in the results of section II.B. The high-pressure ridge is maintained over the southern portion of the mountain throughout the model integration. However, in the region beneath the jet stream, the eastward elongation of the ridge indicates that a portion of the high is advected downstream. These results are in qualitative agreement with those of Huppert and Bryan (1975) who found that topographically forced circulations were advected downstream in strong mean currents and were bound to the topography in weak mean flows.

Examination of this sequence does not reveal any rapid continuous-mode growth. Between $t = 12$ and $t = 24$ h, when the continuous-mode growth should be evident, there is no significant cyclonic development. A weak trough appears at $t = 24$ h, but only slight amplification is observed during the following 24-30 hour period. This is certainly not the type of growth normally associated with lee cyclogenesis.

70
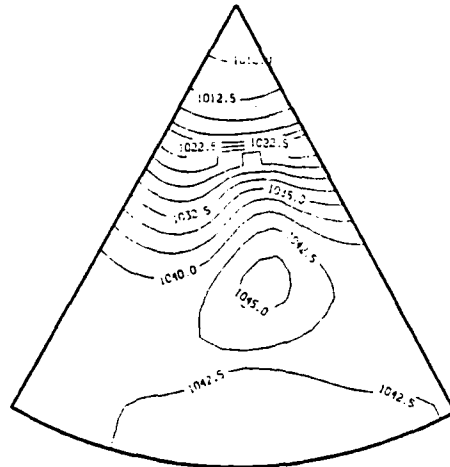
Figure 5.6a.  Sea-level pressure contours for nonlinear Experiment 1 at
              12 h.  Contour interval is 2.5 mb.  Domain is a 45° sector
              of the globe with cyclic continuity at the east and west
              boundaries.
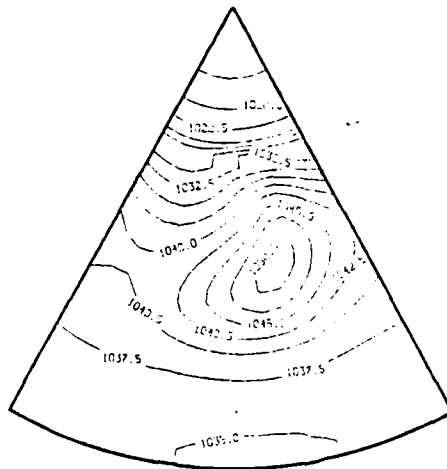


Figure 5.6b.  Sea-level pressure contours for nonlinear Experiment 1 at
              18 h.  Contour interval is 2.5 mb.  Domain is a 45° sector
              of the globe with cyclic continuity at the east and west
              boundaries.

71
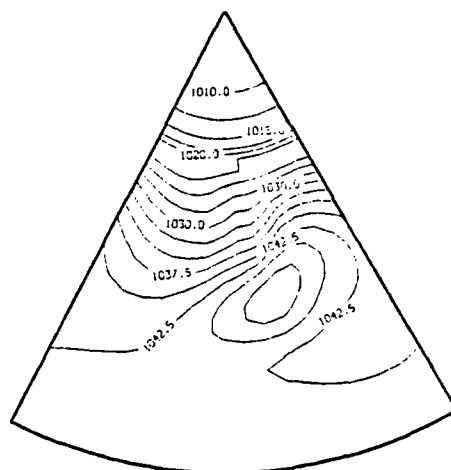
Figure 5.6c.  Sea-level pressure contours for nonlinear Experiment 1 at
24 h.  Contour interval is 2.5 mb.  Domain is a 45° sector
of the globe with cyclic continuity at the east and west
boundaries.
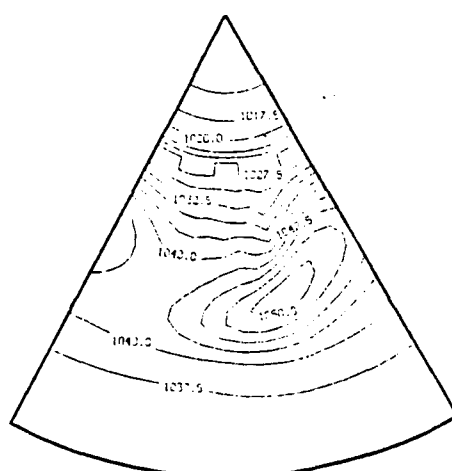


Figure 5.6d.  Sea-level pressure contours for nonlinear Experiment 1 at
30 h.  Contour interval is 2.5 mb.  Domain is a 45° sector
of the globe with cyclic continuity at the east and west
boundaries.

72
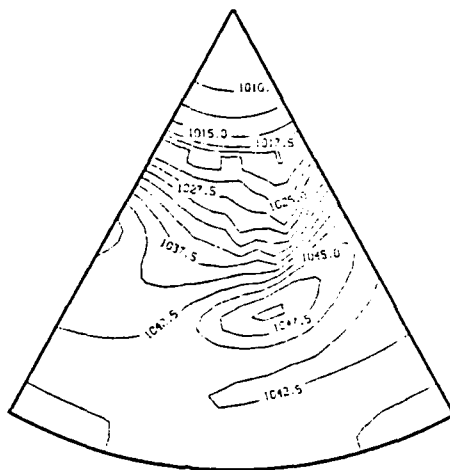
Figure 5.6e.   Sea-level pressure contours for nonlinear Experiment 1 at
               36 h.  Contour interval is 2.5 mb.  Domain is a 45° sector
               of the globe with cyclic continuity at the east and west
               boundaries.
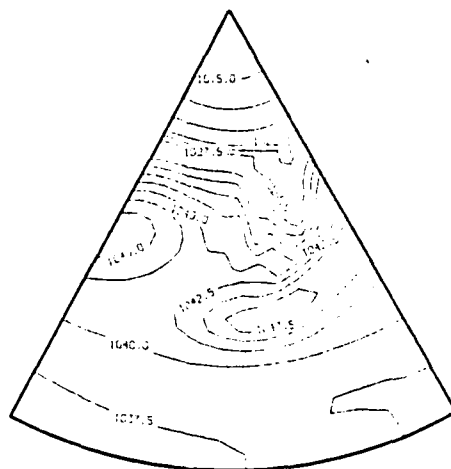


Figure 5.6f.   Sea-level pressure contours for nonlinear Experiment 1 at
               42 h.  Contour interval is 2.5 mb.  Domain is a 45° sector
               of the globe with cyclic continuity at the east and west
               boundaries.

73
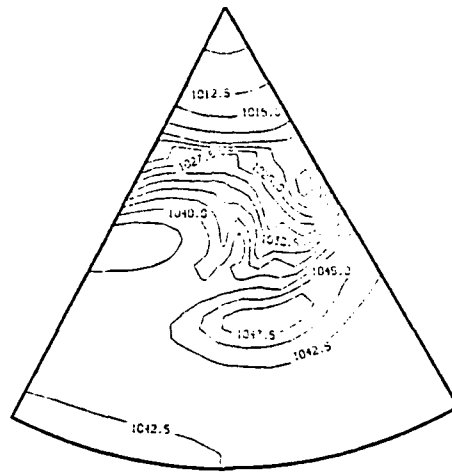
Figure 5.6g. Sea-level pressure contours for nonlinear Experiment 1 at 48 h. Contour interval is 2.5 mb. Domain is a 45° sector of the globe with cyclic continuity at the east and west boundaries.

In Figure 5.7, the amplitude of v for global wave number 8 at $\sigma = 0.9167$ is plotted versus time. In the first 12 hours, the amplitude grows rapidly in response to the "growing" mountain. Between $t = 12$ and $t = 24$ h, the model atmosphere adjusts to the presence of the mountain. A weak inertia-gravity wave (amplitude approximately 1-2 m s$^{-1}$) is observed. However, this wave does not grow and, in fact, appears to damp slightly with time. Amplification is not observed between $t = 12$ and $t = 50$ h. After $t = 50$ h, wave number 8 begins to amplify at an approximately exponential rate. This type of growth is predicted for disturbances in baroclinically unstable mean flows, but it is normally associated with the most unstable discrete mode, and not with continuous modes.

74
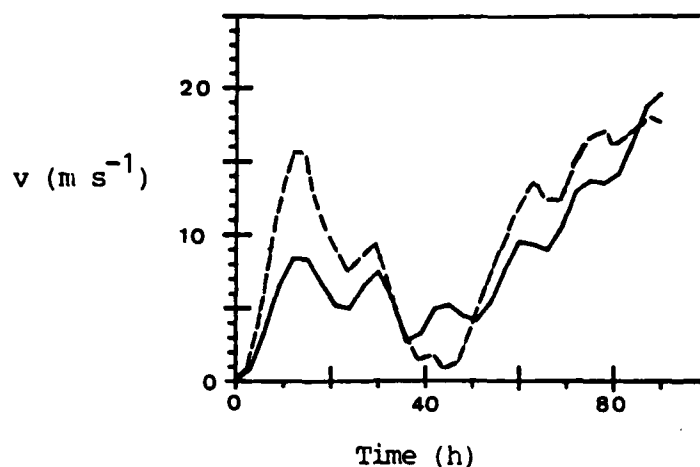
Figure 5.7. Amplitude of wave number 8 at $\sigma = 0.9167$ at 45°N versus time for nonlinear Experiments 1 (solid) and 2 (dashed).

Results of the second experiment ($\gamma = 8^0$, $z_{m_\star} = 3.0$ km) are similar as seen in Figure 5.7. As expected, the larger mountain forces a stronger deflection of the mean flow during the first 12 hours. Doubling of the mountain height approximately doubles the amplitude of the response. A more intense forced ridge-trough pattern is observed in the sea-level pressure contours (not shown), although no evidence of rapid growth is observed during the first 24 hours of the integration. Growth of the most unstable discrete mode is indicated here also, and it begins at about the same time ($t = 50$ h).

75

Results (Figure 5.8) of the third ($\gamma = 16^0$, $z_{m_*} = 1.5$ km) and fourth ($\gamma = 16^0$, $z_{m_*} = 3.0$ km) experiments are qualitatively similar. The response to the growing mountain during the first 12 hours is approximately the same ad in the $\gamma = 8^0$ runs, and doubling the mountain height approximately doubles the amplitude. A smaller gravity-wave oscillation (amplitude less than 1 m s$^{-1}$) is observed after t = 12 h, which indicates a better geostrophic adjustment. No initial growth which might indicate growing continuous modes is observed. In these two runs, baroclinic growth associated with the most unstable discrete mode is observed after t = 40 h (about 10 hours earlier than in the $\gamma = 8^0$ runs).
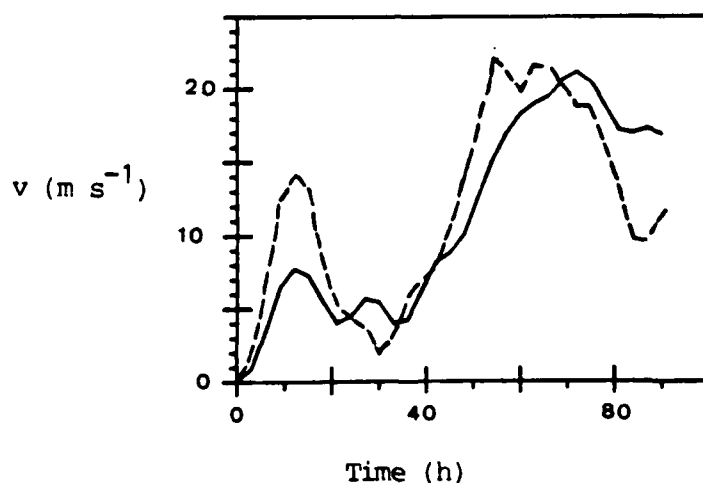


Figure 5.8. Amplitude of wave number 8 at $\sigma$ = 0.9167 at 45$^0$N versus time for nonlinear Experiments 3 (solid) and 4 (dashed).

76

The results of this chapter do not support the hypothesis that continuous-mode growth plays a significant role in lee cyclogenesis. Evidence of sustained, rapid growth is not observed during the first 24 h of any of the numerical experiments examined in this chapter. In the linear experiments, the vertically-trapped disturbance shows spurts of growth in the lower levels, but this growth is not sustained beyone approximately 3 h after onset. The overall character of these solutions appears to be oscillatory rather than amplifying.

In the nonlinear experiments, slight amplification of the forced surface-pressure trough is observed after 12 hours. However, since no evidence of rapid initial growth is observed in the v-component of the wind at $\sigma = 0.9167$, amplification must be confined to a region close to the earth's surface. The growth observed in these experiments is attributed to the most unstable discrete mode - and not to continuous modes. Consequently, if as Farrell suggests, growing continuous modes play a role in lee cyclogenesis, other justifiable initial conditions must be found.

## VI. BASIC NUMERICAL EXPERIMENTS

In this chapter, enhanced baroclinic instability and superposition
are considered as possible lee cyclogenesis mechanisms. Markine's (1975)
analysis of quasi-geostrophic flow past an infinitely long mountain
showed increased vertical wind shear on the lee side of the mountain,
which indicates enhanced baroclinicity. He has suggested that as a dis-
turbance moves into the lee of a mountain complex, it encounters a
signficantly destabilized mean flow and rapid cyclogenesis results.

Merkine's suggestion is investigated in this chapter using a series
of numerical experiments in which a free disturbance evolves in a baro-
clinically unstable flow. To isolate the effects of the mountain, runs
are made with and without topography. One of the two baroclinically un-
stable mean states that are considered also meets the necessary condition
for barotropic instability. Mountain height and length, as well as the
initial amplitude of the disturbance, are varied.

Results are examined for evidence of increased growth which could
indicate enhanced instability on the lee side of the mountain. As indi-
cated in Chapter II, observed lee-side growth could be explained by a
superposition of the growing wave on a steady, orographically forced lee-
side trough. Consequently, for the enhanced-instability mechanism to be
considered a significant contributer to lee cyclogenesis, it must be
demonstrated that disturbances moving over mountains develop more rapidly
than disturbances moving over flat terrain. That is, it must be shown

that this development significantly exceeds that caused by a combination of superposition and normal baroclinic growth.

## A. NUMERICAL EXPERIMENTS

Numerical experiments are carried out using the version of the UCLA model described in Chapter III. The initial mean state consists of a baroclinically unstable, westerly current balanced analytically for a flat lower boundary (that is, no topography). The basic current, given by (4.1-4.5), possesses both horizontal and vertical shear and reaches a maximum speed of 45 m s$^{-1}$ in the top layer of the model at 45°N. A mean westerly surface current with a similar horizontal profile as the upper level flow is included. The maximum surface wind is 5 m s$^{-1}$ at 45°N. The mountain consists of a long, smooth barrier (approximately 47° latitude by 24° longitude) oriented north-south as described by (4.8).

### 1. Experimental Techniques

Each experiment consists of three runs: Control, Interaction, and Non-interaction. In the Control run, a weak disturbance, given initially by (4.6), is allowed to evolve into a mature cyclone with no topography included. The time-dependent solution for this run may be represented as:

$$\Psi_C(t) = \bar{\Psi}_F + \Psi'_C (t) \qquad , \qquad (6.1)$$

where $\bar{\Psi}_F$ is a zonally symmetric, time-independent state in gradient balance over flat topography. Here, $\Psi'_C$ is the instantaneous deviation of the solution from the mean state. Because the UCLA model is fully

nonlinear, there are no implied constraints on the magnitude or mean value of $\Psi_c'(t)$.

In the Interaction run, a growing baroclinic wave evolves as it passes over the mountain. The initial conditions for the integration are constructed by combining $\Psi_c'$ (taken from the Control run at some arbritrary time $t_0$ using (6.1) with an orographically forced, mountain mean state such that

$$\Psi(t_0) = \bar{\Psi}_M + \Psi_c'(t_0) \qquad (6.2)$$

$\bar{\Psi}_M$ is a zonally asymmetric, time-independent mean state representing flow in the presence of the mountain. These conditions are integrated forward in time with full-height topography until the disturbance passes over the mountain. The resulting Interaction solution may be formally separated into two parts analogously to (6.1):

$$\Psi_I(t) = \bar{\Psi}_M + \Psi_I'(t) \qquad , \qquad (6.3)$$

To isolate the degree of interaction between the growing wave and the mountain-induced distortions in the mean state, a Non-interaction solution $\Psi_N(t)$ is constructed without model integration by combining $\Psi_c'(t)$, taken from the Control run at each desired output time, with $\bar{\Psi}_M$ such that

$$\Psi_N(t) = \bar{\Psi}_M + \Psi_c'(t) \qquad . \qquad (6.4)$$

In this way, the Non-interaction solution parallels the development in Chapter II in which the time-dependent Eady solution was superposed on the steady, orographically forced solution to describe the passage of a wave over the mountain.

The observed growth is affected by the superposition of the disturbance on the forced lee-side trough in both the Interaction and Non-interaction runs. However, the growth of the disturbance in the Interaction run is also affected by the stability of the orographically forced mean flow, whereas the growth of the Non-interaction disturbance is affected by the stability of a zonally uniform mean flow. Therefore, comparison of these two runs will reveal differences in growth caused by the orographically forced distortions to the mean flow. If mean flow destabilization is a significant factor in lee cyclogenesis, large increases in growth should be observed in the Interaction runs.

## 2. Derivation of the Mountain Mean State

The key to the experimental procedure described in the preceding section is the steadiness of the mountain mean state. Because the mean flow is baroclinically unstable and the mountain is a continous source of disturbances, normal-mode growth is anticipated. Therefore, a strictly time-independent mountain mean state is not achieveable. However, a "locally" steady state can be derived by limiting the analysis to that part of the solution in which the normal-mode amplitudes are negligibly small.

In this study, the locally steady, mountain mean state is derived from a model run in which the Control mean flow, $\Psi_F$, is integrated in the presence of the mountain. The mountain in this case is raised from zero

81

to its full height in 12 hours. The solution is then time-averaged over 12 hours (using fields from $t = 18$ to $t = 30$ h) to filter out inertia-gravity waves, and this time-averaged solution is defined as the mountain mean state, $\bar{\Psi}_M$.

Test integration of $\bar{\Psi}_M$ revealed the presence of a weak transient solution and some amplification of the forced modes at $t = 24$ h. These effects are present in the Interaction run which includes $\bar{\Psi}_M$ as part of the initial conditions for a model integration. They are included in the Non-interaction run by integrating $\bar{\Psi}_M$ separately in the presence of the mountain and using this time-dependent $\bar{\Psi}_M(t)$ in (6.4). Formally, then, the Non-interaction solution is written

$$\Psi_N(t) = \bar{\Psi}_M(t) + \Psi'_C(t) \qquad . \qquad (6.5)$$

## 3. Description of Experiments

The numerical experiments conducted in this portion of the study are listed in Table 6.1. In each, an Interaction run and a Non-interaction run are generated. Two basic states are considered: one in which the jetstream halfwidth, $\gamma$ (in (4.1) - (4.5)), is $16^\circ$ latitude and one in which $\gamma = 8^\circ$. Vertical cross-sections of the mean wind for these two basic states are shown in Figure 4.1. As indicated earlier, the $8^\circ$ jet more closely resembles the upper level flow observed during cyclogenesis (see, for example, Palmen and Newton (1969)). However, the $8^\circ$ jet also meets the necessary condition for barotropic instability in regions immediately north and south of the jet. Therefore, a $16^\circ$ jet which does not meet this condition is included to isolate the baroclinic effects.

82

Table 6.1. List of Experiments

| | | |
|---|---|---|
| Control A: | 16° Jet | No Topography |
| Control B: | 8° Jet | No Topography |
| I | 16° Jet | 47°x24°x1.5 km Mountain |
| II | 16° Jet | 47°x24°x3.0 km Mountain |
| III | 8° Jet | 47°x24°x1.5 km Mountain |
| IV | 8° Jet | 47°x24°x3.0 km Mountain |
| Va | 16° Jet | 25°x24°x3.0 km Mountain |
| Vb | 16° Jet | 57°x24°x3.0 km Mountain |

In these experiments, the initial amplitude of the disturbance, the mountain height, and the mountain width are varied. The initial disturbance amplitude ranges from very weak to approximately finite-amplitude, and is prescribed by setting $t_0$, the time at which the perturbation fields are taken from the Control fun, to the appropriate value. Results of Trevisan (1976) suggest that lee cyclogenesis is triggered only when the disturbance has sufficient amplitude before encountering the mountain. If this is so, the results of these experiments should identify a minimum amplitude.

Mountain height is varied between 1.5 km and 3.0 km. The analysis of Chung et al. (1976) indicates that mountain height plays a role in the generation of lee cyclones. In addition, the results of Williams et al. (1981) suggest that the fundamental character of the mean flow distortion differs with mountain height - with air parcels tending to flow over smaller mountains and around larger mountains. The 1.5 km mountain range is representative of smaller mountains such as the

Appalachians, whereas the 3.0 km mountain range roughly resembles the Rockies. Because it represents a larger obstacle, the higher mountain is expected to have a greater impact on the development of the wave.

The sensitivity of disturbance growth to mountain length is investigated by using three mountain lengths: 47°, 25°, and 57°. The 47° mountain length was used in the majority of experiments and should be assumed unless otherwise specified.

## B. RESULTS

### 1. Control Runs

Control runs without topography were generated to: 1) measure growth in the absence of topography (defined here as "normal" baroclinic growth); 2) identify the portion of the solution dominated by linear dynamics; and 3) create the $\Psi_c'(t)$ fields required for initializing the Interaction run and defining the perturbation in the Non-interaction run. A control run for each basic state ($\gamma = 16°$ and $\gamma = 8°$) was required.

Results of Control Run A (16° jet) are shown in Figure 6.1. An initially weak disturbance grows into a closed circulation by approximately $t = 60$ h (not shown) and by $t = 96$ h, a mature cyclone is observed. A log-linear plot of disturbance amplitude at wave number 8 versus time is given in Figure 6.2. The exponential growth predicted by linear theory is observed from approximately $t = 30$ to $t = 75$ h; the doubling time is approximately 21 hours, and is in agreement with the rough estimate of 24 hours for synoptic-scale baroclinic waves given by Haltiner and Williams (1980). Growth is not observed at other wave numbers until after $t = 60$ h, which indicates that linear processes dominate through this period.

84
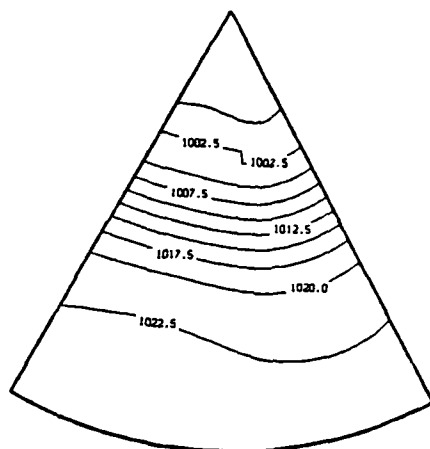
Figure 6.1a. Sea-level pressure contours for control run A at 0 h.
Contour interval is 2.5 mb.
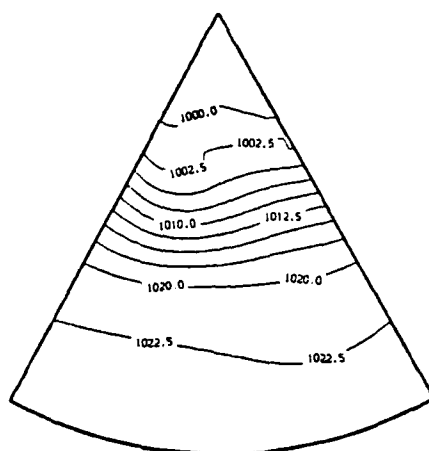


Figure 6.1b. Sea-level pressure contours for control run A at 24 h.
Contour interval is 2.5 mb.
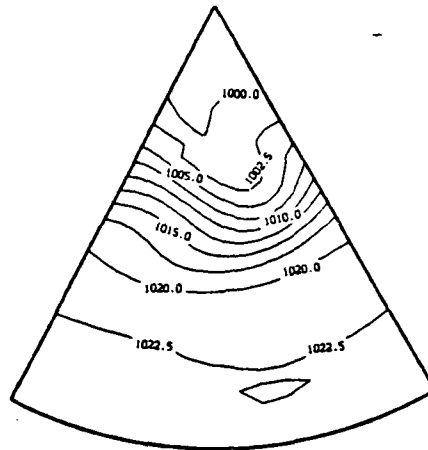
Figure 6.1c.   Sea-level pressure contours for control run A at 48 h.
Contour interval is 2.5 mb.
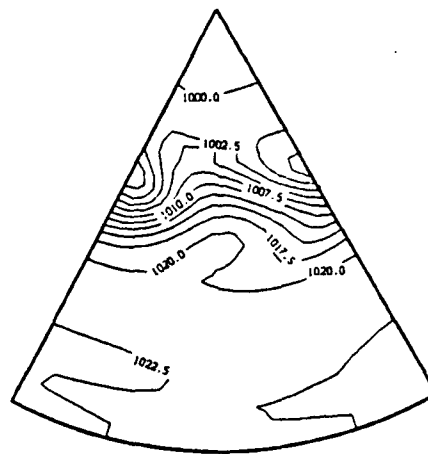


Figure 6.1d.   Sea-level pressure contours for control run A at 72 h
Contour interval is 2.5 mb.
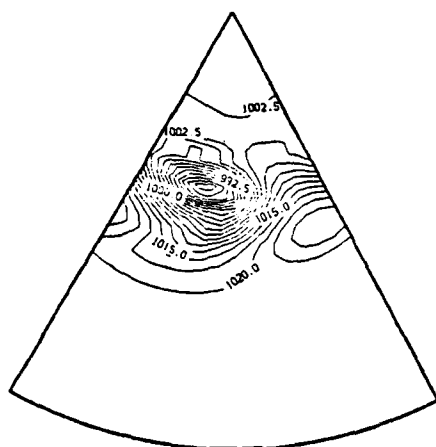
Figure 6.1e.  Sea-level pressure contours for control run A at 96 h.
Contour interval is 2.5 mb.
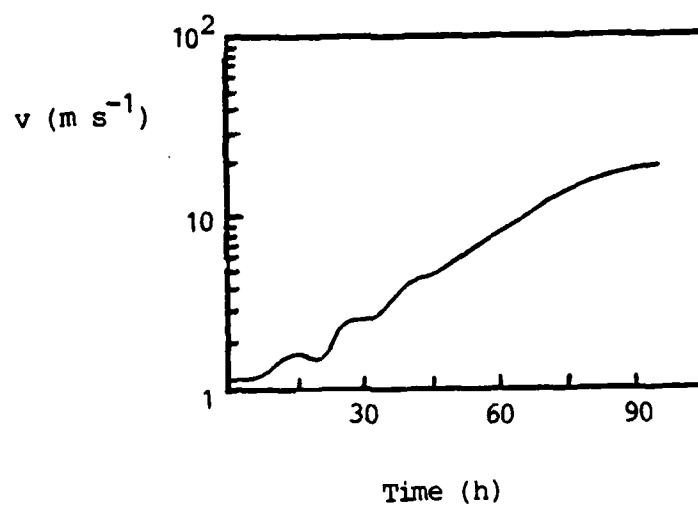


Figure 6.2.  Amplitude of wave number 8 of v at σ = 0.9167 versus time at
45°N for control run A.

87

Results of Control Run B (the 8° jet) are similar. Growth in this case is slightly slower with a disturbance doubling time of 27 h, as is indicated in Figure 6.3. Even though both jets have the same maximum speed, the broader 16° jet leads to a larger growth rate. This is apparently because the 16° jet has more available potential energy (because of the larger temperature variance). Also, the stronger barotropic effects in the 8° jet may reduce the growth rate as has been shown by Grotjahn (1979).
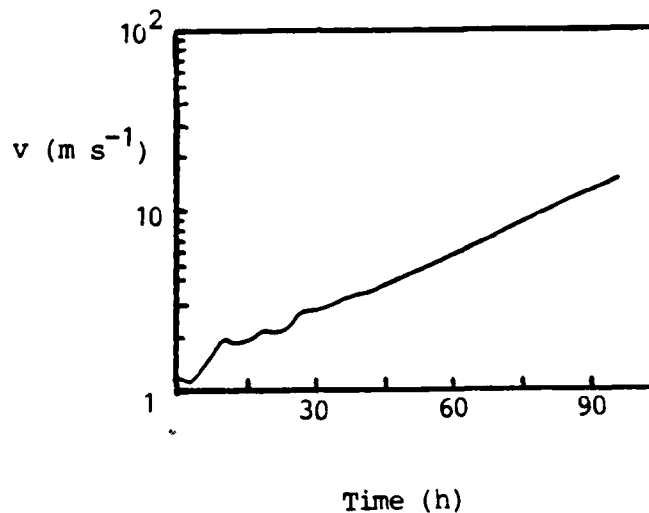


Figure 6.3.   Amplitude of wave number 8 of v at $\sigma$ = 0.9167 versus time at 45°N for control run B.

## 2. Experiment I: 16º Jet, 47ºx24ºx1.5 km Mountain

In this experiment, the effect of the 1.5 km mountain on distur-
bance growth in the presence of the 16º jet is considered. Four cases
are examined in which the initial wave amplitude is successively in-
creased. In Case 1, the initial perturbation fields are taken from the
Control at $t = 24$ h. In Cases 2, 3, and 4, the initial fields are taken
from 36, 48, and 60 h, respectively. In each of these cases, the distur-
bance is initially positioned upstream of the mountain.

In Figure 6.4, sea-level pressure contours are shown at 12-hourly
intervals for Case 1. The disturbance crosses the mountain, and a closed
circulation, indicative of cyclogenesis, develops on the lee side. This
growth exceeds that observed in the corresponding control run, where a
closed circulation is not observed until $t = 60$ h (at $t = t_0 + 36$ h,
relative to the time units of Case 1). As noted previously, the increas-
ed growth is at least partially due to the superposition of the wave on
the forced lee-side trough. To account for this afect, the non-inter-
action run is introduced in Figure 6.4d. The closed circulation observed
at $t = t_0 + 24$ h is also observed here. The similarity of the two solu-
tions suggests that the effect of the mountain on the stability of the
mean flow is not critical to the occurrence of lee cyclogenesis in this
case.
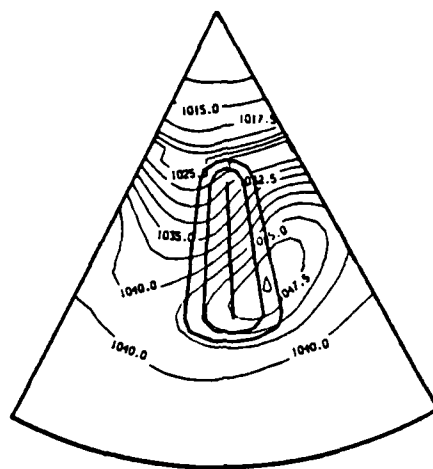
Figure 6.4a.  Sea-level pressure contours for the Interaction and Non-
interaction solutions of Experiment I, Case 1.  Interaction
solutions are given at $t_0$.    Contour interval is 2.5 mb.
Bold contours at center of figure represent mountain.
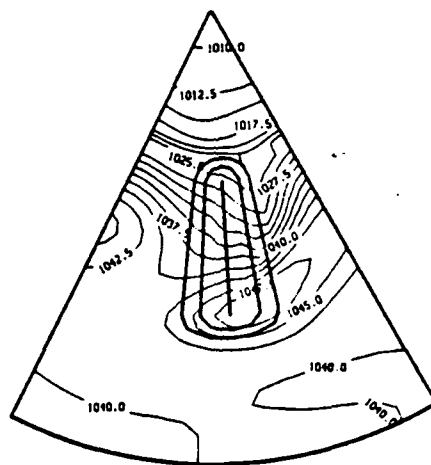


Figure 6.4b.  Sea-level pressure contours for the Interaction and Non-
interaction solutions of Experiment I,. Case 1.  Interaction
solutions are given at $t_0+12$ h.    Contour interval is
2.5 mb.  Bold contours at center of figure represent
mountain.

90
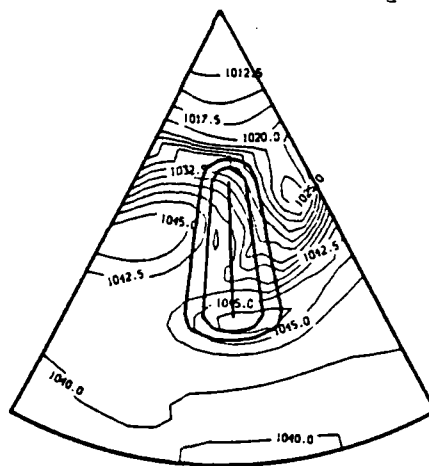
Figure 6.4c.  Sea-level pressure contours for the Interaction and Non-interaction solutions of Experiment I, Case 1.  Interaction solutions are given at $t_0$+24 h.    Contour interval is 2.5 mb.  Bold contours at center of figure represent mountain.
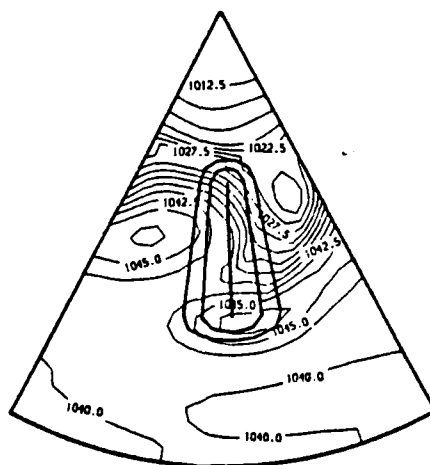


Figure 6.4d.  Sea-level pressure contours for the Interaction and Non-interaction solutions of Experiment I, Case 1.  Non-Interaction solution is given at $t_0$+24 h.  Contour interval is 2.5 mb.  Bold contours at center of figure represent mountain.

91

The solutions for Case 4 are shown at $t_0$+24 h in Figures 6.5a (Interaction run) and 6.5b (Non-interaction run). The Interaction cyclone appears more intense than the Non-interaction cyclone. The central, closed pressure contour of the Interaction cyclone is 5 mb lower than in the corresponding Non-interaction cyclone. In addition, the pressure gradient east of the cyclone center appears stronger in the Interaction run. However, as in Case 1, a lee cyclone is observed in both runs. Similar results were observed in Cases 2 and 3 (not shown). Although some destabilization of the mean flow may be indicated by the more intense Interaction solutions, it does not appear to be critical to the formation of the surface cyclone. In addition, in contrast to the results of Trevisan (1976), the amplitude of the initial disturbance does not appear to be a factor in the occurrence of lee cyclogenesis.

To isolate the effect of the mountain on disturbance growth, the mountain mean state, $\bar{\Psi}_M(t)$, is subtracted from each of these runs to allow a direct comparison of $\Psi_I'(t)$ and $\Psi_N'(t)$. Recall that the latter is by definition simply the perturbation field from the control case, $\Psi_C'(t)$. A harmonic analysis (Figure 6.6) of the v field at $\sigma = 0.9167$ (p $\doteq$ 930 mb) along 45°N was completed for each run. The curves represent amplitude, A, which is computed according to

$$A = \left[ \sum_{n=0}^{8} a_n^2 \right]^{0.5} \quad , \quad (6.6)$$
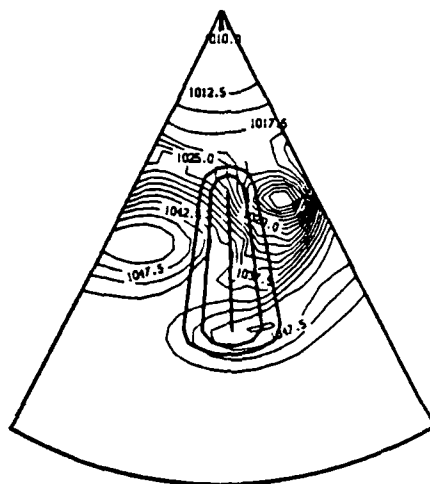
Figure 6.5a. Sea-level pressure contours at $t_0$+24 h for Interaction solutions of Experiment I, Case 4. Contour interval is 2.5 mb. Bold contours at center of figure represent mountain.
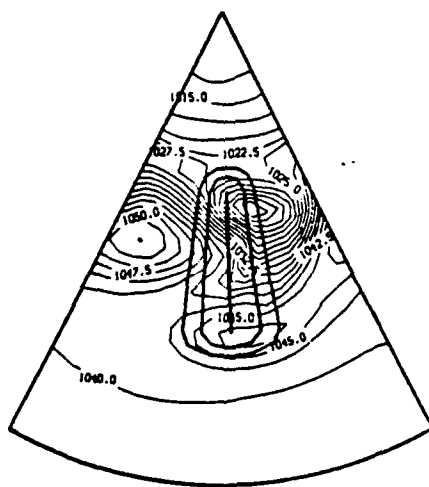


Figure 6.5b. Sea-level pressure contours at $t_0$+24 h for Non-interaction solutions of Experiment I, Case 4. Contour interval is 2.5 mb. Bold contours at center of figure represent mountain.

where $a_n$ is the amplitude of the nth harmonic. In the first three cases, the Interaction and Non-interaction curves are very close, which indicates that the mountain has little effect on the growth rate of the disturbance. In Case 4, the growth is similar through $t_0 + 15$ h, after which the Interaction disturbance appears to grow more slowly.
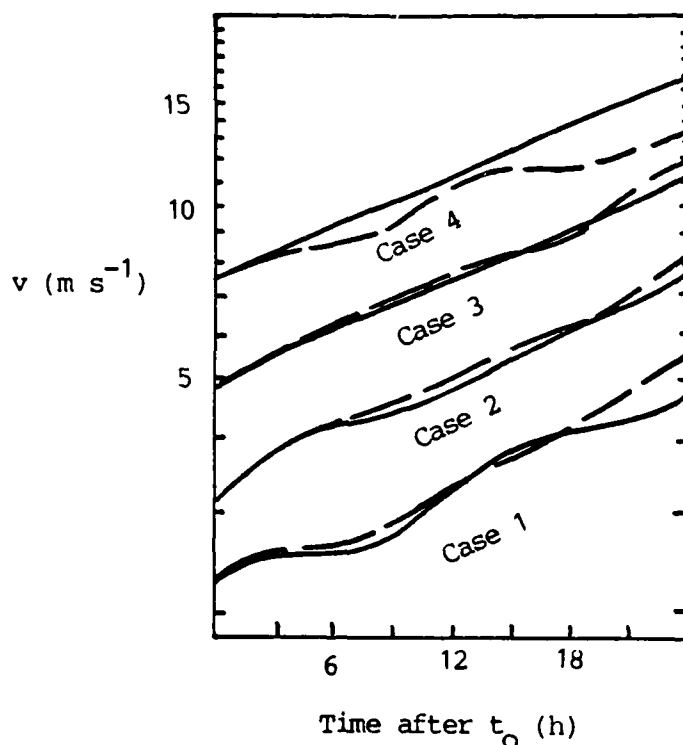


Figure 6.6. Amplitude of wave number 8 of v at $\sigma = 0.9167$ at 45°N for Experiment I, Cases 1, 2, 3, and 4. Interaction (dashed) and Non-interaction (solid) solutions are shown.

Figure 6.7, the minimum value of $p_s'$, the deviation from mean-state surface pressure, along 45°N is plotted versus time for each of the runs. As the wave moves up the mountain from $t = 0$ to 12 h, the Interaction disturbance grows more slowly than the Non-interaction disturbance. In fact, the disturbance even weakens between $t - t_0 + 6$ and

94
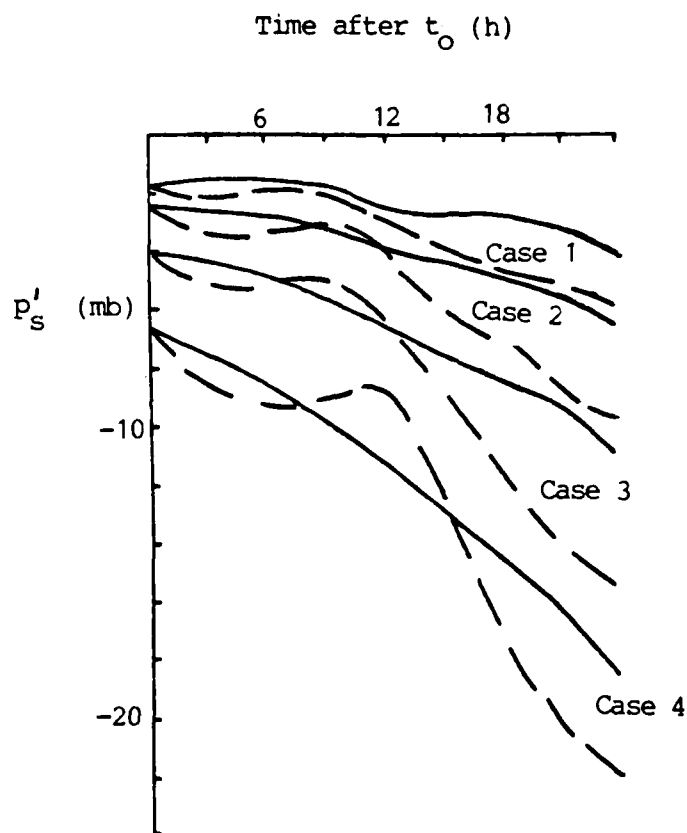
Figure 6.7. Minimum $p_s'$ (where $p_s = p_s - \bar{p}_s$) at 45°N versus time
for Experiment I, Cases 1, 2, 3, and 4. Interaction
(dashed) and Non-interaction (solid) solutions are shown.

$t_0$ + 12 h. As the disturbance moves down the lee side of the mountain, more rapid growth is observed in the Interaction run. This latter result suggests that enhanced instability may exist on the lee side of the mountain. However, the net effect on the disturbance is small because of the period of decreased growth (or weakening) which occurs when the disturbance is on the windward slope. The minimum value of $p_s'$ along 45°N for each case is listed in Table 6.2. The Interaction values are lower than the Non-interaction values. However, the maximum difference between

END

FILMED

DTIC
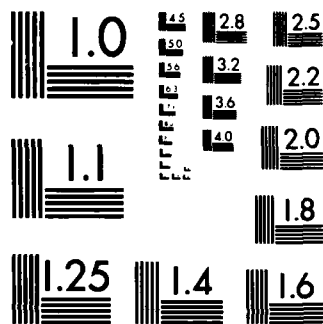
MICROCOPY RESOLUTION TEST CHART
NATIONAL BUREAU OF STANDARDS-1963-A

## Table 6.2. Experiment I. Cases 1-4.
### Disturbance Characteristics

Entries in the column labeled "min $p_S'$" represent the lowest values of the deviation from mean-state surface pressure along 45°N at $t = t_0 + 24$ h.

Entries in the phase-speed column represent the average phase speed of wave number 8 of $v$ at $\sigma = 0.9167$ along 45°N over the 24-hour period of the model integration.

$V_M$ represents the orographically-forced, meridional wind component in the Hoskins transformation estimated from the numerical results at $t = t_0 + 24$ h.

Phase differences, expressed in units of length, of wave number 8 of $p_S'$ at 45° are given in the two columns at the right. In the subcolumn labeled "SG", entries represent the phase shift predicted by the semi-geostrophic solution (2.46) using entries from the $V_M$ column. In the sub-column labeled "EXP", entries represent the differences in east-west position between the Interaction and Non-interaction solutions.

| Case | Min $p_S'$ (mb) | | Phase Speed (m s$^{-1}$) | | $V_M$ (m s$^{-1}$) | Phase Differences (km) | |
|------|------|------|------|------|------|------|------|
|      | I*   | N    | I    | N    |      | SG   | Exp  |
| 1    | -6.4  | -4.2  | 17.8 | 16.1 | -13.2 | 256 | 135 |
| 2    | -9.9  | -6.8  | 17.9 | 15.4 | -14.2 | 276 | 215 |
| 3    | -15.6 | -11.3 | 18.3 | 15.4 | -17.0 | 330 | 235 |
| 4    | -22.7 | -18.7 | 20.0 | 15.6 | -17.7 | 344 | 488 |

* I - Interaction; N = Non-interaction

the Interaction and Non-interaction values is less than 4 mb and does not appear to be critical to the formation of a closed surface pressure contour.

Comparison of the phases of the two sets of solutions reveals that the Non-interaction cyclones lag the corresponding Interaction cyclones. This effect is seen more clearly by comparing the phases of the two solutions. In Figure 6.8, an acceleration of the Interaction disturbance is apparent even at $t = t_0 + 6$ h, and by $t = t_0 + 24$ h, the phase difference between the Interaction and Non-interaction solutions has increased significantly. A similar phase difference is observed at $t = t_0 + 24$ h in Cases 2, 3, and 4 as shown in Figure 6.9.

This result is predicted by the semi-geostrophic solution considered in Chapter II. It was shown there that the disturbance is accelerated as it passes over the mountain. Here, the Non-interaction run represents the linear solution (in the transform space of Chapter II) and the Interaction run corresponds to the semi-geostrophic solution (in the physical space). The phase difference between the two solutions is a result of the acceleration of the disturbance as it passes over the mountain. A rough estimate of this difference may be obtained using the transformation rule (2.46). The phase differences predicted by the semi-geostrophic solution and those observed (between the Interaction and Non-interaction solutions) in the four cases of Experiment I are given in Table 6.2. The value of $V_M$ required to calculate the semi-geostrophic value is estimated by using the maximum value of v at $\sigma = 0.9167$ observed immediately downstream of the mountain. Qualitative agreement exists between the observed and theoretical values.
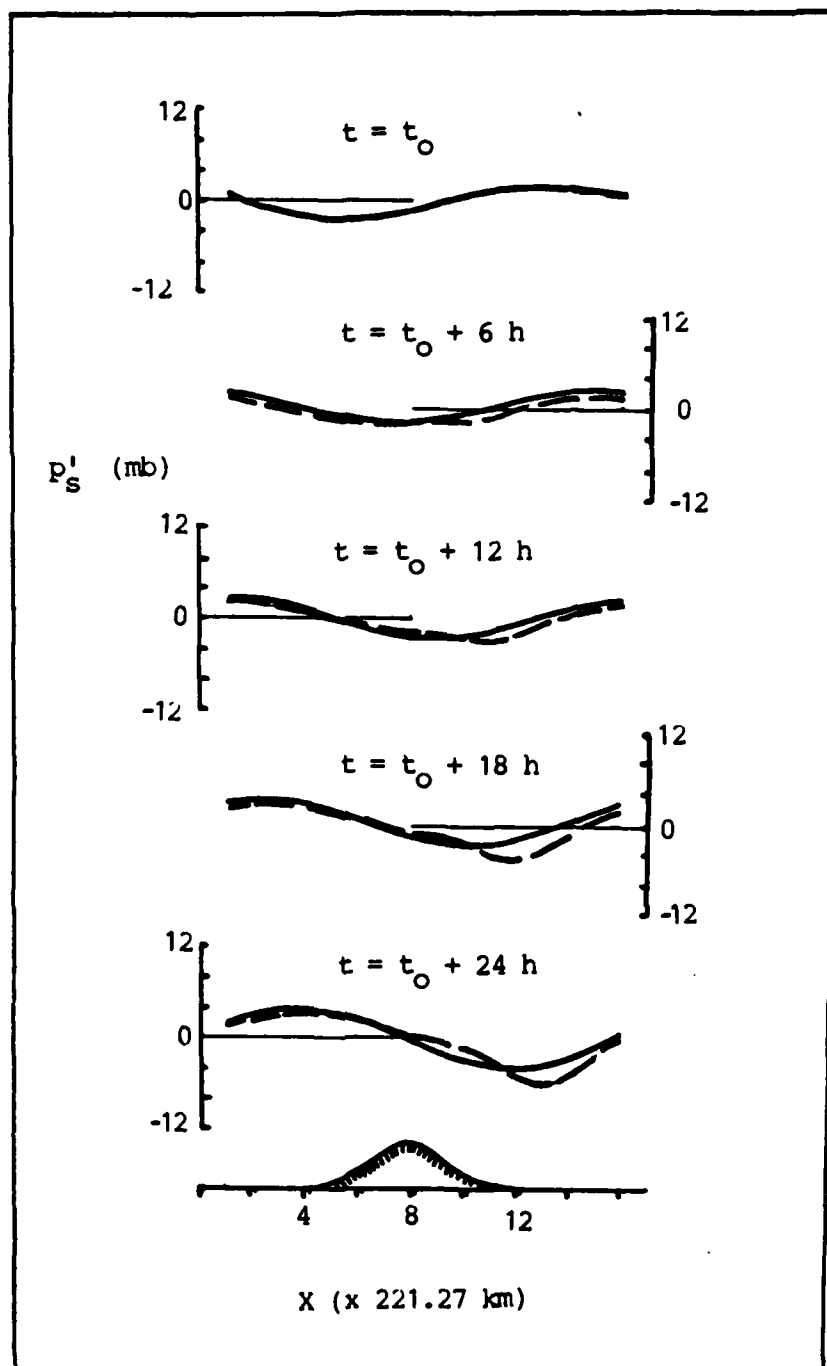
Figure 6.8   $p_s'$ (where $p_s = p_S - \bar{p}_S$) versus X for Experiment I, Case 1 at
45°N at 6 h intervals from $t_0$ to $t_0$+24 H.   Dashed curves re-
present  Interaction solutions; solid curves represent Non-
interaction solutions.  East-west profile of mountain is
shown at bottom.

98
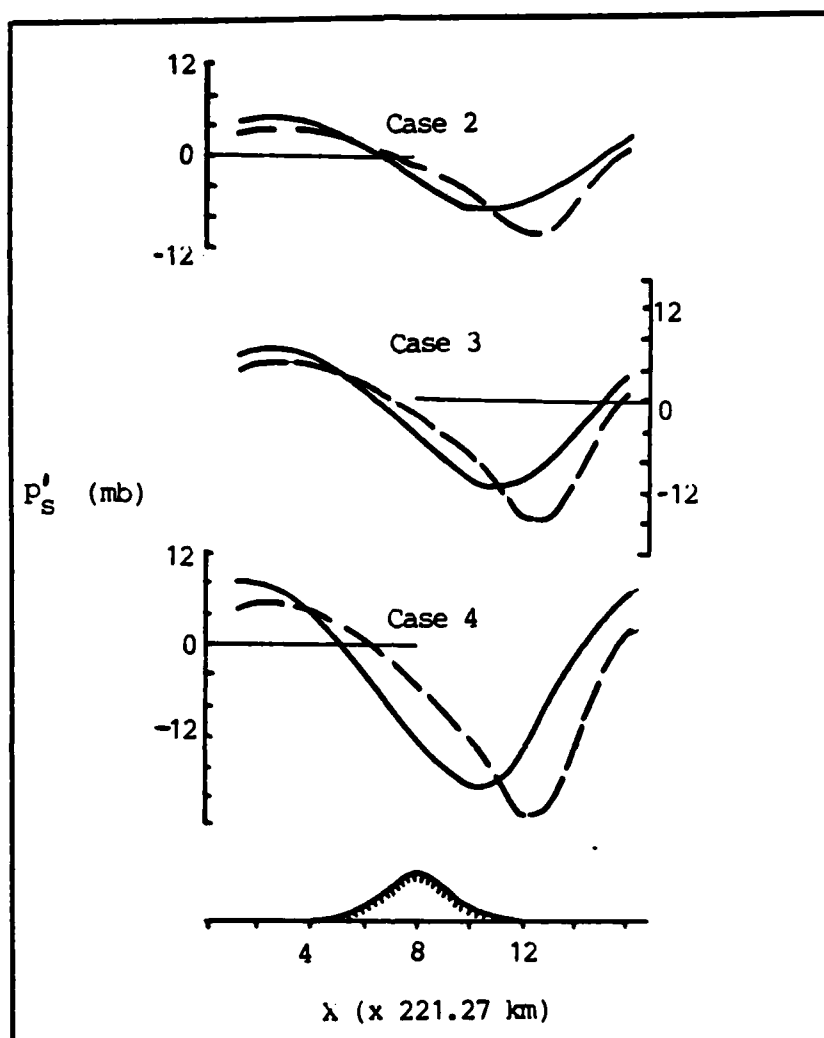
Figure 6.9. $p_s'$ (where $p_s = p_s - \bar{p}_s$) versus X for Experiment I, Cases 2, 3, and 4 at $45^\circ$N at 6 h intervals from $t_0$ to $t_0+24$ H. Dashed curves represent Interaction solutions; solid curves represent Non-interaction solutions. East-west profile of mountain is shown at bottom.

99

Table 6.3. Experiment II. Cases 1-4.
Disturbance Characteristics

| Case | Min $p'_s$ (mb) | | Phase Speed (m s$^{-1}$) | | $V_M$ (m s$^{-1}$) | Phase Differences (km) | |
|------|------|------|------|------|------|------|------|
| | I* | N | I | N | | SG | Exp |
| 1 | -5.5 | -4.2 | 18.1 | 16.1 | -19.6 | 381 | 175 |
| 2 | -9.1 | -6.8 | 18.6 | 15.4 | -23.6 | 459 | 280 |
| 3 | -14.5 | -11.3 | 18.9 | 15.4 | -29.6 | 575 | 290 |
| 4 | -22.6 | -18.7 | 21.7 | 15.6 | -33.9 | 659 | 510 |

* I - Interaction; N = Non-interaction

### 3. Experiment II: 16° Jet, 47°x24°x3.0 km Mountain

In this experiment, the effect of mountain height on disturbance growth is considered. The four cases of experiment I corresponding to initial disturbances from 24, 36, 48, and 60 h are repeated using a 3.0 km mountain. Results of Case 1 are shown in Figure 6.10. As in experiment I, the disturbance moves over the mountain and cyclogenesis is observed as the disturbance moves away from the lee slope. The higher values observed in the surface pressure ridges in this and other figures are due to a lack of downstream variation in the baroclinic stability of the mean flow and the exclusion of friction from the numerical model. In general, these factors will result in more intense cyclones and anticyclones in the numerical simulations, but should not change the fundamental conclusions based on the comparison of the Interaction and Non-interaction simulations. The maximum amplitude and phase speed of the disturbance do not appear to be affected significantly by the higher mountain. The minimum value of $p'_s$ in Case 1 is -5.5 mb (Table 6.3) which

Figure 6.10a. Sea-level pressure contours at $t_0+24$ h for Interaction solutions of Experiment II, Case 1. Contour interval is 2.5 mb. Bold contours at center of figure represent mountain.



Figure 6.10b. Sea-level pressure contours at $t_0+24$ h for Non-interaction solutions of Experiment II, Case 1. Contour interval is 2.5 mb. Bold contours at center of figure represent mountain.

is close to the value of -6.4 mb observed in Case 1 of experiment I; the phase speeds are within $0.3 \text{ m s}^{-1}$. In addition, the difference in development between the Interaction cyclone (Figure 6.10a) and the Non-interaction cyclone (Figure 10b) in Case 1 is less than 2 mb as in experiment I.

The magnitude of the orographically-forced meridional wind component, $V_M$, (Table 6.3) in Case 1 is more than $6 \text{ m s}^{-1}$ higher than the corresponding value of experiment I. This increase which is also observed in Cases 2 through 4 is due to the stronger deflection of the flow caused by a higher mountain, and is predicted by the solution (2.13).

Another significant difference from experiment I is observed in the vicinity of the mountain top at $t = t_0 + 24$ h (Figure 6.10a) in the form of a second cyclone. This feature first appears as a weak trough on the upwind slope of the mountain approximately 12 hours into the integration and it intensifies as it moves up the mountain slope in a north-easterly direction. This same feature is observed in the Non-interaction solution (Figure 6.10b), but its amplitude is much weaker. This secondary cyclone which was also observed by Walker (1982) appears to be related to mountain height and is discussed further in experiment Vb.

The results of Cases 2 through 4 (not shown) are similar. In each case, the Interaction lee cyclone appears to be more intense than the corresponding Non-interaction cyclone. In Case 3, where the difference in intensity is most noticeable, the central closed isobar of the Interaction cyclone is 7.5 mb lower than in the corresponding Non-interaction cyclone. However, when the mean state is subtracted from the solutions, the difference is reduced to 3.2 mb (Table 6.3). This

102

indicates that superposition is partially responsible for the observed difference. In the other three cases, the minimum $p_s'$ for the Non-interaction run is within 4 mb of the value for the corresponding Interaction run. These results are in agreement with those of Experiment I, and again indicate that superposition is the dominant effect.

In Figure 6.11, the amplitude of $v^*$ at $\sigma = 0.9167$ along 45°N is plotted as a function of time for each of the four cases. From $t = t_0$ to $t + 18$ H, as the disturbance moves over the mountain and down the lee side, the slopes of the Interaction and Non-interaction curves are very close, which indicates, again, that the mountain has little effect on the growth rate. From $t = t_0 + 18$ h to $t_0 + 24$ h, after the disturbance has begun to move away from the mountain, some increase is observed in the growth rates of the Interaction disturbances. However, by this time, a closed circulation, indicative of cyclogenesis, has already formed and the additional growth does not appear to be critical to the formation of a closed surface-pressure contour.

The phase acceleration noted in Experiment I is also observed here. The semi-geostrophic and experimental phase differences are given in Table 6.3. In these cases, the semi-geostrophic solution over-estimates the acceleration experienced by the Interaction disturbance. This is because of the large magnitude of v observed in the lee of the mountain. As a result, the semi-geostrophic solution predicts a larger phase acceleration. The smaller phase acceleration observed in the numerical simulations may result from nonlinear blocking effects caused by the larger mountain.

103
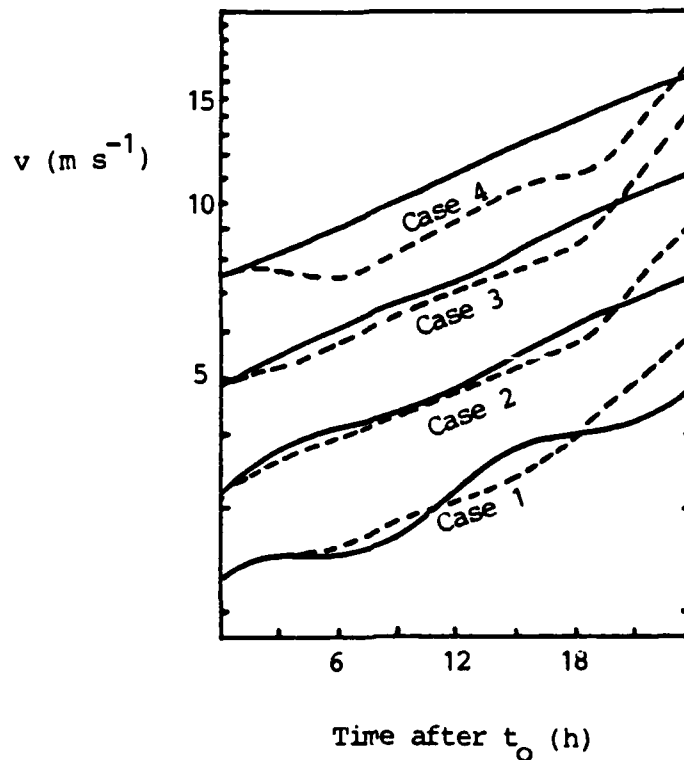
Figure 6.11.  Amplitude of wave number 8 of v at $\sigma = 0.9167$ at 45°N for Experiment II, Cases 1, 2, 3, and 4.  Interaction (dashed) and Non-interaction (solid) solutions are shown.

## 4.  Experiment III: 8° Jet, 47°x24°x1.5 km Mountain

In this experiment, the effect of the horizontal structure of the mean flow on the interaction between the disturbance and the mountain is considered.  The halfwidth of the jet, $\gamma$ (in 4.1 and 4.2), is reduced to 8° and the four cases of Experiments I and II are run with a 1.5 km mountain.  As noted earlier, this mean wind profile meets the necessary condition for barotropic instability both to the north and south of the jet stream axis.  This led to a smaller growth rate in the Control B run, and consequently, it is anticipated that the growth observed in this experiment will be less than that observed in Experiments I and II.

104

The Interaction and Non-interaction solutions for Cases 1 and 4 at $t = t_0 + 24$ h are shown in Figures 6.12 and 6.13, respectively. As anticipated, the growth is somewhat less than was observed earlier. The maximum amplitudes of these disturbances (given as the minimum $p_s'$ in Table 6.4) are from 3 to 15 mb weaker than those of Experiments I and II. In addition, a closed cyclone does not occur in every case. It is observed only in the cases in which the initial disturbance amplitude is large. This is in contrast to the results of Experiments I and II in which the initial disturbance amplitude did not appear to be critical to the formation of a closed surface isobar. It is also in better agreement with the result of Trevisan (1976).

As in the previous two experiments, the final amplitudes of the Interaction and Non-interaction disturbances are within a few millibars of each other in every case. However, here, the Non-interaction disturbances are slightly more intense. In fact, closed circulations result in all but the first Non-interaction run and only in the Case 4 Interaction run. The amplitude of v along 45°N at $\sigma = 0.9167$ is plotted versul time for each of the four cases in Figure 6.14. During the first 15 hours, the growth rates of the Interaction and Non-interaction disturbances are in rough agreement. After $t = t_0 + 15$ h, growth in the Interaction runs occurs at a slower rate.

An interesting contrast to earlier results is in the location at which a closed circulation is first observed. In Experiments I and II, the closed low was not observed until the disturbance reached the bottom of the mountain. Here, in Cases 2 through 4, the closed circulation is first observed along the lee slope close to the mountain top.
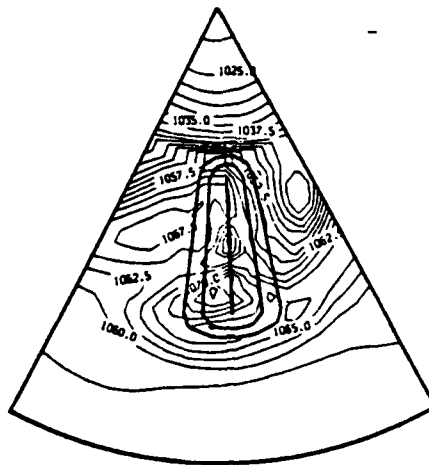
105

Figure 6.12a.   Sea-level pressure contours at $t_0$+24 h for Interaction
                solutions of Experiment III, Case 1.  Contour interval is
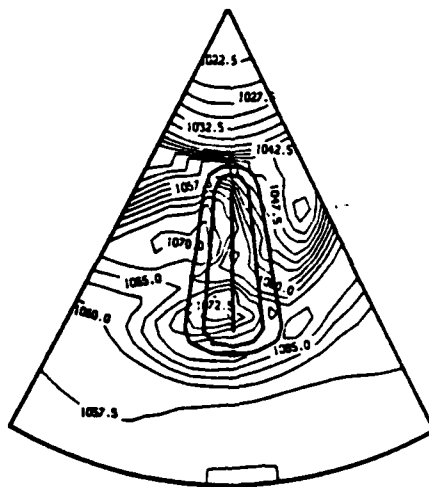                2.5 mb.  Bold contours at center of figure represent
                mountain.



Figure 6.12b.   Sea-level pressure contours at $t_0$+24 h for Non-interaction
                solutions of Experiment III, Case 1.  Contour interval is
                2.5 mb.  Bold contours at center of figure represent
                mountain.

Figure 6.13a.   Sea-level pressure contours at $t_0$+24 h for Interation
solutions of Experiment III, Case 4.   Contour interval is
2.5 mb.   Bold contours at center of figure represent
mountain.



Figure 6.13b.   Sea-level pressure contours at $t_0$+24 h for Non-interaction
solutions of Experiment III, Case 4.   Contour interval is
2.5 mb.   Bold contours at center of figure represent
mountain.

107

Table 6.4.  Experiment III.  Cases 1-4.
Disturbance Characteristics

| Case | Min $p'_s$ (mb) | | Phase Speed ($m\ s^{-1}$) | | $V_M$ ($m\ s^{-1}$) | Phase Differences (km) | |
|------|------|------|------|------|------|------|------|
| | I* | N | I | N | | SG | Exp |
| 1 | -2.9 | -2.7 | 15.5 | 12.5 | -9.8 | 191 | 256 |
| 2 | -4.1 | -4.1 | 14.6 | 11.8 | -10.2 | 198 | 243 |
| 3 | -5.4 | -6.0 | 13.6 | 11.0 | -17.1 | 332 | 228 |
| 4 | -7.6 | -8.4 | 15.0 | 12.1 | -19.0 | 369 | 246 |

* I - Interaction; N = Non-interaction
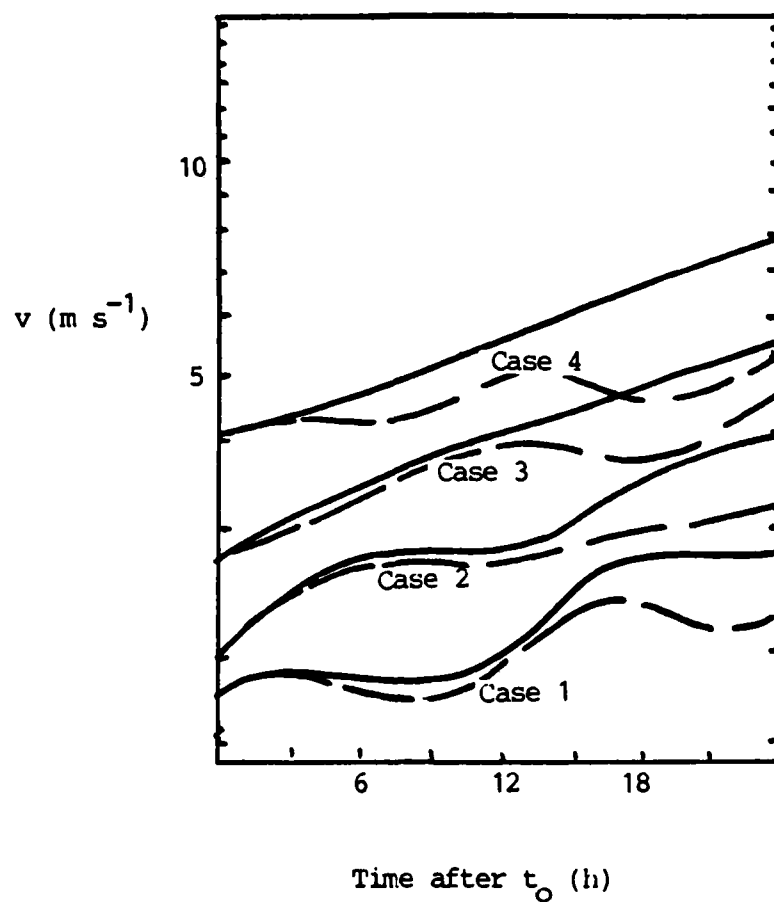
Figure 6.14. Amplitude of wave number 8 of v at $\sigma = 0.9167$ at 45°N for Experiment III, Cases 1, 2, 3, and 4. Interaction (dashed) and Non-interaction (solid) solutions are shown.

109

Results of the phase calculations are shown in Table 6.4. As can be seen, the presence of the mountain causes a 20-25% increase in phase speed and in the Interaction runs (over the Non-interaction runs). However, the average values observed here are 3-5 m s$^{-1}$ less than were observed in the previous experiments. The phase lag observed here agrees well with the value predicted by the semi-geostrophic solution.

5.  <u>Experiment IV: 8$^o$ Jet, 47$^o$x24$^o$x3.0 km Mountain</u>

In this experiment, the mountain height is raised to 3.0 km to examine the combined effect of the narrower jet and the higher mountain on disturbance growth. The first three cases of Experiment III are re-run for a 3.0 km mountain. In Case 4 (not shown), a large inertial oscillation was observed in the v fields of the Interaction run and this prevented a meaningful comparison with the corresponding Non-interaction run.

Based on the similarity of the results of Experiments I and II, it is anticipated that the 3.0 km mountain will have essentially the same net effect on disturbance growth as the 1.5 km mountain. That is the final amplitudes of the Interaction disturbances should be slightly weaker than those of the Non-interaction disturbance and considerably weaker than those of Experiment II. Examination of the minimum values of $p_s'$ for each of the three cases in Table 6.5 reveals that both of these expectations hold true. The Non-interaction disturbances have slightly lower $p_s'$ than the Interaction disturbances and both sets of values are approximately the same as those for the corresponding runs of Experiment III (Table 6.4). In addition, the final amplitudes are from 2 to 20 mb weaker than those of Experiment II (Table 6.3).

110

Table 6.5. Experiment IV. Cases 1-4.

Disturbance Characteristics

| Case | Min $p_s^!$ (mb) | | Phase Speed (m s$^{-1}$) | | $V_M$ (m s$^{-1}$) | Phase Differences (km) | |
|---|---|---|---|---|---|---|---|
| | I* | N | I | N | | SG | Exp |
| 1 | -2.6 | -2.7 | 20.5 | 12.5 | -12.0 | 233 | 668 |
| 2 | -3.4 | -4.1 | 20.1 | 11.8 | -13.0 | 252 | 725 |
| 3 | -4.2 | -6.0 | 19.8 | 11.0 | -25.5 | 495 | 762 |

* I - Interaction; N = Non-interaction .

The Interaction and Non-interaction solutions for Cases 1 and 4 at $t = t_0 + 24$ h are shown in Figures 6.15 and 6.16, respectively. As in Experiment III, a closed low is observed only in the Non-interaction runs of Cases 2 and 3, not in the corresponding Interaction runs. Also, as in Experiment III, the cyclogenesis occurs over the lee slope.

The secondary cyclone noted in Experiment II is also observed here over the mountain top, although only in the Interaction runs.

Figure 6.15a. Sea-level pressure contours at $t_0$+24 h for Interaction solutions of Experiment IV, Case 1. Contour interval is 2.5 mb. Bold contours at center of figure represent mountain.

Figure 6.15b. Sea-level pressure contours at $t_0$+24 h for Non-interaction solutions of Experiment IV, Case 1. Contour interval is 2.5 mb. Bold contours at center of figure represent mountain.
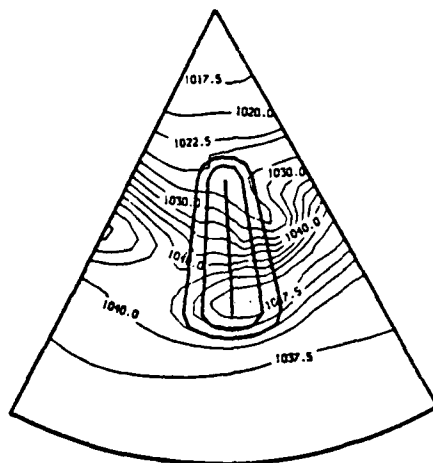
Figure 6.16a.  Sea-level pressure contours at $t_0$+24 h for Interaction
solutions of Experiment IV, Case 3.  Contour interval is
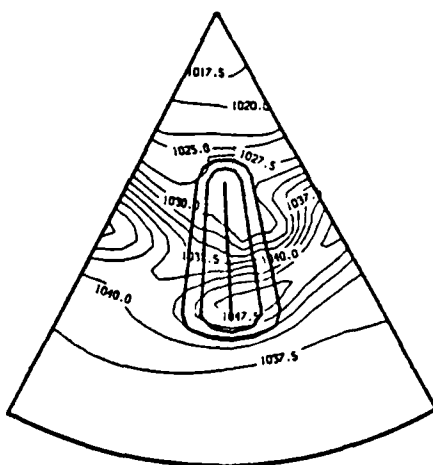2.5 mb.  Bold contours at center of figure represent
mountain.



Figure 6.16b.  Sea-level pressure contours at $t_0$+24 h for Non-interaction
solutions of Experiment IV, Case 3.  Contour interval is
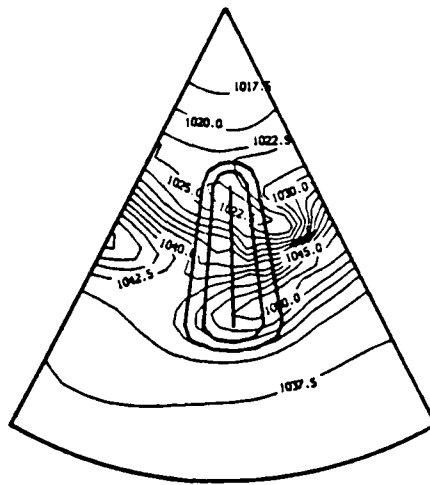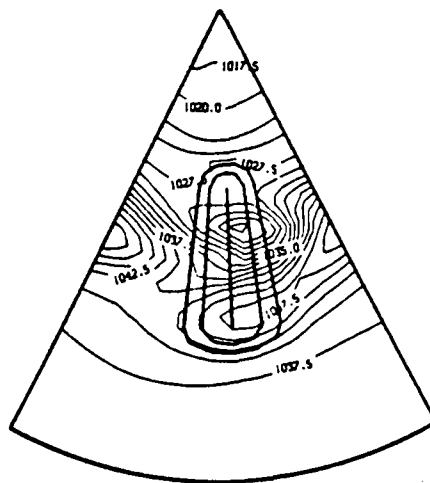2.5 mb.  Bold contours at center of figure represent
mountain.

The amplitude of the feature is less than that observed in Experiment II, as might have been anticipated based on the comparison of the primary disturbances. The lack of a secondary cyclone in the Non-interaction runs may be related to the proximity of the primary disturbance to the mountain top. In each of the Non-interaction solutions, the disturbance is located over the lee slopes at $t = t_0 + 24$ h. In the Interaction runs, it has moved over the plain well east of the mountain top.

Results of the phase calculations are shown in Table 6.5. Phase speeds of the Interaction disturbances are 8-9 m s$^{-1}$ higher than those of the Non-interaction disturbances, and 5-6 m s$^{-1}$ higher than those of the Interaction runs of Experiment III. This latter result differs from that of Experiment II in which the increase in mountain height resulted in only a 1-2 m s$^{-1}$ increase in phase speed. This dramatic increase in phase speed is also evident in the large differences between the semi-geostrophic and experimental phase lags. It suggests that nonlinear effects cause additional acceleration over that predicted by the semi-geostrophic solution.

6.  Experiment V: Short Versus Long Mountain

In this experiment, the effect of mountain length on disturbance growth is considered. The evolution of the disturbance from Case 3 of Experiments I and II is considered in the presence of shorter (25$^o$ latitude, north-south) and longer (57$^o$, north-south) mountains. Based on the results of Walker (1982), it is anticipated that less development will be observed with the shorter mountain than with the longer one.

114

The Interaction and Non-interaction solutions at $t = t_0 + 24$ h for run Va, with the short mountain are given in Figure 6.17. Lee cyclogenesis is not observed in either run. The 24-hour track of the Interaction disturbance is shown in Figure 6.18. As can be seen, the disturbance moves to the north of the mountain and takes a more northerly course than in the previous experiments where disturbances moved over the mountain. Lee cyclogenesis is not observed in either run. These results agree with those of Walker (1982) who found that disturbances tended to move around smaller scale mountains and exhibited little tendency toward cyclogenesis.
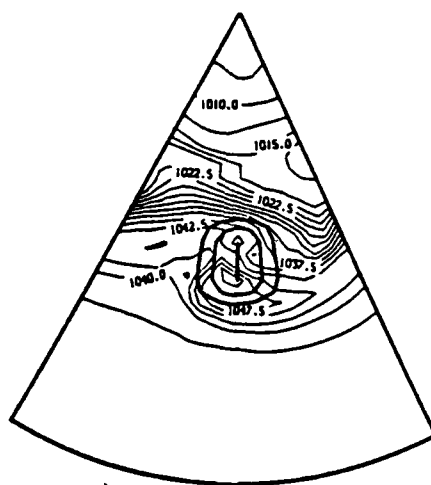


Figure 6.17a.   Sea-level pressure contours at $t_0$+24 h for Interaction solutions of Experiment Va, Case 3. Contour interval is 2.5 mb. Bold contours at center of figure represent mountain.
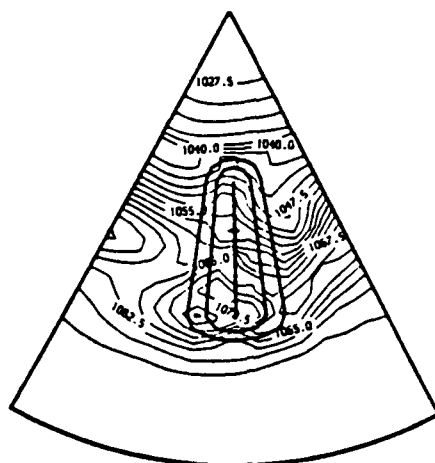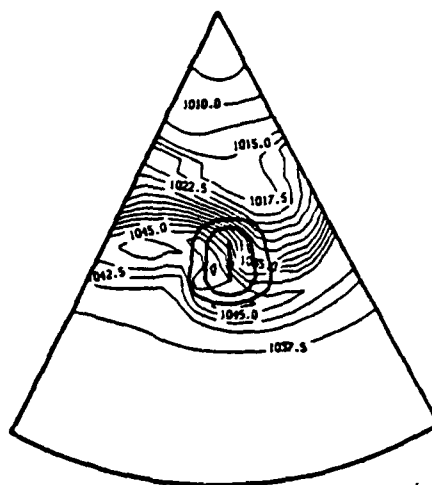
Figure 6.17b.   Sea-level pressure contours at $t_o$+24 h for Non-interaction solutions of Experiment Va, Case 3.   Contour interval is 2.5 mb.   Bold contours at center of figure represent mountain.
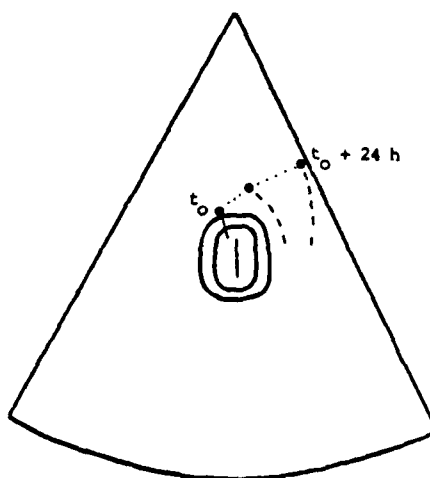


Figure 6.18.   Position of surface-pressure trough at $t_o$, $t_o$+12 h, and $t_o$+24 h in Experiment Va.

116

The minimum values of $p_s'$ for this experiment are given in Table 6.6. As before, little difference in amplitude exists between the Interaction and Non-interaction solutions. The secondary cyclone that was noted in Experiments II and IV is also observed in Figure 6.17. In the Interaction run, it appears as a weak low along the northern slope near the mountain top. In the Non-interaction run, it appears further south and west along the windward slope of the mountain. The phase acceleration experienced by the primary disturbance is considerable. The interaction disturbance is approximately 564 km further east than the Non-interaction disturbance. Its phase speed is nearly 6 m s$^{-1}$ greater than that of the Non-interaction run, and some 3 m s$^{-1}$ greater than the corresponding values observed in Experiments II and IV. This rapid movement may be at least partially due to accelerations experienced by the Interaction disturbance along the northern slope of the mountain.

Table 6.6.  Experiment V.  Cases 1-4.
Disturbance Characteristics

| Case | Min $p_s'$ (mb) | | Phase Speed (m s$^{-1}$) | | $V_M$ (m s$^{-1}$) | Phase Differences (km) | |
|------|-------|-------|------|------|------|------|------|
| | I* | N | I | N | | SG | Exp |
| Va | -10.1 | -11.3 | 21.7 | 15.1 | -13.0 | 252 | 564 |
| Vb | -13.3 | -11.3 | 17.6 | 15.1 | -29.6 | 575 | 214 |

* I - Interaction; N = Non-interaction

The Interaction and Non-interaction solutions at $t = t_0 + 24$ h are given in Figure 6.19. Lee cyclogenesis is observed in both cases, and the closed circulation is first observed while the disturbance is still over the lee slope of the mountain. This differs from the results of Experiments I and II in which a closed circulation was not observed until the disturbance reached the plain east of the mountain. The earlier appearance of a closed surface circulation in both the Interaction and Non-interaction runs indicates that it results from the superposition of the disturbance on a more intense lee-side trough. This result, which is not predicted by the two-dimensional models considered in Chapter II, suggests that the north-south dimension of the mountain may play a role in the location and intensity of the cyclogenesis.

Minimum $p'_S$ values for this run are given in Table 6.6. As in all previous experiments, little difference exists between the Interaction and Non-interaction solutions indicating that *the mountain* has little net effect on the disturbance. Comparison of these values with those of Experiments II and Va yields a similar conclusion. The phase-speed calculations given in Table 6.6 show that the phase speed of the Interaction disturbance in this run is approximately the same as that in Experiment II. The experimental phase acceleration is also much less than is predicted by the semi-geostrophic solution.

The secondary circulation noted in the previous 3.0 km mountain cases is observed here as well in the Interaction run where an intense small-scale cyclonic circulation exists over the mountain top. No such circulation is observed in the Non-interaction run, though a pressure trough is observed in approximately the same location. The position of

118
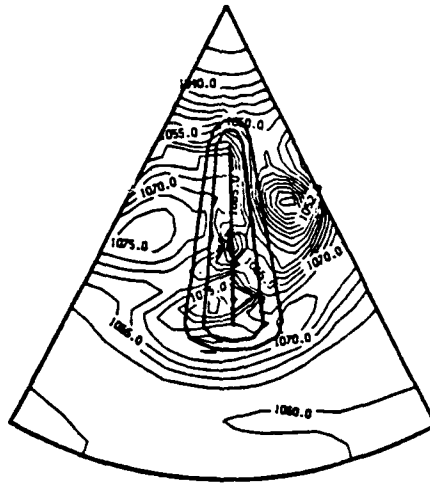
Figure 6.19a.   Sea-level pressure contours at $t_0$+24 h for Interaction
                solutions of Experiment Vb, Case 3.   Contour interval is
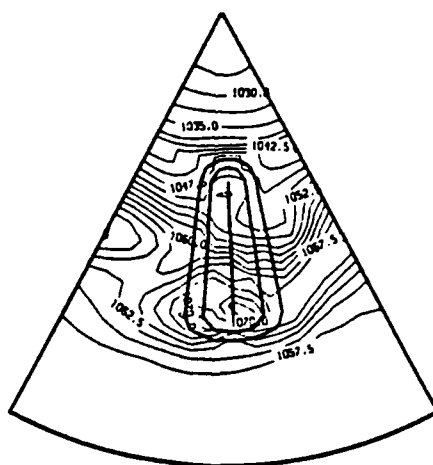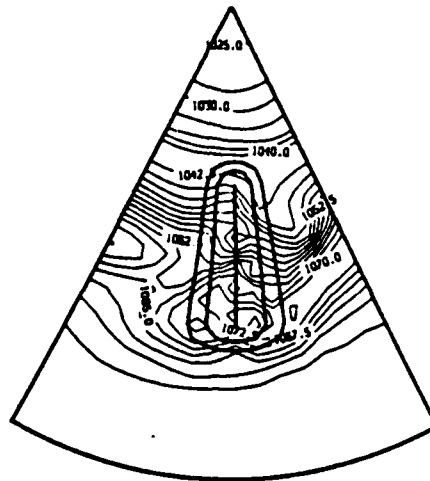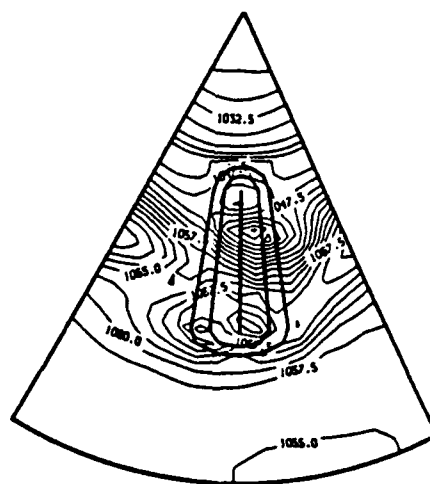                2.5 mb.   Bold contours at center of figure represent
                *mountain.*
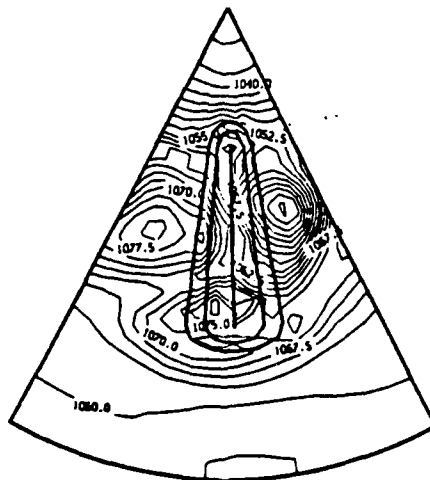


Figure 6.19b.   Sea-level pressure contours at $t_0$+24 h for Non-interaction
                solutions of Experiment Vb, Case 3.   Contour interval is
                2.5 mb.   Bold contours at center of figure represent
                *mountain.*

the secondary low-pressure center is shown at three-hourly intervals in Figure 6.20. The secondary cyclone is first observed at $t = t_0 + 15$ h as a weak low pressure system along the windward slope of the mountain. Over the next 12 hours, the low moves northeastward up the mountain, intensifying and broadening slightly in horizontal scale. The low reaches its maximum amplitude as it reaches the top of the mountain at $t = t_0 + 24$ h. Thereafter, the low drifts southward along the mountain top and weakens. By $t = t_0 + 30$ h, only 6 hours after it has reached its maximum amplitude, the secondary cyclone has disappeared. This feature and its behavior resemble the "type B" cyclone described by Schallert (1962) in his study of Colorado cyclones. It also resembles the forced Kelvin wave described by Gill (1977) and Murakami and Nakamura (1983).
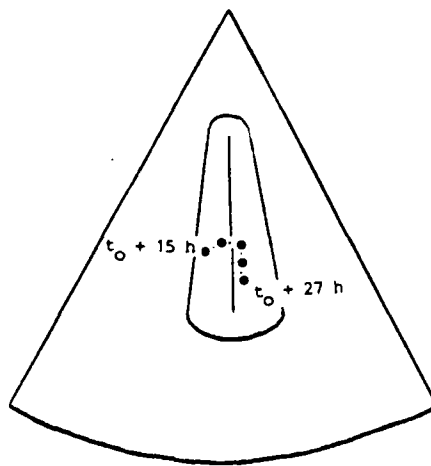


Figure 6.20.  Position of secondary surface-pressure low at three-hourly intervals for Experiment Vb.

120

In this chapter, Merkine's (1975) suggestion that lee cyclogenesis results from enhanced instability on the lee side of large mountain ranges was considered using a rough approximation of the Rocky Mountains as a model. Results of the numerical experiments indicate that disturbances moving over mountains appear to develop more rapidly and to greater intensities than disturbances moving over flat terrain. However, these increases are shown to be due predominantly to the effect of the superposition of the baroclinic disturbance on the orographically forced lee-side trough. When the basic states are subtracted, little difference is observed between the amplitudes of disturbances developing on the lee-side of the mountain and those developing over flat terrain. Slight increases in growth are observed in the Interaction runs. However, the effect of these increases is overwhelmed by the effect of the superposition. This basic result is not significantly different for the experiments in which mountain height and length, initial disturbances amplitude, and the horizontal structure of the basic state are varied. In general, increases in the intensity of the lee-side cyclonic disturbances considered in this study are due to increases in either the initial amplitude of the disturance or the amplitude of the orographically forced lee-side trough, and not to enhance baroclinic instability.

Two additional results are also noted. First, a phase acceleration is observed as the disturbance moves over the mountain. This acceleration is predicted by the semi-geostrophic, Eady model considered in Chapter II. Qualitative agreement exists between the semi-geostrophic and experimental values for the 1.5 km mountain experiments, although the semi-geostrophic estimates tend to be larger than the experimental values

in the 3.0 km mountain experiments. This latter result is attributed to a nonlinear blocking effect caused by the larger mountain.

Second, a secondary cyclonic circulation similar to the small-scale Colorado cyclone observed by Schallert (1962) and the Kelvin wave described by Gill (1977) and Murakami and Nakamura (1983) is observed in the 3.0 km mountain experiments. This feature develops rapidly as it moves up the western slope of the mountain, but dissipates just as rapidly as it moves southward along the mountain ridge after reaching the top. At not time does this secondary cyclonic circulation appear to affect the development of the primary (or lee) cyclone.

## VII. CONCLUSIONS

The objective of this research is to explain the high incidence of cyclogenesis in the lee of the major mid-latitude mountain ranges. The study is restricted to long, north-south barriers similar to the Rocky Mountains. Three possible mechanisms were considered: 1) enhanced, lee-side baroclinic instability; 2) continuous-mode growth; and 3) superposition.

Simple analaytical models were used to provide a theoretical basis for the investigation. Eady's model was adapted to include the linear effects of the mountain through the lower boundary condition. The evolution of a baroclinic wave crossing the mountain was simulated by superposing the classical, time-dependent Eady solution upon the steady orographically forced solution for Eady's model. The developing wave was partially cancelled as it moved up the mountain by the orographically forced high pressure ridge. As it reached the lee-side, however, the disturbance appeared to grow rapidly as it became superposed with the forced lee-side trough. This rapid development occurred in a manner not unlike that observed in lee cyclogenesis - without any actual interaction between the disturbance and the mountain.

A semi-geostrophic model was considered to include finite-amplitude effects. It was shown that the model reduces to Eady's model if the Hoskins transformation is used. As with the linear model, the solution of this model indicated that the mountain affects the amplitude of the baroclinic wave only through the steady, forced solution; in other words,

there is no net orographic effect. However, a phase acceleration is predicted as the disturbance crosses the mountain. For the mean flow considered in this study, the phase acceleration, which is governed by the Hoskins transformation, resulted in an additional phase displacement of approximately 300-400 km over a 24-hour period.

Farrell (1982) proposed that continuous spectrum growth could be important for lee cyclogenesis. He showed that rapid initial growth is possible with the appropriate initial conditions, but that the long term behavior gives dampening proportional to $1/t^2$ (Pedlosky, 1964). In this thesis, the initial disturbance was chosen to cancel the forced mountain solution. The numerical experiments with the linearized spectral model showed that this initial disturbance was oscillatory in time, and there was no indication of any tendency for amplification. In experiments with the fully nonlinear, potential enstrophy conserving UCLA model, disturbances forced by the mountain did not grow until some 30-40 hours after initial excitation, at which time discrete-mode growth began to dominate.

Merkine (1975) proposed that lee cyclogenesis is more frequent because the lee sides of major mountain ranges are regions of enhanced baroclinic instability. In this study, the fully nonlinear UCLA model was used with a vertically and horizontally sheared westerly flow across a long north-south barrier to determine the relative importance of the enhanced baroclinic instability mechanism and the superposition mechanism. Initial disturbance amplitude, mountain height and length, and the horizontal structure of the mean flow were varied. In each experiment, three simulations were generated: a Control run (without topography), an

Interaction run, and a Non-interaction run. In the Interaction runs, the perturbation fields from the Control run were superposed on a numerically derived mountain mean state, and these conditions were integrated forward in time without any imposed dynamical constraints. In the Non-interaction runs, a time evolution of the same disturbance was constructed without model integration by superposing upon the Mountain mean state perturbation fields taken from the Control run at various stages of development. These three runs were intercompared to estimate the growth due to normal baroclinic processes and that due to the superposition of the disturbance on the orographically forced solution. In this way, any additional growth resulting from destabilization of the mean flow could be isolated.

The results indicate that the distortions of the mean flow caused by the mountains do not result in significantly enhanced baroclinic instability for the cases studied. Disturbances in the distorted mean flow developed at approximately the same rate as those in a parallel mean flow. In addition, the amplitude of the disturbance as it begins to move away from the mountain was approximately the same in both the Interaction and Non-interaction runs. This basic result is not significantly affected by varying the initial disturbance amplitude, the mountain height or length, and the horizontal structure of the mean flow. Consequently, superposition dominates over enhanced baroclinic instability in this study.

Other features of the numerical solutions are also of interest. The mountain-induced divergent flow caused an acceleration of the disturbance as it moved over the mountain. This effect was predicted by the solution

125

of the semi-geostrophic, Eady model and was observed in the Interaction simulations of Chapter VI. The accelerations caused by the lower mountains agreed well with those predicted analytically; however, those caused by the higher mountain were overestimated by the semi-geostrophic model. This latter result is an indication that nonlinear effects are important, and may be a consequence of a tendency for air to flow around rather than over the larger barrier.

A secondary cyclonic circulation which is not predicted by the analytical models was also observed in the simulations of Chapter VI. This feature which is similar to the forced Kelvin wave described by Gill (1977) and Murakami and Nakamura (1982) appeared in all simulations with the higher mountains and in none of those with the lower mountains. The secondary cyclone developed rapidly as it moved up the western slope of the mountain and weakened, just as rapidly, as it drifted southward after reaching the mountain top. At *no time did this* feature appear to affect the development of the primary cyclonic disturbance nor did it show any tendency to develop into a lee cyclone. However, the rapid development of this forced disturbance suggests that enhanced instability may exist over the mountain for scales shorter than the synoptic scale. Its dependence on mountain height suggests that the feature is an orographically forced circulation which depends critically on mountain size.

Mountain length had an effect on disturbance intensity and rate of growth. The longer mountain, because it represented a larger barrier to the westerly mean flow, resulted in a larger amplitude forced ridge-trough pattern. This, in turn, affected the observed amplitude and rate of growth of the lee-side disturbance. Cyclogenesis was not observed in

the experiments with the shortest mountain indicating that the mountain length may play a role in whether or not a closed circulation is observed.

For the two mean flows considered, the horizontal structure of the mean flow appeared to affect the growth rate of the disturbance. The narrower jet resulted in a lower growth rate in the Control cases of Chapter VI. This effect was also observed in the experiments with mountains and appears to result from there being less available potential energy in the narrower jet and possibly from barotropic effects.

This research has shown that superposition is the dominant mechanism of lee cyclogenesis for long mountain ranges which are perpendicular to the basic current. When the time mean flow is subtracted, the resulting disturbances show little effect as they move over the mountain barrier. However, when the total flow is viewed, rapid cyclogenesis occurs as the disturbance moves down the lee-side slope under the influence of the mountain-forced horizontal convergence. The superposition mechanism can be expected to affect cyclogenesis whenever there are synoptic-scale forced fields. In particular, the heating off the east coasts off mid-latitude continents could produce a surface low which would increase the frequency of cyclogenesis in those regions.

In addition, this research has shown that the amplitude of the oro-graphically-forced, lee-side trough is a significant factor in the occurrence of apparent cyclogenesis in the lee of a long meridional barrier. It has further shown that the amplitude of the forced trough is affected by the height and length of the mountain as well as the strength

127

of the current perpendicular to the mountain. These results have application to operational forecasting of lee cyclogenesis because they suggest a more important role is played by the lee-side trough.

Hovanec and Horn (1975) have shown that static stability is decreased in the lee of the Rockies just prior to cyclogenesis. Static stability was allowed to vary in all but the linear models of this study and large increases in disturbance growth were not observed. However, the effect of feedback through diabatic mechanisms was ignored. This effect, which is not thought to be significant, could be evaluated by including the diabatic terms in the numerical simulations.

The procedure used in this study would be improved if true steady-state solutions could be found for the basic flow over the mountain range. Possible techniques include the method developed by Kalnay-Rivas (1977) and the semi-geostrophic approach used by Bannon (1984) and in this study.

The research in this study should be extended to other basic flows and other mountain barriers. For example, Smith (1984) proposed a mechanism for lee cyclogenesis in the Alps which depends on a mean flow in which the vertical wind shear is opposite to the surface wind component across the mountain range. In this case, there is a large steady state response and the "cyclogenesis" is not a true instability. This mechanism needs to be investigated with more realistic conditions.

# LIST OF REFERENCES

Arkawa, A., and V. Lamb, 1977: Computational design of the basic dynamical processes of the UCLA general circulation model. Methods in Computational Physics, 17, 173-265, Academic Press, New York.

Arakawa, A., and V. Lamb, 1981: A potential enstrophy and energy conserving scheme for the shallow water equations. Mon. Wea. Rev., 109, 18-36.

Arakawa, A., and M. Suarez, 1983: Vertical differencing of the primitive equations in sigma coordinates. Mon. Wea. Rev., 111, 34-45.

Bannon, P. R., 1984: A semi-geostrophic model of frontogenesis over topography. Bietrage zur Physik der Atmoshare, Vol 57, No. 3, 393-408.

Bleck, R., 1977: Numerical simulation of lee cyclogenesis in the Gulf of Geona. Mon. Wea. Rev., 105, 428-445.

Buzzi, A., and S. Tibaldi, 1978: Cyclogenesis in the lee of the Alps: a case study. Quart. J. Roy. Met. Soc., 104, 271-287.

Charney, J. G., and P. G. Drazin, 1961: Propagation of planetary scale disturbances from the lower into the upper atmosphere. J. Geophys. Res., 66, 83-109.

Charney, J. G., and J. DeVore, 1979: Multiple flow equilibria in the atmosphere and blocking. J. Atmos. Sci., 36, 1205-1216.

Charney, J. G., and D. Strauss, 1980: Form-drag instability, multiple equilibria and propagating planetary waves in baroclinic orographically forced, planetary wave systems. Atmos. Sci., 41, 1157-1176.

Chung, Y. -S., K, Hage, and E. Reinelt, 1976: On lee cyclogenesis and airflow in the Canadian Rocky Mountains and the East Asian Mountains. Mon. Wea. Rev., 104, 878-891.

Eady, E., 1949: Long waves and cyclone waves. Tellus, 3, 33-52.

Egger, J., 1974: Numerical experiments on lee cyclogenesis. Mon. Wea. Rev., 102, 847-860.

Farrell, B. F., 1982: The initial growth of disturbances in a baroclinic flow. J. Atmos. Sci., 39, 1663-1686.

Gill, A., 1977: Coastally trapped waves in the atmosphere. Quart. J. Roy. Met. Soc., 103, 431-440.

Grotjahn, R., 1979: Cycline development along weak thermal fronts. J. Atmos. Sci., 36, 249-274.

Haltiner, G., and R. T. Williams, 1980: Numerical Prediction and Dynamical Meteorology. John Wiley and Sons, Inc., New York. 477 pp.

Hess, S., and H. Wagner, 1948: Atmospheric waves in the northwestern United States. J. Meteor., 5, 1-19.

Holton, J. R., 1972: An Introduction to Dynamic Meteorology. Academic Press, New York. 319 pp.

Hoskins, B. J., 1975: The geostrophic momentum approximation and the semi-geostrophic equations. J. Atmos. Sci., 32, 233-242.

Hoskins, B. J., and F. P. Bretherton, 1972: Atmospheric frontogenesis models: mathematical formulation and solutions. J. Atmos. Sci., 29, 11-37.

Hovanec, R. D., and L. H. Horn, 1975: Static stability and the 300 mb isotach field in the Colorado cyclogenetic area. Mon. Wea Rev., 103, 18-36.

Huppert, H., and K. Bryan, 1975: Topographically generated eddies. Deep Sea Res., 23, 655-679.

Kalnay-Rivas, E., 1977: Numerical scheme to solve unstable boundary value problems. Advances in Computing for Partial Differential Equations, Vol II, 264-268.

Klein, W., 1958: The frequency of cyclones and anticyclones in relation to the mean circulation. J. Meteor., 15, 98-102.

Lubeck, O., T. Rosmond, and R. T. Williams, 1977: Divergent initialization experiments using a spectral model. Naval Postgraduate School Technical Report NPS-63Wu7791, 81 pp.

Manabe, S., and T. Terpstra, 1974: The effects of mountains on the general circulation of the atmosphere as identified by numerical experiments. J. Atmos. Sci., 31, 3-42.

Merkine, L. -O., 1975: Steady, finite-amplitude, baroclinic flow over long topography in a rotating, stratified atmosphere. J. Atmos. Sci., 32, 1881-1893.

Merkine, L. -O., 1977: Convective and absolute instability of baroclinic eddies. Geophys. Astrophys. Fluid Dynamics, 9, 127-157.

Merkine, L. -O., and M. Israeli, 1978: The stability of a Rossby wave in a baroclinic zonal flow. J. Atmos. Sci., 35, 1388-1394.

Murakami, T., and H. Nakamura, 1983: Orographic effects on cold surges and lee cyclogenesis as revealed by numerical experiment. Part II. Transient aspects. J. Meteorol. Soc. Japan, 61, 547-567.

Newton, C. W., 1956: Mechanisms of circulation change during a lee cyclogenesis. J. Meteor., 13, 528-5 ʼ.

Palmen, E., and C. W. Newton, 1969: Atmospheric Circulation Systems. Academic Press, New York. 603 pp.

Pedlosky, J., 1964: An initial value problem in the theory of baroclinic instability. Tellus, 16, 12-17.

Pedlosky, J., 1981: Resonant topographic waves in barotropic and baroclinic flows. J. Atmos. Sci., 38, 2626-2641.

Petterssen, S., 1956: Weather Analysis and Forecasting. Vol I., McGraw-Hill Book Company, New York. 428 pp.

Reitan, C., 1974: Frequencies of cyclones and cyclogenesis for North America, 1951-1970. Mon. Wea. Rev., 102, 861-868.

Rennick, M. A., and R. T. Williams, 1985: Representation of the tropopause in sigma coordinates. In preparation.

Schallert, W. L., 1962: An Investigation of Colorado cyclones. Sci. Report No. 7, Contract AF 19 (604)-7230, Dept of Meteorology, University of Chicago, 68 pp.

Smith, R. B., 1979: The influence of mountains on the atmosphere. Advances in Geophysics, 21, 87-230.

Smith, R. B., 1984: A theory of lee cyclogenesis. J. Atmos. Sci., 41, 1159-1168.

Tibaldi, S., A. Buzzi, and P. Malguzzi, 1980: Orographically induced cyclogenesis: analysis of numerical experiments. Mon. Wea. Rev., 108, 1302-1314.

Trevisan, A., 1976: Numerical experiments on the influence of topography on cycline formation with an isentropic primitive equation model. J. Atmos. Sci., 33, 768-780.

Walker, J. P., 1982: Numerical simulation of the influence of small scale mountain ranges on a baroclinic wave. Naval Postgraduate School Master's Thesis. 159 pp.

Whittaker, L. M., and L. H. Horn, 1981: Geographical and seasonal distribution of North American Cyclogenesis, 1958-1977. Mon. Wea. Rev., 109, 2312-2322.

Williams, R. T., J. Hayes, F. Winninghoff, and O. Haney, 1981: Numerical simulation of air flow over and around a long mountain range. Reprints: Fifth Conference on Numerical Weather Prediction (Monterey, California), Amer. Meteor. Soc., Boston, 137-138.

Zishka, K. M., and P. J. Smith, 1980: The climatology of cyclones and anticyclones over North America and surrounding ocean environs for January and July, 1950-1977. Mon. Wea. Rev., 108, 387-401.

INITIAL DISTRIBUTION LIST

No. Copies

1.  Defense Technical Information Center                            2
    Cameron Station
    Alexandria, Virginia   22314

2.  Library, Code 0142                                             2
    Naval Postgraduate School
    Monterey, California   93943

3.  Dr. R. T. Williams, Code 63Wu                                 5
    Department of Meteorology
    Naval Postgraduate School
    Monterey, California   93943

4.  Director                                                      1
    Naval Oceanography and Meteorology
    National Space Technology Laboratories
    Bay St. Louis, Mississippi   39520

5.  Officer in Charge                                             1
    Navy Environmental Prediction Research Facility
    Monterey, California   93940

6.  Commanding Officer                                            1
    Fleet Numerical Oceanographic Central
    Monterey, California   93940

7.  Naval Oceanographic Office                                    1
    Library, Code 3330
    Washington, D.C.   20373

8.  AFCRL Research Library                                        1
    ATTN:  Nancy Davis/Stop 29
    L. G. Hanscom Field
    Bedford, Massachusetts   01730

9.  Commander, Air Weather Service                                1
    Military Airlift Command
    United Stated Air Force
    Scott Air Force Base, Illinois   62226

10. Dr. A. Arakawa                                                1
    Department of Meteorology
    University of California
    Los Angeles, California   90024

11.  Mr. Jeffrey P. Walker                                              1
     NOAA
     Western Regional Center
     7600 Sand Point Way, N.E.
     Seattle, Washington  98115

12.  Major John L. Hayes                                                5
     3300 Wellhouse Ct
     Herndon, Virginia  22071

13.  Atmospheric Sciences Library                                       1
     National Oceanic and Atmospheric Administration
     Silver Spring, Maryland  20910

14.  Dr. John Brown                                                     1
     National Meteorological Center/NOAA
     World Weather Building
     Washington, D.C.  20233

15.  Dr. C.-P Chang, Code 63CP                                          1
     Department of Meteorology
     Naval Postgraduate School
     Monterey, California  93943

16.  Dr. R. L. Elsberry, Code 63Es                                      1
     Department of Meteorology
     Naval Postgraduate School
     Monterey, California  93943

17.  Dr. R. L. Haney, Code 63Hy                                         1
     Department of Meteorology
     Naval Postgraduate School
     Monterey, California  93943

18.  CDR D. Hinsman                                                     1
     NEPRF
     Monterey, California  93943

19.  Dr. J. Holton                                                      1
     Department of Atmospheric Sciences
     University of Washington
     Seattle, Washington  98105

20.  Dr. B. J. Hoskins                                                  1
     Department of Geophysics
     University of Reading
     Reading, United Kingdom

21.  Dr. J. Young                                                       1
     Department of Meteorology
     University of Wisconsin
     Madison, Wisconsin  53706

22. Dr. A. Kasahara                                                 1
    National Center for Atmospheric Research
    P.O. Box 3000
    Boulder, Colorado   80303

23. Dr. M. G. Wurtele                                               1
    Department of Meteorology
    University of California
    Los Angeles, California   90024

24. Dr. E. N. Lorenz                                                1
    Department of Meteorology
    Massachusetts Institute of Technology
    Cambridge, Massachusetts   02139

25. Meteorology Library, Code 63                                    1
    Naval Postgraduate School
    Monterey, California   93943

26. National Center for Atmospheric Research                        1
    Box 1470
    Boulder, Colorado   80302

27. Director, Naval Research Laboratory                             1
    ATTN:  Technical Services Information Center
    Washington, D.C.   20390

28. Dr. E. C. Nickerson                                             1
    NOAA, Atmospheric Physics & Chemistry Laboratory
    Boulder, Colorado   80302

29. Prof. C. N. K. Mooers                                           1
    Department of Oceanography, Code 68
    Naval Postgraduate School
    Monterey, California   93943

30. Office of Naval Research                                        1
    Department of the Navy
    Washington, D.C.   20360

31. Prof. N. A. Phillips                                            1
    National Meteorological Center/NOAA
    World Weather Building
    Washington, D.C.   20233

32. Dr. J. Smagorinsky, Director                                    1
    Geophysical Fluid Dynamics Laboratory
    Princeton University
    Princeton, New Jersey   08540

135

33. Dr. T. Rosmond                                                  1
    Naval Environmental Prediction Research Facility
    Monterey, California  93943

34. Dr. D. Williamson                                               1
    National Center for Atmospheric Research
    P.O. Box 3000
    Boulder, Colorado  80303

35. Dr. Y. Sasaki                                                   1
    Department of Meteorology
    University of Oklahoma
    Norman, Oklahoma  73069

36. Prof. A. L. Schoenstadt                                         1
    Code 53 Zh
    Naval Postgraduate School
    Monterey, California  93943

37. Prof. Fedor Mesinger                                            1
    Department of Meteorology
    University of Belgrade
    11001 Beograd, p.p. 550
    Yugoslavia

38. Dr. M. J. P. Cullen                                             2
    Meteorological Office
    Bracknell, Berks,
    United Kingdom

39. Dr. R. L. Lee                                                   1
    Atmospheric and Geophysical Science Division
    University of California
    P.O. Box 808
    Livermore, California  94550

40. Dr. C. H. Wash                                                  1
    Code 63
    Naval Postgraduate School
    Monterey, California  93943

41. Prof. R. J. Renard, Code 63                                     1
    Naval Postgraduate School
    Monterey, California  93943

42. Dr. Andrew Staniforth                                           1
    Recherce en Prevsion Numerique
    West Isle Office Tower, 5 ieme etage
    2121 route Trans-Canada
    Dorval, Quebec H9P1J3, Canada

43. Dr. J. Hoverrmale                                                    1
    Naval Environmental Prediction Research Facility
    Monterey, California  93943

44. Dr. R. T. Pierrehumert                                               1
    Geophysical Fluid Dynamics Lab/NOAA
    P.O. Box 308
    Princeton, New Jersey  08540

45. W. Blumen                                                            1
    Campus Box 391
    University of Colorado
    Boulder, Colorado  80309

46. Dr. M. A. Rennick                                                    1
    Department of Meteorology
    Naval Postgraduate School
    Monterey, California  93943

47. Lt. Col. J. Cipriano                                                 1
    AFIT/CIRF
    Wright Patterson AFB, Ohio  45433

48. AWS Technical Library                                                1
    Scott AFB, Illinois  62225

49. Mr. P. Gallacher                                                     1
    Code 63
    Naval Postgraduate School
    Monterey, California  93943

50. Dr. M. Peng                                                          1
    Code 63
    Naval Postgraduate School
    Monterey, California  93943

51. Dr. S.-S. Liou                                                       1
    Code 63
    Naval Postgraduate School
    Monterey, California  93943

52. Dr. David Adamec                                                     1
    Code 63
    Naval Postgraduate School
    Monterey, California  93943

53. Captain A. R. Shaffer                                                1
    Det 1, 2nd Weather Sq.
    Wright Pattersen AFB, Ohio  45433

137

54. LCDR. Scott Sandgathe                                        1
    NOCC/JTWC
    COMNAVMARIANAS Box 17
    FPO San Francisco, California  96630

55. Carl Ihli                                                    1
    C. O. NOCF
    San Diego, California  92152

56. Dr. R. B. Smith                                              1
    Department of Geology and Geophysics
    Yale University
    P.O. Box 6666
    New Haven, Connecticut  06511

57. Dr. Peter Bannon                                             1
    Department of Geophysical Sciences
    University of Chicago
    Chicago, Illinois  60637

58. Prof. D. Johnson                                             1
    Department of Meteorology
    University of Wisconsin
    1225 W. Dayton Street
    Madison, Wisconsin  53706

59. Dr. Donna Blake                                              1
    Code 322
    NORDA
    NSTL Station, MS  39520

60. Dr. R. Gall                                                  1
    Code 63
    Naval Postgraduate School
    Monterey, California  93943

# END

# FILMED

7-85

# DTIC